Calculation and observation of x-ray-sensitive molecules in envelopes of young stellar objects

ETH
Eidgenössische Technische Hochschule Zürich
Swiss Federal Institute of Technology Zurich

Calculation and Observation of X-Ray-Sensitive Molecules in Envelopes of Young Stellar Objects

Simon Bruderer

Diploma Thesis at the Institute of Astronomy, ETH Zürich

March 2006

Supervisor: Prof. Dr. Arnold O. Benz

Assistant: Pascal Stäuber

Was von den Farben am Regenbogen und dergleichen hierbey außzudingen, das gehöret an sein Ort; Dann es werden auch die Sonnenstrahlen in den runden Regentröpfflin wahrhafftig gefärbet daß also in der Matery deß Wassers alle Farben, so man am Regenbogen siehet, darinnen stecken und durch das durchtringende Liecht der Sonnen herauß geführet werden.

Johannes Kepler (Tertius interveniens, These 28)

Title picture: The young stellar object AFGL 2591 ($\alpha_{2000} = 20^h29^m24.9^s$, $\delta_{2000} = 40°11'21.0''$) seen in infrared wavelengths by the NIRI (Near-IR Imager) instrument mounted on the 8-meter Gemini North telescope on Mauna Kea (Aspin et al.).

Abstract

Protostars start emitting high energetic FUV and X-ray photons after a not yet known point of evolution. Stars in this phase are still deeply embedded in their cloud and all radiation is absorbed. The radiation, however, can affect chemical abundances of molecules in the cloud. Several hydrides (e.g. CH, CH^+, OH, OH^+, NH) can act as tracers for X-rays.

To schedule observations with the HIFI instrument onboard the Herschel space telescope, we have estimated line intensities of the high-mass object AFGL 2591 and the low-mass objects IRAS 16293-2422 (Class I) and TMC 1 (Class 0) for the hydrides CH, CH^+, SH, SH^+, NH, OH^+ and the water ion H_2O^+. We have used the chemical model of Stäuber et al. (2005a) for our calculation. It was found that CH, CH^+ and NH are promising for a detection.

In a second part of the work, observations of star forming regions were carried out with the KOSMA telescope. We have observed the HCO^+(4–3) and HCO^+(3–2) lines in S140 and W3. Maps of both objects and a cut through S140 were measured. We have determined the column density and excitation temperature at the center position of S140. The cosmic ionization rate at this point has been estimated to be $\zeta \approx (0.9 - 4.9) \cdot 10^{-17}$ [s^{-1}].

Zusammenfassung

Protosterne emittieren hochenergetische FUV- und Röntgenstrahlung ab einem unbekannt Zeitpunkt. Sterne in dieser Entwicklungsphase sind tief eingebettet in ihre Hüllen, welche die gesamte Strahlung absorbieren. Die Strahlung kann jedoch die Häufigkeit von Molekülen in der Hülle verändern. Mehrere einfache Hydride (z.B. CH, CH^+, OH, OH^+, NH) können als Tracer für Röntenstrahlung fungieren.

Um Beobachtungen mit dem HIFI-Instrument des Herschel-Satelliten zu planen, wurden die Linienintensitäten der Hydride CH, CH^+, SH, SH^+, NH, OH^+ und des Wasser-Ions H_2O^+ für das high-mass Objekt AFGL 2591 und die low-mass Objekte IRAS 16293-244 (Class I) und TMC I (Class 0) abgeschätzt. Das chemische Modell von Stäuber et al. (2005a) wurde für die Berechnung verwendet. Wir finden, dass CH, CH^+ und NH aussichtsreiche Linienstärken für eine Detektion aufweisen.

In einem zweiten Teil der Arbeit wurden Beobachtungen von Sternentstehungsgebieten mit dem KOSMA-Teleskop durchgeführt. Wir haben die HCO^+(4–3) und HCO^+(3–2) Linien in S140 und W3 beobachtet. Karten beider Objekte und ein Schnitt durch S140 wurden erstellt. Wir haben die Kolonnendichte und Anregungstemperatur im Zentrum von S140 bestimmt. Für die Ionisationsrate von H_2 durch Kosmische Strahlung wurde an diesem Punkt ein Wert von $\zeta \approx (0.9 - 4.9) \cdot 10^{-17}$ [s^{-1}] abgeschätzt.

Contents

List of Figures

List of Tables

1 Introduction

The musician and amateur astronomer Friedrich Wilhelm Herschel (1738-1822) is famous for his discovery of Uranus in 1781 and his ever-growing telescopes. His appointment as "The King's Astronomer" gave him the possibility to turn to astronomy full-time. In honor of his employer King Georg III., he named the new planet "Georgium Sidus". Together with his sister Caroline who assisted his observations and saved herself a place in the history of astronomy for discovering several comets, he discovered two satellites of Uranus and Saturn and was first to realize that our solar system is moving through space. He also created the word "asteroid" and claimed that every planet was inhabited, even the sun due to a cool, solid surface protected from the hot atmosphere by opaque clouds... In 1800, he set up an experiment using a prism and three thermometers (Fig. 1): When he moved the the thermometer from the blue to the red light, he noticed a higher temperature. The big surprise was that the thermometer did no stop rising, when he placed it away from the red light to the "dark" area. He deduced the existence of a new kind of radiation out of this observation and called them "calorific rays" (Hamel 1998, Nussbaumer 2005).

In the year 2000, two hunderd years after this discovery, the ESA renamed the Far Infrared and Submillimetre Telescope FIRST after Herschel. The scheduled launch is in August 2007. With its 3.5 meter main mirror, it will be the largest space telescope to observe in far infrared and submillimeter wavelengths. Due to atmospheric attenuation, ground based telescopes are severely limited in wavelengths below 600 μm and in frequencies of water transitions due to the absorption by atmospheric water. The Herschel Space Observatory will therefore enlarge our knowledge about water - one of the basic requirements for life - and many other active topics as the formation of stars and galaxies or the chemistry of the interstellar medium. The Institute of Astronomy at the Swiss Federal Institute of Technology ETH in Zurich has contributed parts of the very high resolution spectrometer HIFI for Herschel. In return, the Institut of Astronomy has observation time at disposal. To schedule the valuable time, estimations of the expected intensities for the chosen observation targets are needed. The ETH measurements will concentrate on envelopes around Young Stellar Objects. One of the scientific objectives will be to draw conclusions about the X-ray radiation from young protostars out of the measured abundances of molecules.

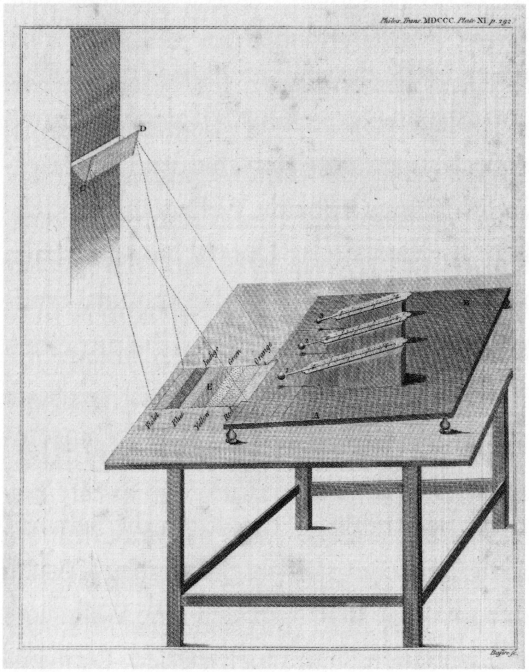

Figure 1: Herschels experiment (from Nussbaumer 2005)

In our work, we will first give a brief introduction to the physical mechanism of star formation, the chemical reactions inside a star forming area and their depence on UV radiation and X-rays. In Sect. 3, a brief introduction to radiative transfer problems and their solving by different techniques is given. The next section is designated to an overview of the molecular spectroscopy of diatomic molecules. Sect. 5 contains our calculation of the integrated intensity of CH, CH^+, NH, OH^+, SH^+ and H_2O^+ for the high-mass Young Stellar Object AFGL 2591 and the two low-mass objects IRAS 16293-2422 and TMC 1: After a brief description of the Herschel satellite and its abilities, the used physical and chemical model is described. Then we present the providing of the necessary molecular parameters from databases and spectroscopic constants: We describe the properties of the considered molecules and the compiling of the required parameters for radiative transfer calculations. Thereafter, the actual calculation of the line intensities is carried out. The most promising molecular transitions for an observation with Herschel are selected and the required observation time for those lines is estimated. We give the integrated line intensities for all calculated transitions and discuss their dependance on the X-ray flux of the central young star.

In a second part of the work, we have observed the star formation regions W3 and S 140 with the KOSMA telescope on Gornergrat. We have measured maps of both for HCO^+(4-3) and HCO^+(3-2) transition. For W3, a map was also made for the ^{13}CO(2-1) and ^{12}CO(3-2) transition. A cut through S 140 was made using a position switching measurement. The column density and excitation temperature were determined under the assumption of a local thermal equilibrium (LTE). We have estimated the cosmic ray ionization rate using a simple chemical network. The problem of the smoothed out observation due to the low angular resolution of KOSMA is dicussed and the size of the emitting area was determined. The used molecular data for all calculated transitions and the recorded spectra of the KOSMA observations are given in the appendix.

2 Young Stellar Objects

2.1 Star formation

Since ever mankind have asked where stars come from. Or have they always been on the firmament? For a long time measuring instruments were not accurate enough to answer this question. Only for the past few decades, technical progress made this question accessible to astrophysics. The observation of star formation involves many magnitudes of sizes, temperatures and densities. In the earliest stages of star birth, these regions do only emit wavelengths that are difficult or impossible to observe from ground based telescopes. The later discussed Herschel satellite telescope will contribute further data to answer this question in a few years.

In this section, we will review the elementary steps of star formation, following the current standard theory of star formation (after Shu et al. 1987). We also refer to Benz & Güdel (2005) for this section. We will first discuss the evolution of low-mass stars ($M \leq 2M_{\odot}$) and then give the differences to the formation of high-mass stars.

Formation of low-mass stars

The basic material for new born stars can be found in big dark molecular clouds, made out of molecules and dust grains. These clouds consist of ≈ 63 % H_2, ≈ 36 % He, and ≈ 1 % of dust (mass fractions), other molecules and atoms. Not like terestrial dust, the dust in the interstellar medium is largely made up of of amorphous carbon or graphite, aromatic hydrocarbons, silicates, silicon carbide, and possibly iron particles, metallic oxides, and sulfides. Since the temperature in these clouds is only some tenth Kelvin, dust is often mantled by water ice or ice of other molecules. Two different types of molecular clouds can be dinstinguished, dark clouds and giant molecular clouds (GMCs): We can observe the GMCs as the origin of star cluster with low-mass (A-, F- and G-stars) as well as high-mass stars (O-, B- and A-stars), whereas the dark clouds only give birth to low-mass stars. Examples for GMCs are the Orion nebular and for dark clouds the Taurus Molecular cloud or the Ophiuchus molcular cloud in which the later discussed object IRAS 16293-2422 can be found. Table 1 gives an overview of the physical conditions inside the clouds.

		GMC	Dark Clouds
Cloud	∅ [pc]	3 - 20	0.2 - 4
	ρ [cm^{-1}]	10^3 - 10^4	10^2 - 10^4
	M [M$_\odot$]	10^3 - 10^4	5 - 500
	T [K]	15 - 40	8 - 15
Core	∅ [pc]	0.5 - 3	0.1 - 0.4
	ρ [cm^{-1}]	10^4 - 10^6	10^4 - 10^5
	M [M$_\odot$]	10 - 10^3	0.3 - 10
	T [K]	30 - 100	10

Table 1: Physical conditions in differnt types of molecular clouds. (After Benz & Güdel 2005)

The first step from a molecular cloud to a new star are cores condensed out of a molecular cloud by some not yet known mechanism (Fig. 2/1). One possible mechanism that forms such cores could be shockwaves from a "nearby" supernovae. Self gravity forces cores to collapse further, but magnetic fields and turbulences act against the collapse. It is only possible to contract further by a slow leakage of magnetic and turbulent support by ambipolar diffusion. As the density rises, molecules can freeze out on dust and form an icy mantle. This lasts for a time scale of about 10^7 years. Table 1 lists the physical properties of the cores.

In a next step, the core passes the brink of instability where the core starts to collapse from "inside-out" (Fig. 2/2). A protostar and a disk are formed, deeply embedded within an infalling envelope of dust and gas. The protostar heats the surrounding material, leading to peculiar chemical reactions inside the cloud. As the icy grain mantles evaporate, the molecular gas is enriched with species like H_2O, CH_3OH and CO_2. In this initial, so called Class 0 phase, the young star is still highly obscured and only visible at millimeter and sub-millimeter wavelengths. The protostar accretes most of its matter from the natal cloud and lasts for about 10^4 years in this stage. In the following Class I phase, the accretion decreases and the protostellar mass is close to the final mass. The phase lasts for some 10^5 - 10^6 years.

Later on, deuterium will eventually ignite in the central regions. The star forms a stellar wind, rushing through the channels of weakest resistance - the rotational poles - leading to collimated jets and bipolar outflows (Fig. 2/3). The mainly neutral wind pushes molecular gas away, leading to shocks where a more complex chemistry can produce molecules like H_2O, SiO, CH_3CN, HCN, HCO^+, SO, SO_2. For some 10^5 years, the star stays in this stages, which we may call a Class I-II - object.

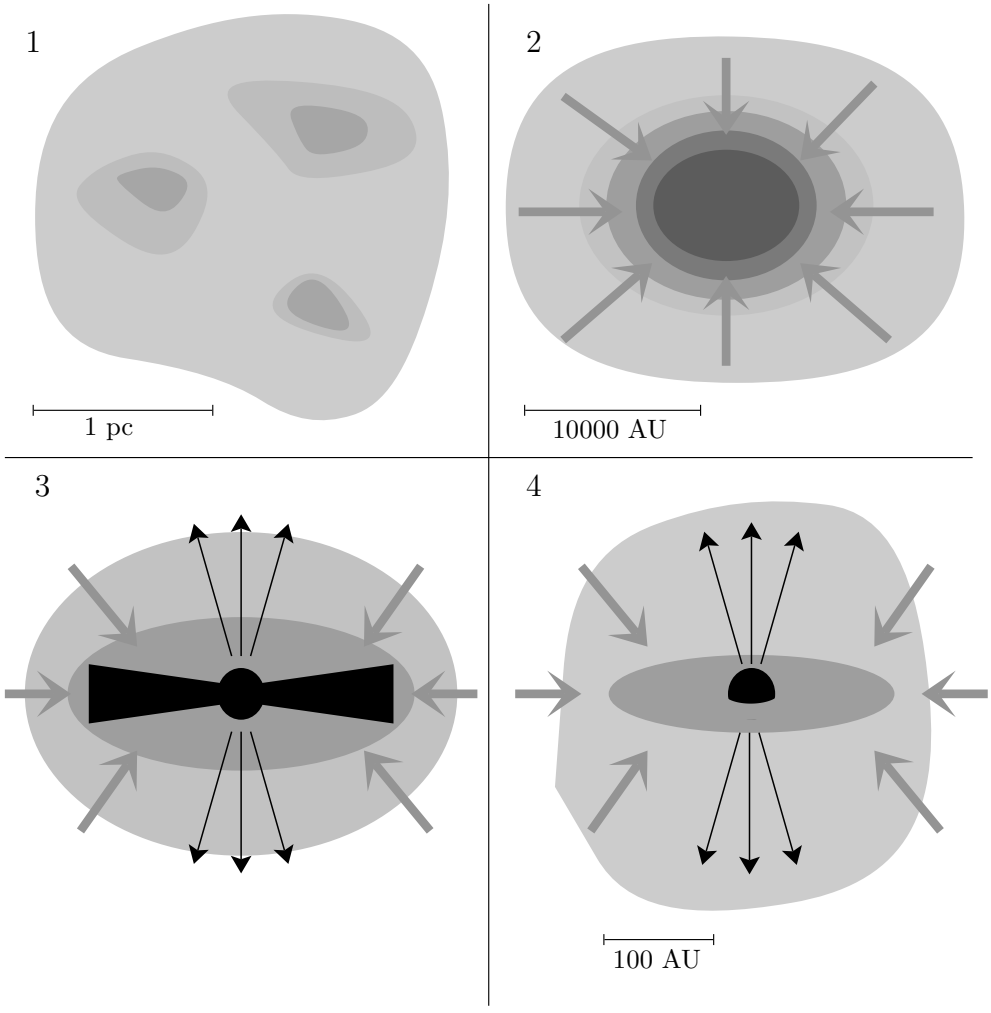

Figure 2: Four stages of star formation: (1) Dark cloud cores embedded in large molecular clouds. (2) Gravitational collaps of the cores (3) Stellar wind forms a bipolar outflow to the north and south pole of the young star. (4) The envelope is disappeared and the disk remains. (after Shu et al. 1987)

In the fourth picture (Fig. 2/4), the star has formed and emits X-rays and UV photons that might interact with the surrounding material. This radiation is already confirmed for Class I objects, but it is not yet sure whether Class 0 objects do also emit this wavelengths. The opening angle of the wind will widen with time and the accretion rate decreases. We can finally observe the new born star directly, still surrounded by a disk where a planetary system can form. A so called T-Tauri star has formed corresponding to a Class II object. The star lasts for some 10^6 years in this phase and will later move on to a post T-Tauri star. The optical thick inner disk then disappears. The outflow vanishs and the new born star evolves towards a main-sequence star.

Formation of high-mass stars

The evolution of low-mass stars can be considered as a sequence of the steps mentioned above, whereas a new formed high-mass star already reaches the main-sequence when the molecular cloud is still collapsing. Young pre-main-sequence high-mass stars can be deeply embedded in their cloud and are therefore not accessible to direct observations. Because of this and due to the large number of low-mass stars ($\approx$ 90 %) we know more about their formation. When high-mass stars start the deuterium burning, they have a strong UV radiation that ionizes the cloud and forms HII - regions. They can disintegrate molecular clouds and therefore avoid further star formation in this area. It is therefore suggested, that massive stars form synchronously, since the first star would destroy the sourrounding dense gas clump before other cores have a chance to collapse. Because the evolution from the collaps to the main sequence proceeds quickly, the fusion provides enough pressure to hold against the gravitation. Disks around high-mass stars have only been reported recently and indicate a short period of equilibrium between centrifugal force and gravitation.

Spectral classification of low-mass Young Stellar Objects

We will concentrate in this section on low-mass stars ($M \leq 2M_\odot$), since for high-mass stars the steps discussed above elapse simultaneously rather than one after another. Low-mass stars are deeply embedded in their cloud and before the T-Tauri phase optically not observable. Most of the radiation in this state comes from absorption in the cloud and reemission in IR and mm-wavelengths. The observed spectra is therefore dependent on the temperature and luminosity of the star, the gas density and dust surrounding it. The spectra can therefore be taken as an indicator for the evolution of the star.

We can distinguish 3 different spectral classes from their spectral energy distribution (Lada 1987):

$$\nu \cdot F_\nu \sim \nu^{-\alpha} \tag{1}$$

The flux density F_ν [Energy / Time · Frequency] as well as the spectral index α depend on the frequency ν and $\nu \cdot F_\nu$ acts as an indicator for the emitted power. The spectral index α is measured in the near IR at a wavelength of 2.2 μm.

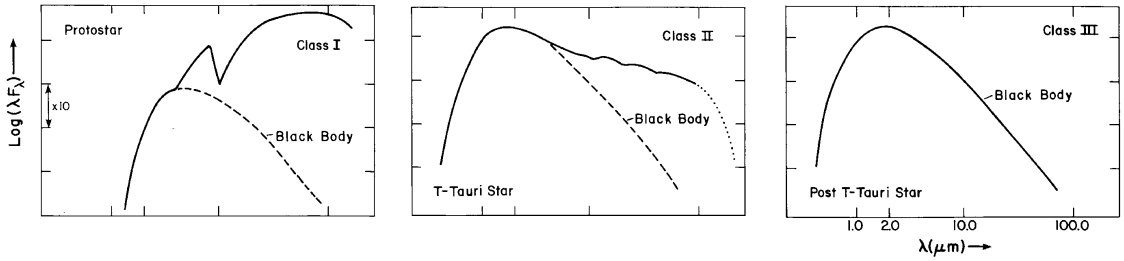

Figure 3: Spectra of Class I, II & III Young Stellar Objects (from Lada 1987)

YSOs can be arranged into 4 classes, that are successive passed through in the case of low-mass stars. A forth class, the so called Class 0, has been introduceed, since objects without emission at

2.2 μm were found.

Class 0: Objects without emission at 2.2 μm.
Objects that only emit at FIR and in mm-wavelength with $\lambda > 10\,\mu m$.

Class I: Spectral index $\alpha > 0$
Spectra with a large amout of radiation in the IR between 10 μm and 100 μm. Emitted by Protostars that are still deeply embedded in their cloud (Fig. 2/2).

Class II: Spectral index $\alpha < 0$
Superposition of the black-body radiation from the T-Tauri star and an excess in IR wavelengths, due to emission from the accretion disk (Fig. 2/4).

Class III: Spectral index $\alpha < 0$
Spectra of post T-Tauri stars can be described by a black body spectra with a well defined surface temperature.

2.2 Interstellar chemistry

For a long time, it was believed that molecules cannot exist in the interstellar medium due to the interstellar radiation field. It was therefore a surprise about seventy years ago, when CH^+ was detected as the first molecule in the interstellar medium. Today we know that dust particles can shield molecules from beeing destroyed by the radiation field. More than 130 molecules[1] have been detected in the interstellar medium over the last few decades. Among them are simple diatomic molecules (e.g. CH, OH) as well as the largest ever detected species $HC_{11}N$ with 13 atoms. We will give a short introduction to the chemical evolution around YSOs following Caselli (2005). Another comprehensive review of the topic can be found in van Dishoeck & Blake (1998).

The first task in calculating the chemical aboundances of molecules around a forming star is to determine initial abundances of molecules and atoms at a specif point of evolution. Besides the bulk species of the gas (H_2, He, CO, H_2O, CO_2 and N_2), the abundances of less common molecules and atoms such as S, Ca, Cr and Ni have to be assumed. For some species, this is not accurately possible (van der Tak 2005): It is not yet clear whether the main oxygen carrier is in the form of H_2O, O or O_2 and the main nitrogen carrier is also uncertain, since N_2 has no permanent dipole moment and N has no fine structure lines and can thus not be observed easily. It has also to be taken in account, that several molecules (e.g. CO_2, H_2O, H_2S, H_2CO and CH_3OH) are frozen out onto dust grains at temperatures below 100 K.

After a set of initial abundances is assumed, the time variation of species has to be calculated. The "rate-equations" need therefore to be solved. They characterise reactions between species quantitative by the rate coefficients. We will first give an introduction to different types of reactions and then discuss the equation that describes them.

Gas-phase chemistry

The main processes happening in the gas phase are:

Ion-molecule reactions: The production of ions in dark molecular clouds is mainly initiated by cosmic rays (c.r.) which ionize H_2. The ionisation rate due to cosmic rays is called ζ and typically of order 10^{-17} s^{-1}. Reactions between ions and neutral species like

$$A^+ + B \rightarrow C^+ + D \tag{2}$$

can then occur. A new formed $H_2{}^+$ reacts with H_2 to $H_3{}^+$, the key to a fast ion-molecule chemistry network (Herbst 2001): Since $H_3{}^+$ can perform proton transfer reactions with many different species A,

[1] A constantly updated list of interstellar molecules can be found at www.astrochemistry.net.

$$H_3^+ + A \rightarrow AH^+ + H_2 \tag{3}$$

this network produces complex molecules like OH, H_2O, HCO^+ and CO.

Typical rate coefficients for ion-molecule reactions in star forming regions are of order 10^{-9} cm^3 s^{-1}. Since H_2 is the most abundant molecule, other reactions are far less frequent. Due to activation energies for some reactions, H_2 will not always react with molecular ions (e.g., SH^+ with H_2, c.f. later).

Dissociative recombination: Reactions between ions and electrons

$$AB^+ + e^- \rightarrow A + B \tag{4}$$

have large rate coefficients of about 10^{-6} cm^3 s^{-1} due to Coulomb attraction. Since the electron abundance in dense clouds is low, recombination cannot compete with reactions with H_2. One example for this reaction is the fusion of H_3O^+ with an electron leading to

$$\begin{aligned} H_3O^+ + e^- &\rightarrow H_2O + H & (5)\\ &\rightarrow OH + 2H \quad \text{or} \quad OH + H_2 & (6) \end{aligned}$$

The fraction of H_3O^+ which will produce H_2O or OH upon dissociative recombination is called the branching ratio.

Radiative association: As the time for interactions between two neutral molecules is fairly short ($\approx 10^{-12}$ s), the reaction

$$A + B \rightarrow AB + h\nu \tag{7}$$

can only be successful, if the radiative process is very fast. This is the case for only a few species like CH, but not for H_2 which can therefore not be formed by a direct association of two H atoms. Typical rate coefficients are of order 10^{-16} - 10^{-9} cm^3 s^{-1}.

Neutral reactions: Reactions between neutral molecues like

$$A + B \rightarrow C + D \tag{8}$$

typically possess substantial activation barriers (≈ 0.1 eV, compared to $k_BT \approx 0.01$ eV at T=100 K) and thus become only important in high temperature regions. An important example are the reaction of O and OH with H_2 that binds all oxygen not locked in CO in H_2O at temperatures above 300 K (van der Tak 2005). Reaction rates are between 10^{-12} and 10^{-10} cm^3 s^{-1}.

Photodissociation: The destruction of molecules through UV photons

$$AB + h\nu \rightarrow A + B \tag{9}$$

can take place at rates of about 10^{-9} s^{-1}. UV radiation can either come from the new born star or from radiative de-excitations following collisional excitation of H_2 and He by cosmic rays or X-ray photons (c.f. Sect. 2.3) or from the interstellar radiation field (ISRF).

Charge transfer: The exchange of an electron in the reaction

$$A^+ + B \rightarrow A + B^+ \tag{10}$$

plays for example in the cosmic ray induced chemical network a role, when O changes its charge with H^+. The rates for such exchanges are approximately 10^{-9} cm^3 s^{-1}.

Surface chemistry

Another important role in the formation of molecules are reactions on grain surfaces (Stäuber 2003): Once a light atom A (e.g. H) hits the dust surface, it is absorbed in a binding site. The light species can move across the surface by thermal hopping or quantum tunneling and strike another atom or molecule B. A and B can form a molecule AB that eventually evaporates from the surface. Call S the probability, that a molecule AB is revealed from the grain after a species A has hit it. The rate R_g [cm^{-3} s^{-1}] of this reaction

$$\mathrm{A} + \mathrm{B} : g \rightarrow \mathrm{AB} + g \tag{11}$$

can be calculated from the densities of A and B, $n(A)$ and $n(B)$, the cross-section σ_g between the dust and the molecules and the difference of the velocities Δv by

$$R_g = n(\mathrm{A})n(\mathrm{B})\sigma_g S \Delta v \quad . \tag{12}$$

Hollenbach & Salpeter have used this principle in 1971 to explain the large amount of H_2 in the interstellar medium. In fact, the rate of the reaction for the H_2 forming on dust is at 10 K about 8 orders of magnitude larger than for radiative association. Chemistry on dust grains can also be used to explain the large abundances of complex species near star forming regions and the enhancement of selected molecules along molecular outflows. This is not restricted on reaction with H_2, e.g. C and O can form CO on grain surfaces (Lequeux et al. 2005).

Chemical network

The reaction A + B → X can be described by the density of the species A and B, $n(A)$ and $n(B)$ and a rate coefficient k [cm^3 s^{-1}] with the rate equation

$$\frac{dn(\mathrm{X})}{dt} = k \cdot n(\mathrm{A}) \cdot n(\mathrm{B}) \ . \tag{13}$$

The rate k is given by averaging over the thermal distribution of the relative velocity v of the two reactants times the total cross section σ:

$$k = < \sigma \cdot v > \tag{14}$$

Many chemical reactions involve the breaking of chemical bonds, before new ones can be formed. Most chemical reactions have therefore appreciable activation energies E_a even if they are exothermic. Hence the rate can be expressed by the Arrhenius law

$$k = A(T) e^{-E_a/k_B T} \ , \tag{15}$$

where A(T) is a "pre-exponential factor", a weak function of the temperature, depending on the actual shape of the reaction potential surface. The activation energy can be as large as 0.1 - 1 eV for some reactions which might therefore not proceed in dark clouds with $k_B T \sim 0.01\,\mathrm{eV}$.

If we take several species and unimolecular processes involving photons and cosmic rays into account, we can rewrite equation (13) as[2]

$$\frac{dn(i)}{dt} = \sum_j l_{ij} n(j) + \sum_{l,m} k_{ilm} n(l) n(m) \ . \tag{16}$$

This set of equation represents a large chemical network that describes the time-dependent density $n(i)$. Besides the initial abundances for each species, the temperature and density distribution as well as the cosmic ray ionisation rate (ζ), the far ultraviolet (FUV) radiation field from inside and outside and the X-ray flux have to be assumed.

[2] A rate coefficent l for reactions like $\mathrm{A} + h\nu \rightarrow \mathrm{A}^+$ can be defined from the equation $\frac{dn(\mathrm{A}^+)}{dt} = kn(\mathrm{A})$.

2.3 Radiation induced chemistry

Young stars, still deeply embedded in their natal molecular cloud, start emitting high energetic radiation like FUV and X-ray photons after a not yet known point of evolution. Photons with FUV energies (6 - 13.6 eV) and X-ray photons (above $\approx$ 1 keV) can enter the surrounding cloud and alter their chemical composition. Fig. 4 shows the penetration depth of radiation into the cloud at various wavelengths.

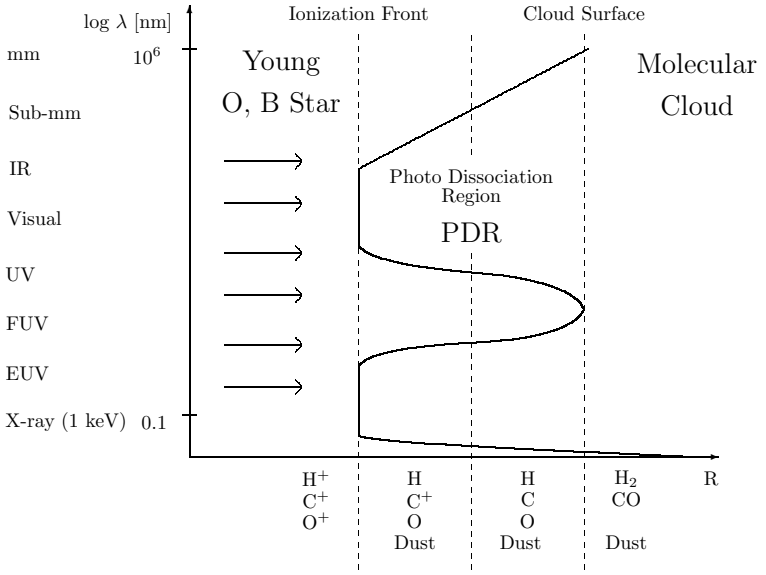

Figure 4: Depth of penetration of the young stellars radiation field into the molecular cloud for different wavelengths. (after Benz & Güdel 2005)

FUV radiation

The influence of FUV radiation from the central source with energies between 6 eV and 13.6 eV on the envelope around Young Stellar Objects was studied by Stäuber et al. (2004a) to which we will refer in this section. Photons with such energies can ionize several atoms and molecules as well as break chemical bonds. Higher gas temperatures due to strong FUV radiation can lead to an evaporation of H_2O from gas in the inner region and thus also alter the chemical equilibrium. We introduce this radiation field into the chemical network by an unimolecular reaction with the rate coefficient

$$k_{UV} = G_{0,in}\ C\, e^{\gamma\, \tau_{in}} + G_{0,out}\ C\, e^{\gamma\, \tau_{out}}\ . \tag{17}$$

The so called "enhancement factor" $G_{0,in}$ due to a central UV source and that for the outer radiation $G_{0,out}$ are characterized in units of the average interstellar radiation flux (ISRF) at the same energy ($1.6 \cdot 10^{-3}$ erg cm^{-2} s^{-1}). C and γ are fit parameters and τ_{in}, τ_{out} attenuation factors proportional to the hydrogen column density $N(H_{tot}) = 2N(H_2) + N(HI)$. We can neglect interaction with other species, as hydrogen is by far most abundant. Due to the high hydrogen density in the inner region, FUV photons are absorbed very quickly and FUV radiation has only an influence on the chemistry in the inner regions up to radii of a few hundred AUs.

The outer UV flux $G_{0,out}$ can be considered as 1, but care has to be taken if the YSO is situated in a region of high-mass star formation. Inner radiation fluxes $G_{0,in}$ can be as large as 10^5. It was found that the column density of several species e.g. CH, CH^+ and OH are strongly enhanced and other molecules like HCO^+ and HCS^+ are not so much changed.

X-Rays

We follow Stäuber et al. (2005a) in this section: Observations of Young Stellar Objects show that some Class I objects are very strong X-ray emitters. Stars in this phase are still deeply embedded in a cloud and therefore X-rays are not directly observable. But due to a small atomic and molecular cross sections at high energies, X-rays can penetrate deeper into the envelope than FUV photons: Whereas the FUV can affect a region of 200 - 300 AU, X-rays can advance up to radii of about 1000 AU. No X-ray detection has been reported yet toward Class 0 objects, but the influence of X-rays to the chemistry of the surrounding envelope is studied in order to draw conclusions from the chemical abundance to the X-ray flux.

X-rays are emitted by hot plasma (e.g., $3 \cdot 10^7$ K for an 2.6 keV X-ray photon) which is heated by a mechanism that is not well understood. In low-mass stars, powerful magnetic activities on the stellar surface may heat the plasma while in high-mass stars wind instabilities and shocks are possible heaters. The X-ray spectra [photons s^{-1} cm^{-2} eV^{-1}] can be assumed as a thermal spectrum

$$F_X(E) = F_0\, e^{-E/kT_x} \ , \tag{18}$$

with T_X, the temperature of the X-ray emitting plasma, assumed to be between $3 \cdot 10^7$ K and $1 \cdot 10^8$ K. The factor F_0 can be evaluated from the X-ray luminosity L_X and the radius r of the cloud:

$$L_X \equiv 4\pi r^2 \int F_X(E) E dE \tag{19}$$

Since photons with energy lower than 1 keV are absorbed in the inner region and photons with energies above 100 keV contribute marginally to the total integrated X-ray flux, the integral in Eq. (19) can be evaluated between this two energies. Typical X-ray luminosities range from approximately 10^{28} to 10^{33} erg s^{-1}.

The local X-ray flux can be expressed by

$$F(E, r) = F_X(E) e^{-\tau(E)} \ , \tag{20}$$

where $\tau(E)$ is the total X-ray attenuation. X-ray photons with energies below 10 keV are attenuated through photoabsorption and at high energy through Compton scattering. It was however shown, that the influence of Compton scattering to the chemistry is negliable. The attenuation can be expressed by the cross section σ_i and the fractional abundance $x(i)$ of a species i by $\tau_P(E) = N_H \sum x(i)\sigma_i(E)$. The sum has to be taken over all regarded species.

X-Ray induced chemistry

Like cosmic rays, X-rays affect the chemistry mainly by ionizing and dissociating several species (Stäuber et al. 2004b): Beside a direct ionization of atoms and molecules by X-ray photons, fast electrons coming from the "primary" process can ionize mainly H_2 and excite H, He and H_2. As the excited molecules decay back to the ground state, they emit UV photons that can photoionize and photodissociate further. This "secondary" processes are far more important for the chemical network than the primary interaction of the X-rays with the gas, since the ionization of H_2 by X-ray is 1000 times slower then the relevant chemical reactions and 10 times slower then electron impact ionizations.

The most important parameter in the chemistry and physics of X-ray governed areas (called X-ray dominated regions XDRs) is H_X / n, the X-ray deposition rate per particle, defined by

$$H_X \equiv \int F(E, r)\sigma(E) E dE \ . \tag{21}$$

Even at points close to the central source (≈ 200 AU), H_X is low due to absorption and geometrical dilution. Therefore additional heating of the gas by X-rays can be neglected in most cases and we

will later use the approximation $T_{Gas} \approx T_{Dust}$.

In order to estimate the X-ray flux out of observations of the chemical structure, it is essential to find molecules that are more sensitive to X-rays than to FUV radiation: It was shown by Stäuber et al. (2004b) that species like HCO^+, SH^+ (among others) are more enhanced by X-rays than by FUV photons even for X-ray luminosities as low as 10^{30} erg s^{-1}. Other species like SH are either enhanced by FUV or X-rays and it is therefore difficult to relate the effect to the radiation.

3 Radiative transfer

The physical conditions of a molecular cloud, for example the density and the gas temperature, can be constrained from a recorded spectra. Therefore, we calculate the emitted spectra of a radiating area depending on various parameters and vary them until the calculation fits the observed data. In the following section, we will discuss the basic physics and algorithms of radiative transfer problems. We will assume a simple 2-energy-level-system but of course the formalism can be easily extended to an arbitrary number of levels.

3.1 The radiative transfer equation

The specific intensity of one particular line I_ν $[erg\,s^{-1}\,cm^{-2}\,Hz^{-1}sr^{-1}]$ at the frequency ν changes along the line of sight inside the cloud in a infinitesimal element ds as (Genzel 1991)

$$\frac{dI_\nu}{ds} = \epsilon_\nu - \kappa_\nu\, I_\nu \ . \tag{22}$$

The first term on the right-hand side of (22) represents the emission and the second term denotes the absorption. We can express the absorption coefficient κ_ν $[cm^{-1}]$ and the emission coefficient j_ν $[erg\,s^{-1}\,cm^{-3}\,Hz^{-1}sr^{-1}]$ in terms of microscopic quantities, the Einstein-Coefficients. For a spontaneous transition from an upper level (u) to a lower level (l), the emission coefficient ϵ_ν can be written as

$$\epsilon_\nu = \frac{h\nu}{4\pi}\phi(\nu) n_u A_{ul} \ , \tag{23}$$

where the Einstein-A-Coefficient A_{ul} $[s^{-1}]$ expresses the transition probability between the two considered levels (Fig. 6). Using Fermi's Golden Rule A_{ul} can be calculated from a transition moment (matrix element) d_{ul}. If we take only electric dipol-transitions into account, the required matrix elements is $d_{ul} = \langle \psi_u \,|X|\, \psi_l \rangle$, with the dipol-operator X. The dipol transition moment is defined as $\mu \equiv q \cdot |d_{ul}|$ and measured in units of Debye (1 Debye = 10^{-18} cm esu). We can then express the Einstein-A-Coefficient as (e.g. in Sigrist 2003 or Schwabl 2002)

$$A_{ul} = \frac{64\pi^4}{3hc^3}\mu^2\nu_{ul}^3 \ . \tag{24}$$

For a rotational transition $J \rightarrow J-1$, the dipol transition moment is related to the classical electric dipol moment μ_{el} as

$$\mu^2_{J+1\rightarrow J} = \frac{J+1}{2J+3}\mu^2_{el} \ , \tag{25}$$

however one has to take care of fine-structure and hyperfine-structure transitions[3].

The emission ϵ_ν and the absorption κ_ν can also be expressed in microscopic quantities, the Einstein-B-Coefficients B_{ul} and B_{lu} (Fig. 6)

$$\kappa_\nu = \frac{h\nu}{4\pi}\phi(\nu)(n_u B_{ul} - n_l B_{lu}) \ , \tag{26}$$

where $B_{ul}I_\nu$ and $B_{lu}I_\nu$ give the corresponding rates $[\mathrm{s}^{-1}]$ per molecule.

The A_{ul} and B_{ul} (resp. B_{lu}) are coupled by the so called Einstein-Relations. A comparison of the later discussed rate equations with the Planck function shows that

$$A_{ul} = \frac{2h\nu^3}{c^2}B_{ul} \tag{27}$$

$$B_{ul}g_u = B_{lu}g_l \ . \tag{28}$$

[3] A generalisation of equation (25) can be found in Whiting et al. (1974), however it is more convenient to use the SPCAT code to calculate line intensities (Pickett 1991).

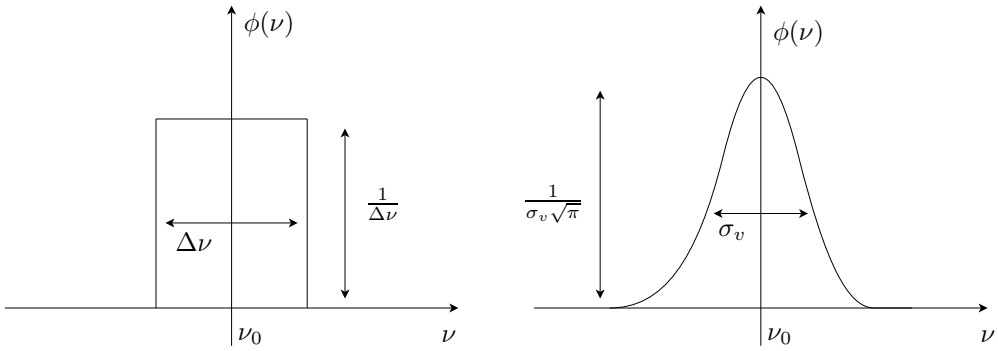

Figure 5: A Gaussian (left) and a rectangular line shape function.

Since the Einstein-Coefficients depend only on microscopic quantities, these relations are also valid if no thermodynamical equilibrium is assumed as for the derivation of the Planck function.

The line shape function $\phi(\nu)$ gives the probability that a photon is emitted at the frequency interval $[\nu, \nu + d\nu]$ ($\int \phi(\nu) d\nu = 1$). As a simple approximation for $\phi(\nu)$, one often uses a rectangle-function with width $\Delta\nu$ and height $\frac{1}{\Delta\nu}$

$$\phi(\nu) = \frac{1}{\Delta\nu} \chi_{[\nu_0 - \frac{1}{2}\Delta\nu, \nu_0 + \frac{1}{2}\Delta\nu]}(\nu) \ , \tag{29}$$

with the characteristic function χ (Fig. 5). The center of the line can be Doppler shifted to $\nu = \nu_0 \frac{v}{c}$ due to motion of the emitting molecule. This rectangular line profile is also used to express the line equivalent width. Another important line shape function is the Gaussian or Doppler profile

$$\phi(\nu) = \frac{1}{\sigma_v \sqrt{\pi}} \cdot exp\left(- \left(\frac{\nu - \nu_{ul} - \vec{v} \cdot \vec{n} \frac{\nu_{ul}}{c}}{\sigma_v} \right)^2 \right) \ . \tag{30}$$

The center is again shifted from ν_{ul} by a velocity field $\vec{v}$ and the width[4] σ_v is determined from the local kinetic temperature T and microturbulences v_{MT} as

$$\sigma_v = \sqrt{\left(\frac{2kT}{m} \right)^2 + v_{MT}^2} \ . \tag{31}$$

Another important quantity is the source function S_ν, given by

$$S_\nu \equiv \frac{\epsilon_\nu}{\kappa_\nu} = \frac{2h\nu^3}{c^2} \left(\frac{g_u n_l}{g_l n_u} - 1 \right)^{-1} \ . \tag{32}$$

In local thermodynamic equilibrium (LTE), the populations of the lower and upper state n_l and n_u are given through a thermal (Boltzmann) popultion

$$\frac{n_u}{n_l} = \frac{g_u}{g_l} e^{-\frac{h\nu}{kT}} \ . \tag{33}$$

The source function is then equal to the Planck function

$$S_\nu = B_\nu(T) \equiv \frac{2h\nu^3}{c^2} \frac{1}{e^{\frac{h\nu}{kT}} - 1} \ . \tag{34}$$

In the interstellar medium, LTE is rarely fulfilled but one can still write the population distribution in the form of equation (34) by defining the excitation temperature T_{ex} as

$$\frac{n_u}{n_l} = \frac{g_u}{g_l} e^{-\frac{h\nu}{kT_{ex}}} \ . \tag{35}$$

[4]The full width at half maximum FWHM is related to σ_v by $FWHM = \sigma_v \cdot 2\sqrt{ln(2)}$

A change of the variable $d\tau \equiv \kappa_\nu ds$ leads to the definition of the optical depth τ_ν

$$\tau_\nu(z) \equiv -\int_0^z \kappa_\nu ds \ . \tag{36}$$

The radiative transfer equation (22) can then be rewritten as

$$\frac{dI_\nu}{d\tau_\nu} = \frac{\epsilon_\nu}{\kappa_\nu} - I_\nu = S_\nu - I_\nu \ , \tag{37}$$

using equation (32). This equation can be easily integrated. The integration constant $I_{\nu,BG}$ is the background intensity (e.g. the 2.7 K cosmic microwave background radiation):

$$I_\nu = I_{\nu,BG}\, e^{-\tau_\nu} + \int_0^{\tau_\nu} S_\nu(\tau_\nu')e^{-\tau_\nu'} d\tau_\nu' \tag{38}$$

If we assume a spatially constant population (S_ν resp. T_{ex} are not dependent on s) this equation leads to

$$I_\nu = I_{\nu,BG}\, e^{-\tau_\nu} + S_\nu(1 - e^{-\tau_\nu}) \ . \tag{39}$$

For radio and submillimeter frequency $h\nu \ll kT$ and therefore the Rayleigh-Jeans approximation $e^{\frac{h\nu}{kT}} \approx 1 + \frac{h\nu}{kT}$ is applicable. In this approximation, intensities can be expressed in terms of the Rayleigh-Jeans equivalent radiation temperature T_{RJ} $[K]$

$$I_\nu = \frac{2k\nu^2}{c^2} T_{RJ} \tag{40}$$

Since atoms or molecules can also be excited or deexcited by collisions with other molecules (mostly H_2), we have to discuss collision rates C_{ul} (resp. C_{lu}) $[s^{-1}]$ (Fig. 6). Because the collision rates must depend linearly on the density of the collison partner n_{col} we can express the rates as

$$C_{ul} = K_{ul} \cdot n_{col} \ , \tag{41}$$

with the collisonal rate coefficient K_{ul} $[cm^3 s^{-1}]$, obtained by integrate the collision cross section over the velocity. Therefore the relative velocities are supposed to be Boltzmann distributed. As for the Einstein-Coefficients, there is a relation between C_{ul} and C_{lu}

$$n_u C_{ul} = n_l C_{lu} \ , \tag{42}$$

the detailed balance relations. Assuming LTE and plugging in (33), this equation leads to

$$C_{lu} = \frac{g_u}{g_l} C_{ul} e^{-\frac{h\nu}{kT}} \ . \tag{43}$$

Since K_{ul} and K_{lu} are microscopical constants this relation is also applicable for systems out of the local thermal equilibrium.

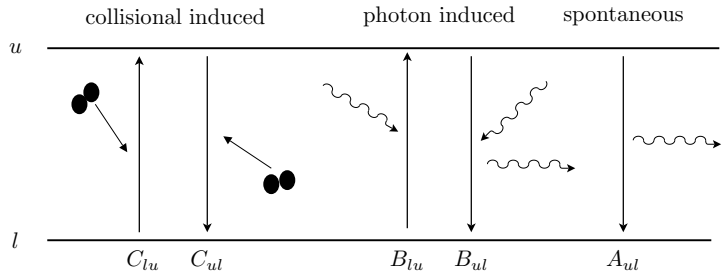

Figure 6: Transitions described by Einstein-Coefficients

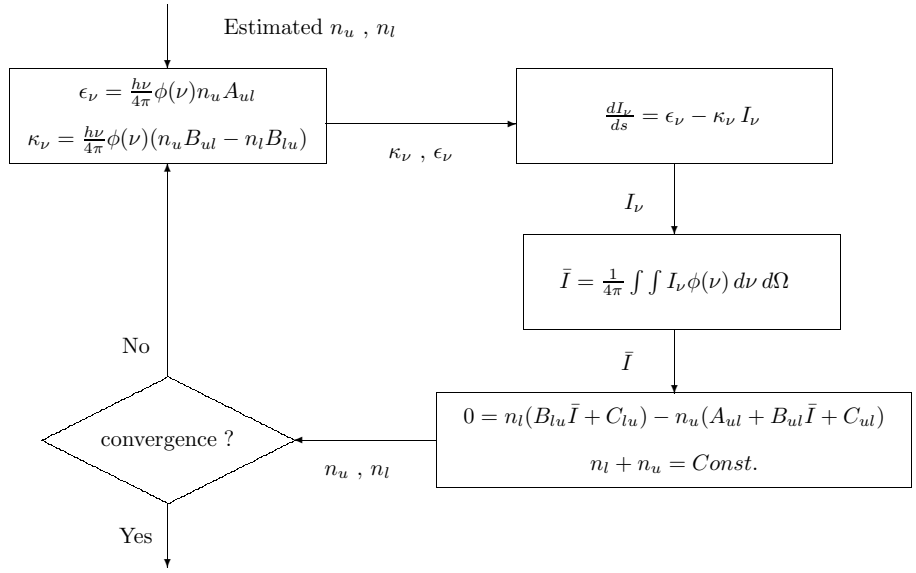

Figure 7: Solving the radiative transfer equation and the equation for statistical equilibrium of a 2 levels-system.

We can now write down the equations of statisical equilibrium for our two level system as

$$\frac{dn_l}{dt} = -n_l(B_{lu}\bar{I} + C_{lu}) + n_u(A_{ul} + B_{ul}\bar{I} + C_{ul}) \quad (44)$$

$$\frac{dn_u}{dt} = n_l(B_{lu}\bar{I} + C_{lu}) - n_u(A_{ul} + B_{ul}\bar{I} + C_{ul}) \ , \quad (45)$$

where $\bar{I}$ is the intensity, integrated over $\phi(\nu)$ and averaged over 4π steradian

$$\bar{I} = \frac{1}{4\pi}\int\int I_\nu \phi(\nu)\, d\nu\, d\Omega \ . \quad (46)$$

Since the intensity I_ν in equation (46) refers on the level population, equations (44/45) and (46) are coupled. In order to solve a radiativ transfer problem, one has to find a way to decouple this set of equations. In the next sections, we will discuss approximations and algorithms to do this. The way in which the physical quantities depend on each other is given in Fig. 7. This figure also shows an iterative approach to solve the radiative transfer problem: Starting with an initial guess for the level population, the equations (23), (26), (22), (46) and (44/45) are solved in this sequence until a self consistent solution is found. This is the so called Lambda Iteration-algorithm, the basic algorithm for the later discussed escape probability and Monte Carlo algorithm.

Besides the gas part of a cloud discussed above, we have to take into account thermal continuum emission from dust $\epsilon_{\nu,DUST}$ and absorption by dust $\kappa_{\nu,DUST}$:

$$\epsilon_\nu = \epsilon_{\nu,GAS} + \epsilon_{\nu,DUST} \quad (47)$$

$$\kappa_\nu = \kappa_{\nu,GAS} + \kappa_{\nu,DUST} \quad (48)$$

If we assume the dust behaves like a black body, the relation between the emission and absorption for a dust temperature T_{Dust} is given by

$$\epsilon_{\nu,DUST} = \kappa_{\nu,DUST} B_\nu(T_{DUST}) \ , \quad (49)$$

with $B_\nu(T_{DUST})$ the Planck function. The absorption can be split up into the density of the dust ρ_{DUST} and the dust opacity per dust mass $\kappa_{DUST}(\nu)$ [5]

[5] In RATRAN, $\kappa_{DUST}(\nu)$ is called κ-function (c.f. Hogerheijde & van der Tak 2000).

$$\kappa_{\nu,DUST} = \kappa_{DUST}(\nu) \cdot \rho_{DUST} \ . \tag{50}$$

Further information on the radiative properties of dust can be found in Lequeux et al. (2005).

3.2 Optically thin radiation

In the case of optically thin radiation, the problem of the coupled equations disappears, since the level population is not affected by the radiation (van Langevelde & van der Tak 2004). It is then possible to write down the equations of statisical equilibrium (44/45) and solve them directly, because the terms of the Einstein-B-Coefficients do not contribute to the transition rates. However background radiation like the 2.7 K CMB can affect the lower level populations of molecules like CO and CS. This can be easily included since the lines are optically thin.

3.3 Local thermal equilibrium

In the assumption of local thermal equilibrium (LTE), the level populations are given by the Boltzmann distribution and the set of equations (44/45) and (46) is decoupled. On earth LTE is present except in special cases (e.g. LASER). In the ISM however, the density is so low that the population cannot be thermalised and natural maser phenomena can occur. For thermalisation, the timescale for collisions must be much shorter than for spontaneous decay

$$\frac{1}{C_{ul}} \ll \frac{1}{A_{ul}} \ . \tag{51}$$

This leads to the definition of the critical density n_{crit} indicating at which density the number of collisions is comparable with the number of spontaneous decays. For densities significantly larger then n_{crit} the LTE assumption is appropriate

$$n \gg n_{crit} \equiv \frac{A_{ul}}{K_{ul}} \ . \tag{52}$$

When lines get optical thick the radiation makes a contribution to the thermalisation and equilibrium is easier established.

In the LTE the source function becomes the Planck function (34)

$$S_\nu = B_\nu(T) \ , \tag{53}$$

and the density of molecules in the level i can be calculated from the total density n_{mol}, the temperature T, the energy of the level E_i and the statistical weight g_i by

$$n_i = n_{mol} \frac{g_i e^{-\frac{E_i}{kT}}}{\sum_{j=0}^{\infty} g_j e^{-\frac{E_j}{kT}}} = n_{mol} \frac{g_i e^{-\frac{E_i}{kT}}}{Q(T)} \ . \tag{54}$$

The sum in the denominator of equation (54) is tabulated in databases as the partition function.

3.4 The escape probability method

Another popular way to decouple the radiative tranfer equation from the calculation of the level population is the so called escape probability method, first introduced by Sobolev. It uses the idea of calculating an approximate $\bar{I}$ out of local conditions only. This is only feasible if the physical conditions do not vary much over the model.

We try to estimate $\bar{I}$ in terms of the probability β, the chance for a newly created photon to escape the cloud. Since for a completely opaque area $\bar{I}$ is equal to the profile averaged source function S, we find

$$\bar{I} = S(1 - \beta) \ . \tag{55}$$

In this approach, the statististical equilibrium equation takes the easy form

$$\frac{dn_u}{dt} = n_l \cdot C_{lu} + n_u \cdot C_{ul} - \beta n_u A_{ul} \ . \tag{56}$$

The only remaining task is to calculate the escape probability β without referring to the radiation field, but taking the geometry and the optical depth into account. In one dimension, this can be done by averaging e^{τ} over the optical depth:

$$\beta =< e^{-\tau} >= \frac{1}{\tau}\int_0^{\tau} e^{-\acute{\tau}} d\acute{\tau} = \frac{1-e^{-\tau}}{\tau} \tag{57}$$

It turns out that this result is also applicable for a quickly expanding sphere. This is the so called Sobolev or large velocity gradient (LVG) approximation.

In order to calculate the level population, we have to apply the following algorithm:

1. Assume n_l and n_u in the LTE-Approximation: (33) and $n_u + n_l = n$
2. Calculate τ using (26) and (36). This gives the escape probability β.
3. The new level population can be calculated.

Step 2 and 3 have to be repeated until the desired convergence is reached (i.e. the solution is self-consistent).

The above-mentioned algorithm is implemented in the `RADEX`-Solver (van Langevelde & van der Tak 2004) and connected to the Leiden Atomic and Molecular Database (LAMDA) (Schöier et al. 2005).

3.5 The Monte Carlo algorithm

Starting with the Lambda Iteration algorithm (Fig. 7), Bernes (1979) deduced an algorithm that uses the Monte Carlo method. The most time consuming step in the Lambda Iteration algorithm is the calculation of the integral (46). Therefore, the complete integration is replaced by a Monte Carlo approximation. In this section, I will follow Bernes (1979). Further technical details can be found in this paper.

The considered cloud is divided into several cells with volume V_m (m indicates the cell). For a spherical symmetric model, shells can be used (Fig. 8). Emitted line photons are represented by a number of model photons, each of them acts as a large number of "real" photons. We further assume the scattering to be incoherent in direction and frequency, i.e. completely redistributed.

After an initial estimation of the upper population in the cell $n_u(m)$, the number of emitted real photons can be derived from the number of emissions per unit volume during one second:

$$N_r(m) = n_u(m) \cdot A_{ul} \tag{58}$$

The relative number of emitted real photons during one second gives the number W_0 of real photons that each model photon represents.

Since we have assumed complete redistribution, a random propagation direction for the model photons is chosen. The photons are allowed to travel a short distance[6] s_1 in the selected direction. The optical depth τ_1 is then approximated by

$$\tau_1 = \frac{h\nu_{ul}}{4\pi}\phi(\nu)(n_u(m)B_{ul} - n_l(m)B_{lu}) \cdot s_1 \ , \tag{59}$$

with the line function $\phi(\nu)$ discussed above. The weight $W(x)$ is originally taken to be W_0 and varies along the path as

[6]This distance as well as the exacte point of emission are chosen randomly

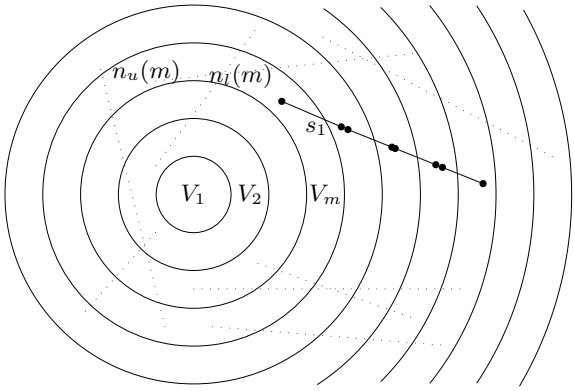

Figure 8: The calculation of the mean radiation $\bar{I}$ using a Monte Carlo algorithm.

$$W(x) = W_0\, exp\left(-\frac{\tau_1 x}{s_1}\right) \ . \tag{60}$$

After a distance s_1 is covered, the value of the weight decreases to $W_0 \cdot exp\,(-\tau_1)$. As the model photon travels along the path it excites and deexcites molecules. The number N_{lu} of excitations along the path is

$$\begin{aligned} N_{lu} &= \frac{h\nu_{ul}}{4\pi}\phi(\nu) n_l(m) B_{lu} \int_0^{s_1} W(x)\, dx & (61)\\ &= \frac{h\nu_{ul}}{4\pi}\phi(\nu) n_l(m) B_{lu} \frac{W_0 s_1}{\tau_1}\left(1 - e^{-\tau_1}\right) \ . & (62) \end{aligned}$$

Since the total number of atoms in the lower state inside cell m is $n_l(m) \cdot V_m$, the number $S_{lu}(m)$ of radiative excitations per atom (caused by this first step of the model photon) is

$$S_{lu}(m) = \frac{N_{lu}}{n_l(m) V_m} \ . \tag{63}$$

This quantity is added to a counter $\Sigma\,[S_{lu}(m)]$. The photons can now move further steps into the same direction until all photons are absorbed or have left the cloud. For every step, the equation (61) and (63) have to be calculated and $\Sigma\,[S_{lu}(m)]$ must be adapted. The step lengths should be chosen so that the physical conditions do not change too much along the path but the model photon crosses a cell boundary.

When all model photons have been emitted and followed, the equation of statistical equilibrium can be set-up and solved

$$n_l\left(\Sigma\,[S_{lu}(m)] + C_{lu}\right) = n_u\left(A_{ul} + \frac{g_l}{g_u}\Sigma\,[S_{lu}(m)] + C_{ul}\right) \ , \tag{64}$$

using the conservation of the number of molecules (i.e. $n_l(m) + n_u(m)$ is constant).

The above mentioned steps have to be repeated, until the level populations have converged. As common for Monte Carlo algorithms, the convergence is of the order $1/\sqrt{N_{Phot}}$ with N_{Phot}, the total number of model photons. Several approaches to accelerate the convergence are carried out in van Zadelhoff et al. (2002) and Hogerheijde & van der Tak (2000).

4 Molecular spectroscopy of diatomic molecules

Molecules consist of several atoms, each built of a core and electrons, held together by their electrons. If the ground state energy of the molecule has a potential minimum that is lower than that of the separated atoms, the molecule can be stable. As atoms, molecules have definite energy-states and radiative emission as well as absorption is only possible in portions of energy differences between two of these energy-states. However, the spectra of molecules is even in the simplest case of a diatomic molecule far more complicated than that of atoms.

In this chapter, we will discuss the basic principles of the spectroscopy of molecules. We will restrict our study to diatomic molecules and temperature regimes around protostars (i.e. up to a few hundred Kelvin). Further details on the topic can be found in Herzberg (1965), Bernath (2002) and Afram (2004), which serve as references for this chapter.

4.1 Energy scales

Different energy states of atoms can be distinguished by the moving state of the electrons and the spin states of the particles. In diatomic molecules, additional modes of movement can occur, which are not possible for a single atom: The molecule can rotate around an axis passing through the center of gravity and the nuclei can vibrate relative to each other. These modes of movement appear at different energy scales, providing the possibility to neglect modes that are "frozen-out" at the considered temperature regime[7].

Another fundamental point in the theory of molecules are the different scales of masses: The mass of nuclei M are 3 to 5 orders of magnitude larger than the mass of the electrons m,

$$\frac{m}{M} \approx 10^{-3} \; - \; 10^{-5} \tag{65}$$

and the rates of movement are therefore also diverse and can be treated as largely independent. This is mathematically realised by the so called Born-Oppenheimer Approximation. Generally, this approximation is very good, but neglects transitions between different electronic states[8] due to the movement of the nuclei. If higher accuracy is needed, such effects have to be considered by using perturbation theory.

We can now roughly estimate the energy scales of the different modes of movement (Sigrist 2003): The electronic energy E_e due to transitions between different energy states of the electronic system can be approximated by using the Heisenberg uncertainty relation as

$$E_e \sim \frac{p^2}{2m} \sim \frac{\hbar^2}{2mR^2} \; , \tag{66}$$

with m, the mass of an electron and R, the internuclear distance. To estimate the vibrational engery E_{vib}, we assume the vibrations of the two atoms towards or away each other to be harmonic (i.e. in a potential $V(r) = \frac{1}{2}M\omega^2 r^2$). Since a deflection of the molecule by R would lead to a potential energy comparable to E_e, we can evaluate ω by

$$M\omega^2 R^2 \sim \frac{\hbar^2}{mR^2} \implies E_{vib} = \hbar\omega \sim \frac{\hbar^2}{\sqrt{Mm}R^2} \sim \sqrt{\frac{m}{M}}E_e \; . \tag{67}$$

The rotational energy E_{rot} for the lowest excited state with angular momentum $\hbar$ is determined by the moment of inertia $I = MR^2$ as

$$E_{rot} = \frac{\hbar l(l+1)}{2I} \sim \frac{\hbar^2}{MR^2} \sim \frac{m}{M}E_e \; , \tag{68}$$

[7] Modes with energies far lower than $E = k_B \cdot T$ are fixed to their ground state

[8] Those matrix-elements are suppressed by a factor of $\sqrt{m/M}$.

and therefore, the ratio between the 3 different types of movement is

$$E_e : E_{vib} : E_{rot} \approx E_e : \sqrt{\frac{m}{M}} E_e : \frac{m}{M} E_e \ . \tag{69}$$

In a H_2 molecule, the internuclear distance is 1.06 Å and the electronic energy after Eq. (66) 3.4 eV $\approx$ 40000 K. For vibrational and rotational states, the excitation temperatures are therefore about 920 K and 20 K, respectively. We will therefore only consider rotational states in this work, since the temperature in shells around YSOs is in general too low to excite vibrational or electronic states.

In spectroscopy, energy is ofter expressed in units of [cm^{-1}]: This definition is motivated by the relation

$$\tilde{\nu} = \frac{\nu}{c} \text{ and } E = h\tilde{\nu}c \ \Rightarrow \frac{E}{hc} = \tilde{\nu} \ , \tag{70}$$

with the energy E [J] and

$$\begin{aligned} \lambda &\equiv \text{wavelength } [cm] \\ \nu &\equiv \text{frequency } [Hz = s^{-1}] \\ \tilde{\nu} &\equiv \text{wavenumber } [cm^{-1}] \ . \end{aligned}$$

An overview of the vibrational and rotational energy states gives Fig. 9, the potential curve of the internuclar force: Upon different vibrational levels (labeled by $\nu = 0, 1, 2, \ldots$) rotational levels $J_\nu = 0, 1, 2, \ldots$ emerge. The potential curve can be described by a parabola for low vibrational states and the radial motion of the atoms is therefore harmonic. In higher states, this approximation is not longer justified, since in an actual molecule the energy goes to a constant value E_D, when the atoms are at great distance from each other. Energies above E_D lead to a dissociation of the molecule or to a higher electronic state if a transition is possible. Beside pure rotational transitions and vibrational transitions, intermediate cases, called ro-vibrational transitions, with change of both vibrational and rotational state can occure.

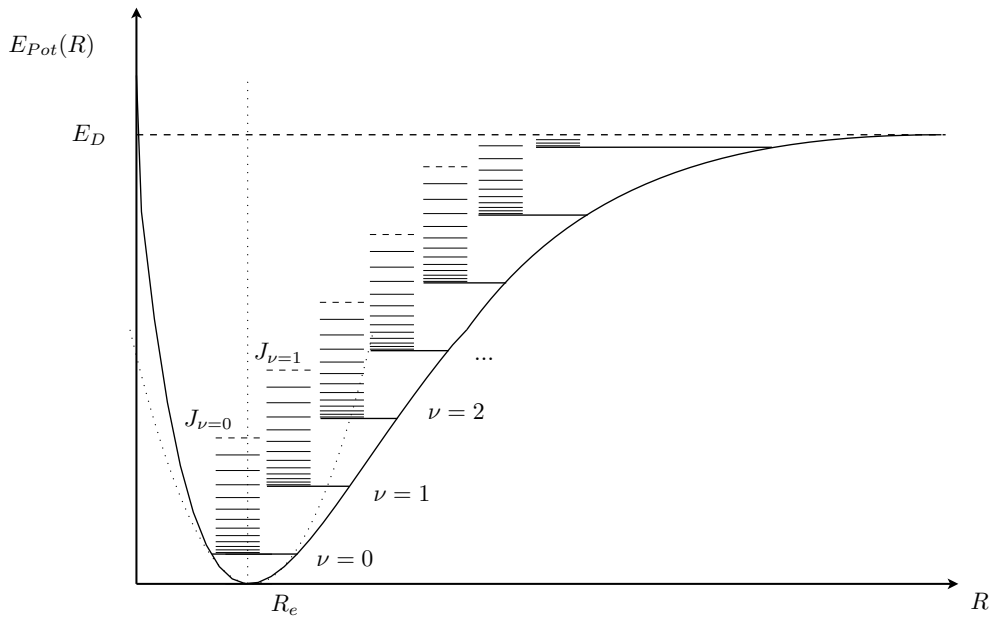

Figure 9: Potential Curve for a diatomic molecule (not to the scale, after Herzberg 1965)

4.2 Electronic motion

Compared to an atom, the number of symmetries in a diatomic molecule is reduced to one axial symmetry about the internuclear axis. Hence, the electric field in which the electrons move is no longer spherical symmetric. The total angular momentum $\vec{L}$ of the electronic system undergoes an increasing precession as the strength of the electric field rises and $\vec{L}$ looses the meaning as an angular momentum. However, the projection $\vec{\Lambda}$ of $\vec{L}$ on the axis is a constant of motion and therefore quantized (Fig. 10). For a fixed $L \equiv \left|\vec{L}\right|$, $\Lambda \equiv \left|\vec{\Lambda}\right|$ can take the values

$$\Lambda = -L, -L+1, \ldots, 0, \ldots, L-1, L \; . \tag{71}$$

Since there is a double orbital degeneracy that corresponds to the circulation of the electrons in a clockwise or counterclockwise direction, we will assume $\Lambda \geq 0$. The states with $\Lambda = 0, 1, 2, 3, \ldots$ are then denoted by

$$\Lambda = \Sigma, \Pi, \Delta, \Phi, \ldots \; , \tag{72}$$

similar to the notation in atoms ("s, p, d, f, ...").

Spins of the electrons are treated analogously: For $\Pi, \Delta, \Phi, \ldots$ - states, the orbital motion of the electrons causes an internal magnetic field, resulting in a precession of total spin $\vec{S}$. As for the angular momentum, we use the projection $\vec{\Sigma}$ of $\vec{S}$ on the intermolecular axis instead of $\vec{S}$. For Σ-states[9], $\vec{S}$ is fixed in the space, since an electric field does not affect the spin. For a spin quantum number $S \equiv \left|\vec{S}\right|$, $2S+1$ values for $\Sigma = \left|\vec{\Sigma}\right|$ are allowed:

$$\Sigma = S, S-1, \ldots, -S \; . \tag{73}$$

The total electronic angular momentum $\vec{\Omega}$ is the sum of the orbital angular momentum and the spin, but care has to be taken if the molecule rotates (c.f. Sect. 4.3):

$$\vec{\Omega} = \vec{\Lambda} + \vec{\Sigma} \tag{74}$$

$$\Omega = |\Lambda + \Sigma| \tag{75}$$

If Λ is not equal to zero, there are $2S+1$ different possible values of Ω for a given Λ resulting in molecular states with different energies. This effect is called multiplet splitting and may be observed e.g. in the ground state of the later discussed sulfur hydrid (SH). For Σ-states, no splitting occurs.

The notation for an electronic state is simillar to that for atoms, with

$$^{2S+1}\Lambda_{\Omega} \; . \tag{76}$$

For Σ-states, the eigenvalue (+/-) of the reflection operator applied in a plane containing the internuclear axis is attached as superscript to Eq. (76). Additionally, for homonuclear diatomic molecules (i.e. molecules with two similar atoms) a subscript g (gerade) and u (ungerade) indicates whether the wave function is either even (g) or odd (u) with respect to the inversion operation.

The complete denotation of a molecules state includes the electronic state, which are labeled with letters on the left to Eq. (76): X is reserved for the ground state, while A,B,C,... are used for excited states of the same multiplicity $(2S+1)$ as the ground state. Excited states with different multiplicity are denoted by a,b,c and so on. As an example, the ground state of the O_2 molecule (an even state with $\Lambda = 1$ and $S = 1$) is written as $X\,^3\Sigma_g^-$.

[9]The quantum number Σ must not be confused with the symbol Σ for $\Lambda = 0$-states.

4.3 Angular momentum and coupling cases

Since the actual rotation of the molecule and the electronic motion take place simultaneously and influence each other, it is necessary to couple their angular momenta. We will do that in limiting-case models, the Hund's coupling cases, first suggested by Hund (1927). Real molecules do not precisely correspond to one of these cases but to intermediate cases. However, generally the structure of the molecule agrees with one of the schemes more strongly than any other coupling case and can approximately be expressed by this scheme.

The coupling cases are of further importance, because they govern the selection rules for transitions between two rotational levels. For this section, we refer to Berdyugina (2002a). We will only discuss the two most frequent coupling cases, Hund's case (a) and (b); a complete discussion can be found in Herzberg (1965).

Hund's case (a)

The electronic angular momentum $\vec{L}$ and the spin $\vec{S}$ are strongly coupled to the line joining the nuclei and interact very weakly with the rotation of the molecule. The field, produced by the orbital momentum, is sufficiently strong to couple the spin $\vec{S}$ to the axis. Only the projection of $\vec{L}$ and $\vec{S}$ on the axis are well defined quantities, given by the quantum numbers Λ and Σ. Fig. 10 gives a vector diagram for this case. This scheme often applies for heavier diatomic molecules.

The total electronic angular momentum $\vec{\Omega} = \vec{\Lambda} + \vec{\Sigma}$ and the angular momentum of the rotation $\vec{N}$ form the resulting total angular momentum $\vec{J}$:

$$\vec{J} = \vec{\Omega} + \vec{N} \tag{77}$$

Possible quantum numbers for this operator are therefore:

$$J = \Omega, \Omega + 1, \Omega + 2, \ldots \tag{78}$$

Selection Rules

Electric dipol transitions between different states are only possible, when the quantum numbers of the upper and lower state (denotet by $(')$ resp. $('')$) satisfy the selection rules:

$$\begin{aligned}
\Delta J &= J' - J'' = 0, \pm 1 \quad \text{with restriction} \quad J' = 0 \nrightarrow J'' = 0 \\
\Delta\Lambda &= \Lambda' - \Lambda'' = 0, \pm 1 \\
\Delta\Sigma &= \Sigma' - \Sigma'' = 0 \\
\Delta\Omega &= \Omega' - \Omega'' = 0, \pm 1
\end{aligned}$$

Besides these selection rules, a change of parity (g $\leftrightarrow$ u) is needed for transitions of homonuclear molecules. Transitions between Σ-states are only allowed, if the eigenvalue of the reflection operator does not change (i.e. $\Sigma^+ \rightarrow \Sigma^+$ or $\Sigma^- \rightarrow \Sigma^-$, but not $\Sigma^+ \leftrightarrow \Sigma^-$).

Hund's case (b)

In Hund's coupling case (b), only the orbital angular momentum $\vec{L}$ is coupled to the internuclear axis. The spin $\vec{S}$ is weakly or not coupled to the internuclear axis. If $\Lambda = 0$ and $S \neq 0$, the spin $\vec{S}$ is not coupled to the axis at all and, thus, $\vec{\Sigma}$ and $\vec{\Omega}$ are not defined. The situation of Hund's case (b) is illustrated in Fig. 11.

The electronic angular momentum $\vec{\Lambda}$ and the angular momentum of the nuclear rotation $\vec{N}$ form the angular momentum

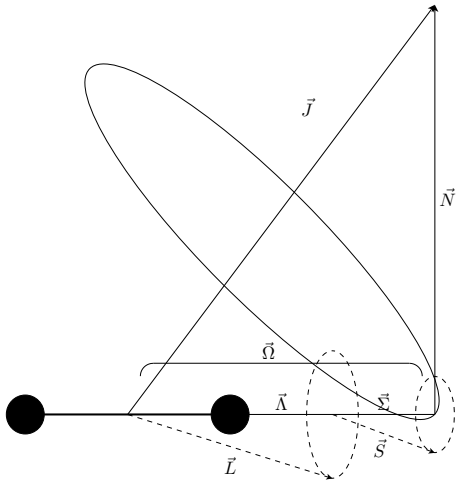

Figure 10: Vector diagram for Hund's case (a): The nutation of the figure axis is indicated by the solid-line ellipse; the much faster precession of $\vec{L}$ and $\vec{S}$ about the line joining the nuclei are indicated by the broken-line ellipses, (After Herzberg 1965).

$$\vec{K} = \vec{\Lambda} + \vec{N} \quad , \tag{79}$$

with quantum numbers

$$K = \left|\vec{K}\right| = \Lambda, \Lambda + 1, \Lambda + 2, \ldots \quad . \tag{80}$$

The total angular momentum $\vec{J}$ is then give by

$$\vec{J} = \vec{K} + \vec{S} \, , \tag{81}$$

and the corresponding quantum number can take the values

$$J = K + S, K + S - 1, \ldots, |K - S| \quad . \tag{82}$$

Selection Rules

For Hund's case (b), the following selection rules apply (The upper and lower level are denotet by ($'$) resp. ($''$)):

$$\begin{aligned}
\Delta J &= J' - J'' = 0, \pm 1 \;\text{ with restriction }\; J' = 0 \nrightarrow J'' = 0 \\
\Delta \Lambda &= \Lambda' - \Lambda'' = 0, \pm 1 \\
\Delta S &= S' - S'' = 0 \\
\Delta N &= N' - N'' = 0, \pm 1 \;\text{ with restriction }\; \Delta N = 0 \;\text{ for }\; \Lambda' = 0 \rightarrow \Lambda'' = 0
\end{aligned}$$

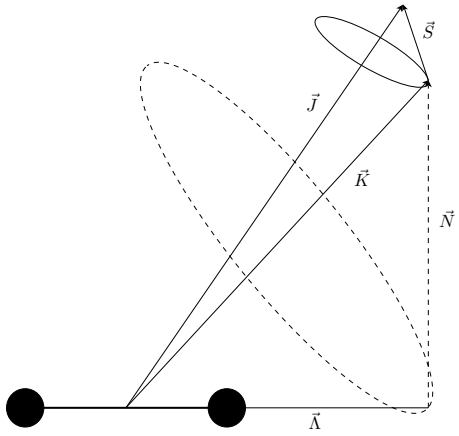

Figure 11: Vector diagram for Hund's case (b): The nutation of the figure axis is much faster than the precession of $\vec{K}$ and $\vec{S}$ about $\vec{J}$. For $\Lambda = 0$, $\vec{N}$ $(= \vec{K})$ is perpendicular to the internuclear axis, (After Herzberg 1965).

4.4 Spectroscopic Constants

The energy levels of a molecule can be expressed by a set of spectroscopic constants and an adequate Hamiltonian operator. In this chapter, a short overview of the calculation of pure rotational energy states is given. We will discuss terms that are needed for an accuracy of a fraction of a megahertz in the corresponding transitions. Vibrational and electronic motion is considered by a constant value, which can be left out, if only transition frequencies between two states are required.

An actual calculation of energy levels and line strengths including all below discussed contributions can be done by the `SPCAT` - Code (Pickett 1991).

The Rigid Rotator

The simplest model of a rotating diatomic molecule is the so-called dumbbell model or rigid rotator: The two atoms are considered to be mass points of mass m_1 (resp. m_2) and fixed at a distance $r = r_1 + r_2$ by a rigid bar (Fig. 12). We neglect in this first approach the finite size of the atoms and the extension of the intermolecular distance due to the rotation of the molecule.

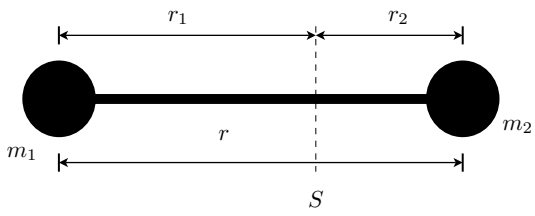

Figure 12: Dumbbell model of a diatomic molecule. The molecule rotates around the center of gravity, denoted by S, (After Herzberg 1965).

For the energy levels, we obtain (Herzberg 1965)

$$E_{rot} = \frac{\hbar^2 J(J+1)}{4\pi\mu r^2} = \frac{\hbar^2 J(J+1)}{4\pi I} \ , \tag{83}$$

with the rotational quantum number $J = 0, 1, 2, \ldots$ and the moment of inertia I, which can be expressed by the reduced mass $\mu = \frac{m_1 m_2}{m_1 + m_2}$ as $I = \mu r^2$. We find a set of discret energy levels with

energies increasing about quadratically, in contrast to the equidistant energy levels of vibrational states.

In molecular spectroscopy, the rotational term $F(J)$ [cm$^-$1] is usually given by the rotational constant $B = \frac{\hbar}{4\pi cI}$ [cm^{-1}]:

$$F(J) \equiv \frac{E_{rot}}{hc} = \frac{\hbar}{4\pi cI} J(J+1) = BJ(J+1) \tag{84}$$

The Nonrigid Rotator

In a real molecule, the internuclear distance is not fixed to a constant value. The distance adjusts so that the centrifugal force is compensated by a backdriving force due to the potential E_{Pot} (Fig. 9). For an increasing rotation (i.e. higher J), the internuclear distance and consequently the moment of inertia are increased and therefore the energy state is lower than the value of the rigid rotator (Eq. 84). Near the equilibrium, the potential E_{Pot} can be approximated by a parabola (dotted line in Fig. 9). This leads to a model of the molecule with two point-like atoms, connected by a massless linear spring (Demtröder 2005).

Up to terms of second order, the rotational term [cm^{-1}] for this system is

$$F(J) = \frac{E_{rot}}{hc} = BJ(J+1) - DJ^2(J+1)^2 \ , \tag{85}$$

with the rotational constants $B = \frac{\hbar}{4\pi cI}$ [cm^{-1}] and $D = \frac{4B^3}{\omega^2}$ [cm^{-1}]. The centrifugal distortion constant D is much smaller than the rotational constant B. For highest accuracy, even terms of third order (denotet by H) and effects due to the non parabolic potential have to be taken into account.

Fine Structure

The interactions of the the electron spin with the magnetic fields created by the motion of the electrons, nuclei and other electron spins are called fine structure. They can alter the level energies by several 100 MHz and occur only in nonsinglet states (i.e. $S \neq 0$). The spin-spin interaction is represented by the molecular constant λ and the spin-orbit coupling by the constant γ. For a triplet state (e.g. $^3\Sigma$), the difference between the highest and lowest energy state is $2\lambda + \gamma$. A derivation of the complete equation for the fine structure energy states, the so-called Schlapp-expression can be found in Hougen (1970).

Hyperfine Structure

A much smaller additional term takes the effects of the nuclear magnetic and electric moments into account and is called hyperfine structure. The nuclear magnetic moment can interact with other magnetic moments in a molecule, with electron spins and their orbital motion and with other nuclear spins. Since the nuclear spin $\vec{I}$ is another angular momentum beside $\vec{L}$ and $\vec{S}$, the above mentioned coupling cases have to be extended. The corresponding spectroscopic constants are labeled by b_f and c, their definition and application is given in Frosch & Foley (1952).

5 Calculations

5.1 Introduction

In less than two years, the Herschel Space Observatory (Fig. 13) will give a unique possiblity to observe far infrared and submillimeter wavelengths between 60 μm and 670 μm (450 GHz - 5 THz). Due to the absorption by atmospheric gases, ground based telescopes cannot observe in this frequency range. The satellite will carry a 3.5 meter diameter mirror and three scientific instruments, two cameras or medium resolution spectrometers (PACS and SPIRE) and a high resolution heterodyne spectrometer (HIFI). Herschel will be placed in the second Lagrangian point of the Sun-Earth system, situated 1.5 million kilometers away from the Earth in the anti-sunward direction. This offers a stable thermal environment and cools down the telescope to about 80 K. The much larger mirror of the satellite compared to previous space infrared telescopes (IRAS, ISO or the Spitzer Space Telescope) is only passively cooled but the scientific instruments are situated in a superfluid helium cryostat (Pilbratt 2001).

The scientific purpose of Herschel is the "cold" universe: Black-bodies with temperatures between 5 K and 50 K and gases with temperatures from 10 K up to a few hundered Kelvin emit in wavelengths that are observable by the satellite. Such conditions can be found everywere in the universe, from the solar system to the most distant early epoch protogalaxies! However, the key science objectives are the formation of stars and galaxies and the interrelation between the two as well as the formation of planetary system bodies.

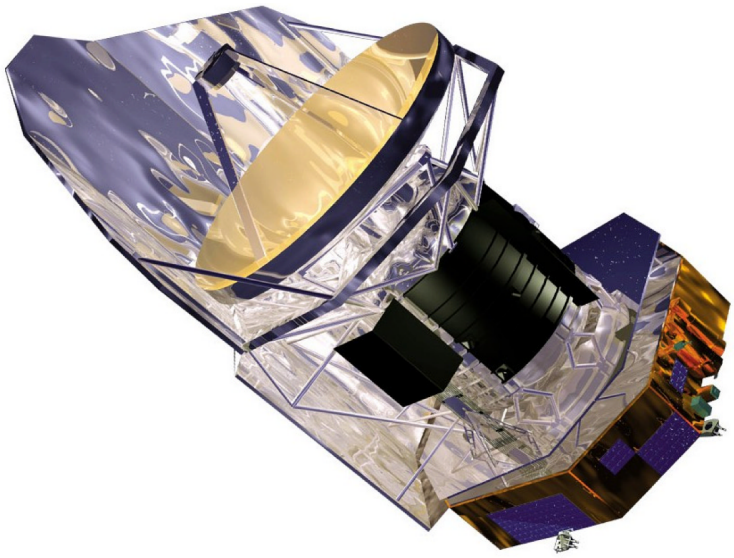

Figure 13: The Herschel satellite (Pilbratt 2001)

The HIFI (Heterodyne Instrument for the Far-Infrared) instrument, partly built by the Institute for Astronomy (IfA) and the Microwave Electronics Laboratory (IfH) at the Swiss Federal Institute of Technology ETH in Zurich, on board the satellite will conduct very high resolution spectroscopic observations. A velocity resolution of 0.3 - 300 km s^{-1} ($\Delta v = \frac{\Delta\lambda}{\lambda} \cdot c$) is achieved in a frequency range of 480 GHz to 1250 GHz and 1410 GHz to 1910 GHz (625-240 μm and 213-157 μm, resp.). The sensitivity of only a factor 3 above the quantum noise limit provides the possibility to observe even the weakest lines of extra-galactic objects. HIFI has a large instantaneous bandwidth of 4 GHz for fast spectral surveys. The science objective of the experiment is the understandig of the cyclic interrelation between stars and the interstellar medium. With HIFI it will be possible to observe water vapor (and water tracers) and the important coolant [CII] as well as not yet discovered molecules with lines in the newly available frequency range (de Graauw & Helmich 2001).

In return to the Swiss contribution to HIFI, the Institute for Astronomy has observation time at disposal in the first third ("guaranteed time") of Herschels 3 years operational lifetime. One part of the project is the observation of hydrides and their ions, e.g. CH or CH^+, in envelopes of star forming regions. It is therefore necessary to calculate estimations of the expected line strengths in order to divide the valuable observation time.

In this chapter, we will discuss the calculation of the line strength of CH, CH^+, SH, SH^+, NH and OH^+ for three different objects that will possibly be targets for Herschel. First, we give an overview of the used chemical models and then describe the providing of the molecular data. The selection of the strongest lines and the actual calculation of the line strengths are presented hereafter.

5.2 Physical and Chemical Models

In order to solve the radiative transport equations, a complete physical and chemical model of the emitting area is required: The model should predict the molecular abundances of the considered molecules and the most abundant molecule H_2 as well as the temperatures of the gas and the dust. For our calculations, we have used the model based on Doty et al. (2002) and extended by Stäuber et al. (2004a) and Stäuber et al. (2004b) with a central UV resp. X-ray source. We will only give a brief outline of the simulation. More detailed informations can be found in the papers mentioned above.

The model concentrates on the extended envelope of a Young Stellar Object, since the inner part with the central source is still unresolved by observations. It is assumed that the geometry is spherical symmetric and the simulation starts with initial abundances for several species, in the gas phase as well as on dust grains. The density profile of H_2 and the temperature is assumed to be constant with time during the simulation and no flow of material is taken into account. Therefore, dynamical aspects of the evolution like the gravitational collapse and shocks that can lead to higher temperatures and specific chemical reactions are not included in the model. Geometrical effects as the further penetration of UV radiation or X-rays along the axis of an outflow that might change abundances of X-ray enhanced species in the observable part of the envelope are also neglected. After a set of initial abundances and physical conditions is assumed, the time-dependent chemical evolution after Eq. (16) is calculated.

The density distribution of H_2, the most abundant molecule, is determined by observations of the continuum flux and CS lines and fits to a power law

$$n = n_0 \left(\frac{r_0}{r}\right)^{\alpha} \quad , \tag{86}$$

with indivdual values for the index α depending on the source. The gas heating is dominated by gas-grain collision, and the dust temperature profile can be obtained from a self-consistent solution of the continuum radiative transport problem. For our calculations, it was assumed that the dust and gas temperature T_{gas} resp. T_{dust} are similar ($T_{gas} - T_{dust} \lesssim 10$ K). This is a good approximation as long as the X-ray luminosity is not to high.

The chemical model is based on the UMIST database for astrochemistry[10] and involves about 400 species and 4000 reactions between them. The accuracy of the rate coefficents is often only by a factor of 2, since their measurement is hard to perform in terrestrial conditions. Radiation from the central source have been included in the chemical network as described in Sect. 2.3. Aditional parameters for the chemical network are the cosmic ray ionization rate and the flux strenghts of the UV field and X-rays. Finally, the chemical evolution is calculated at 30 radial grid points.

[10] http://www.udfa.net/

5.2.1 AFGL 2591

The high mass object AFGL 2591 has the observational advantage that it is situated in relative isolation, while most massive stars form in clusters. This allows us to study its physical, thermal and chemical structure without influence of a nearby massive source. AFGL 2591 is well-observed in the continuum and in different molecular lines. It has a mass of about 42 $M_\odot$ within a radius of $3 \cdot 10^4$ AU and its luminosity is about $2 \cdot 10^4$ $L_\odot$. For our calculations, we have assumed a distance to AFGL 2591 of 1 kpc, however this value is not well established. A set of initial abundances is taken as in Stäuber et al. (2004b) and the model covers a region from $r_{in} \sim 200$ AU to $r_{out} \sim 29000$ AU. The cosmic ray ionization rate was taken to be $\zeta_{cr} = 5.6 \cdot 10^{-17}$ s^{-1} and the parameters of the density distribution power-law are $n_0 = 5.8 \cdot 10^4$ cm^{-3}, $r_0 = 2.7 \cdot 10^4$ AU and an index of $\alpha = 1$, in agreement with Stäuber et al. (2004b) and Doty et al. (2002). The chemical age (the final time-step of the calculation) was $5 \cdot 10^4$ years. Five models where calculated with different values for the X-ray luminosity (L_X), the temperatures T_X of the X-ray emitting plasma and the inner UV flux ($G_{0,in}$). The inner H_2 column density[11] $N_{H,in}$ between the source and the first grid point is assumed to be constant for the models with radiation and vanishing for model 0. Tab. 2 gives an overview of the used parameters. The numbering of the models corresponds to Stäuber et al. (2004b) and Model 0 excludes any radiation, as presented in Doty et al. (2002).

Model	L_X [ergs s^{-1}]	T_X [K]	$N_{H,in}$ [cm^{-2}]	$G_{0,in}$
0	0	0	0	0
1	0	0	$3 \cdot 10^{22}$	10
2	$1 \cdot 10^{30}$	$7 \cdot 10^7$	$3 \cdot 10^{22}$	0
3	$1 \cdot 10^{31}$	$7 \cdot 10^7$	$3 \cdot 10^{22}$	0
6	$8 \cdot 10^{31}$	$1 \cdot 10^8$	$3 \cdot 10^{22}$	10

Table 2: Model parameters for AFGL 2591

The resulting fractional chemical abundances of the later used hydrides is presented in Fig. 14. The plots show that several of the considered species are strongly enhanced by X-rays (Stäuber et al. 2004b): In the chemical network, the larger abundance of SH and SH^+ compared to the model without X-rays can be explained by the photodissociation of H_2S. Atomic sulfur then reacts with OH and either forms SO or SH. The large abundance of SH^+ is due to efficient reactions of the atomic sulfur with H_3^+ or HCO^+, which are both strongly enhanced by X-rays. The OH^+ ion is mainly built in reactions of the radiation enhanced He^+ with H_2O or in reactions of H_3^+ with OH and destroyed by reactions with H_2. The photodissociation of CH_4 by X-rays and reactions of atomic carbon with H_2 produces CH_2, that undergoes the reaction $CH_2 + H \rightarrow CH + H_2$ producing CH. Ionized carbon hydride CH^+ is efficiently built by the reaction of C with H_3^+ or HCO^+.

5.2.2 IRAS 16293-2422

The deeply embedded Class 0 source IRAS 16293-2422 in the Ophiuchus constellation is a well studied low-mass Young Stellar Object (van Dishoeck & Blake 1998). Like many other low-mass objects, it is a binary system, with estimated masses of about 0.5 $M_\odot$ per star at a separation of 840 AU. The used model parameters follow Stäuber et al. (2005b): The distance to IRAS 16293-2422 is taken to be 160 pc and a luminosity of 27 $L_\odot$ is assumed. The envelopes total mass is about 5.4 $M_\odot$. Again, a power-law density structure is used, here with an index α of 1.7 and a density of $6.7 \cdot 10^6$ cm^{-3} at 1000 AU radially from the source. The range of $r_{in} \sim 32$ AU to $r_{out} \sim 8000$ AU is covered by the simulation. Initial abundances are taken from Doty et al. (2004) and are similar to those for the high mass object AFGL 2591. Although not yet observed towards Class

[11] Notice, that $N(H) = 2 \cdot N(H_2) + N(HI)$

0 objects, the source is assumed to emit X-rays. The X-ray plasma temperature is assumed to be $T_X = 3 \cdot 10^7$ K and the fluxes are taken to be 10^{28}, 10^{30} and 10^{32} ergs s^{-1}. An additional model without X-rays is calculated. Since the correct chemical age is still controversial, the chemical evolution was calculated up to 10^4 years and 10^5 years, respectively, as suggested in Stäuber et al. (2005b) and Doty et al. (2004). Recent observations with the Spitzer Space Telescope indicate that IRAS 16293-2422 may have a large cavity in the envelope with a diameter of 400 to 800 AU. The size of the cavity is comparable to the centrifugal radius of the envelope and therefore appears to be a consequence of the rotation of the protostellar core. This rotation may also have caused the fragmentation leading to the central protostellar binary (Jørgensen et al. 2005). A third model takes such a "protostellar hole" into account, whereas the chemical age is assumed to be 10^5 years. The chemical age 10^4 years and a "protostellar hole" is combined in a further model. Figures 15 - 18 show the results for the calculations.

5.2.3 TMC 1

TMC 1 (IRAS 04381+2540) is a Class I Young Stellar Object in the Taurus molecular cloud (TMC) at a distance of 140 pc and a luminosity of 0.66 $L_\odot$. The envelopes mass is much lower than for IRAS 16293-2422 and estimated to be 0.034 $M_\odot$. The same assumptions for the initial abundances and the X-ray radiation as for IRAS 16293-2422 have been applied. The power-law distribution of the density is assumed to have an index α of 1.6 and the H_2 density at a distance of 1000 AU from the source is $8.8 \cdot 10^4$ cm^{-3}. The simulation covers a range of 3.1 AU up to 4300 AU and the chemical age was assumed to be 10^5 years. Further details of the model can be obtained again from Stäuber et al. (2005b). The results of the calculations can be found in Fig. 19.

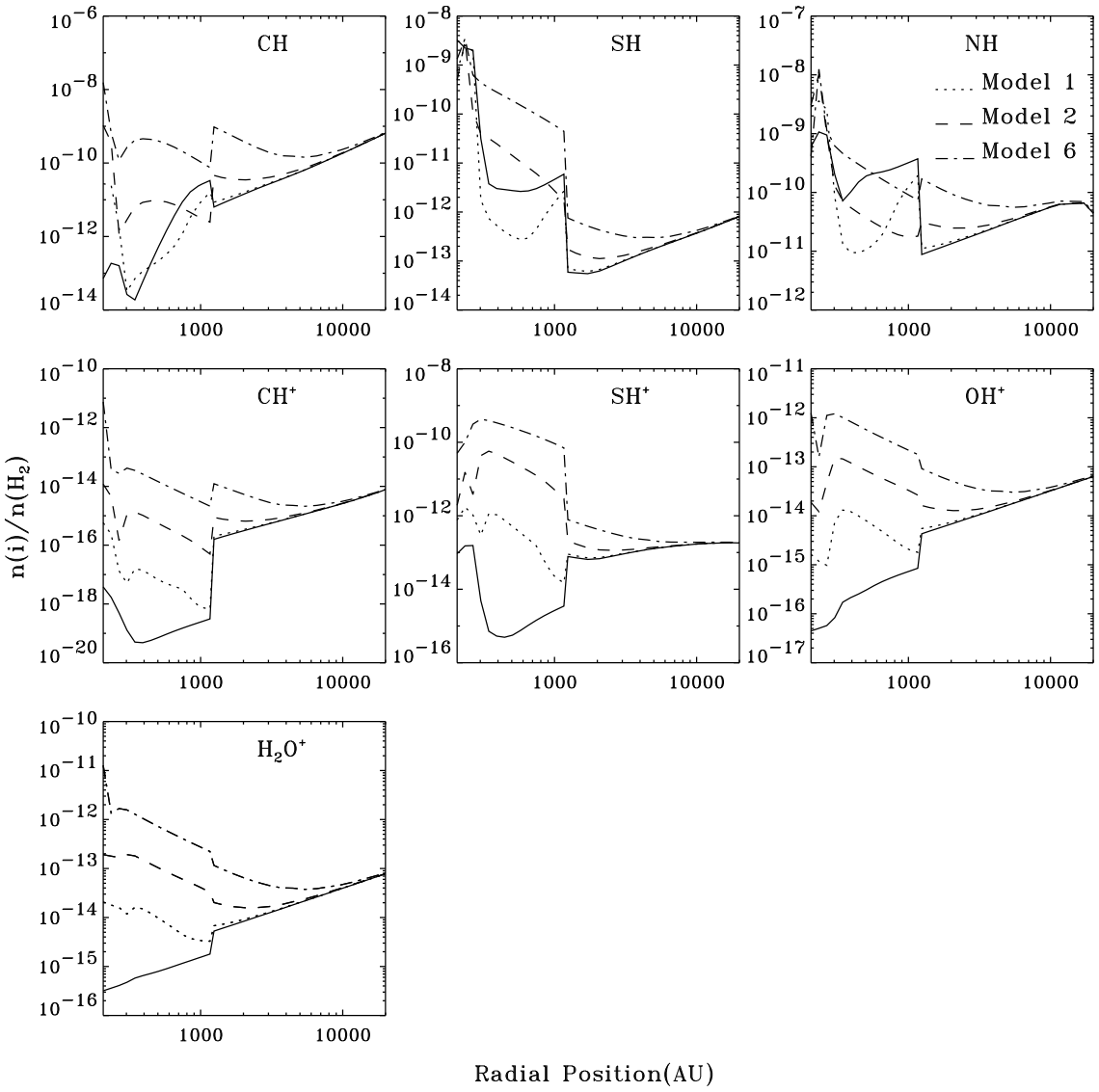

Figure 14: Depth dependent fractional abundances of AFGL 2591 for the later used hydrides and the water ion. The solid line corresponds to model 0 without a central radiation field. model 3 is not ploted, since it is very similar to model 6.

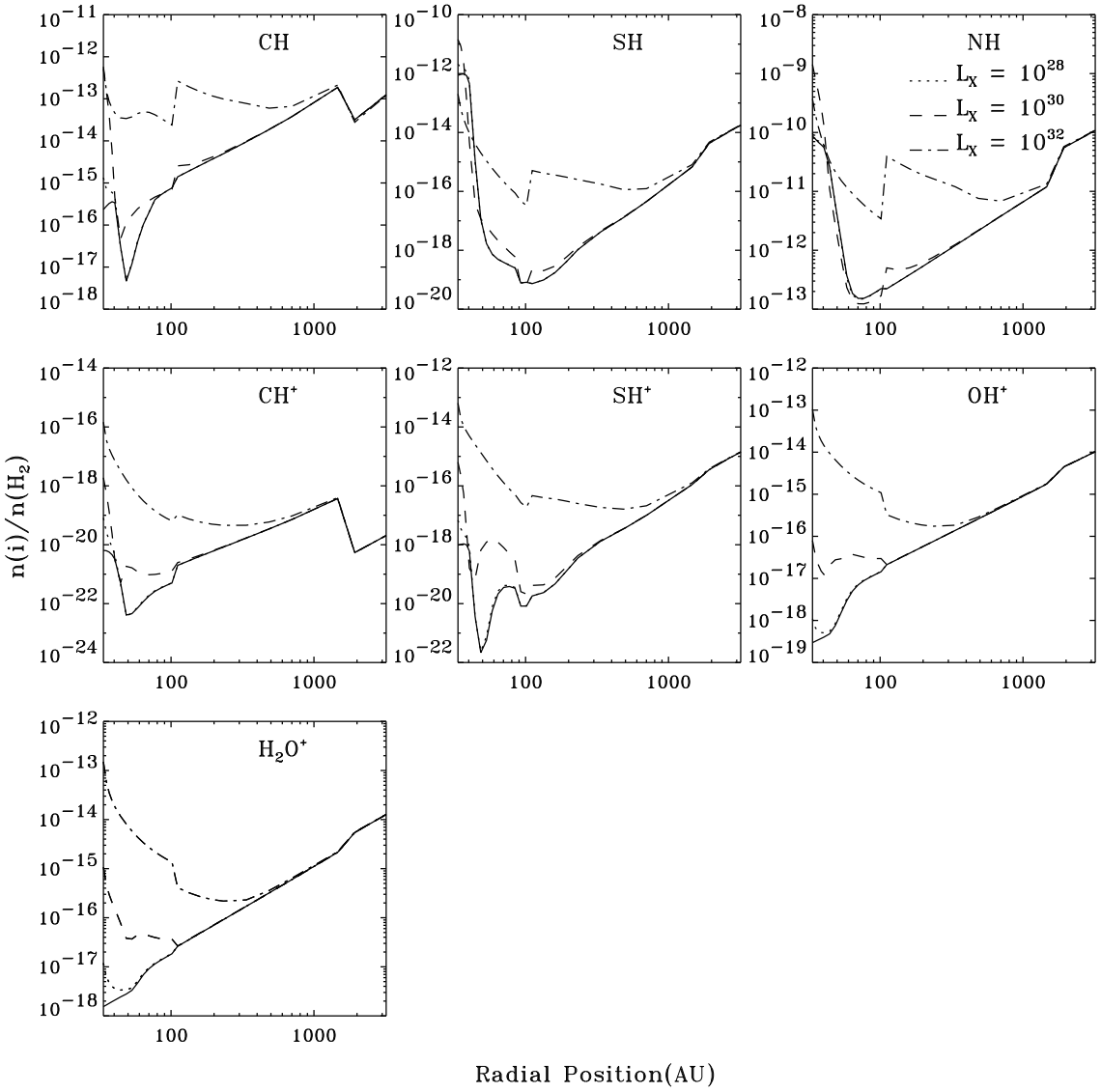

Figure 15: Depth dependent fractional abundances of IRAS 16293-2422 for the later used hydrides and the water ion. A chemical age of 10^5 years was assumed. The solid line corresponds to the Model without a central radiation field.

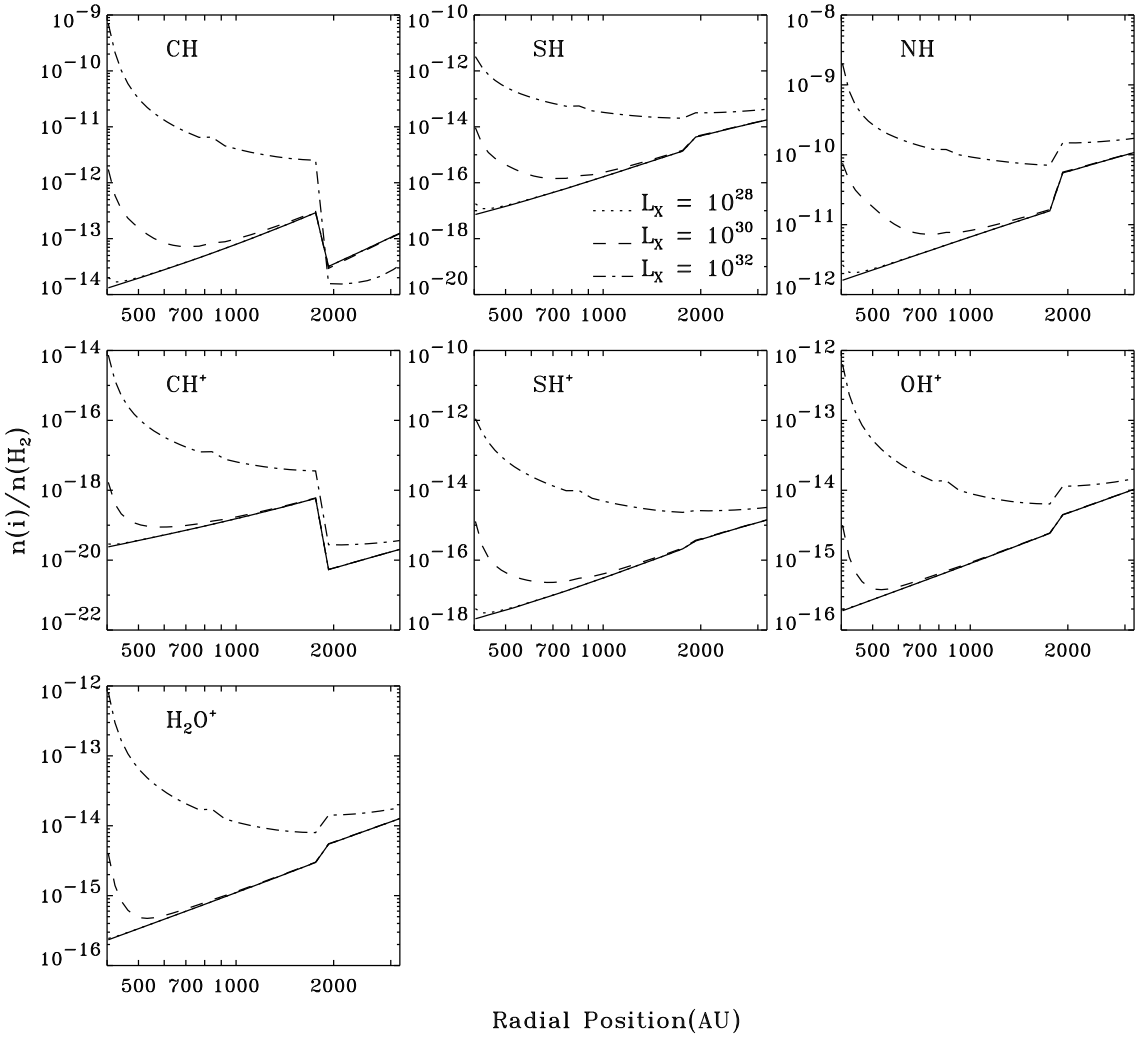

Figure 16: Depth dependent fractional abundances of IRAS 16293-2422 with a protostellar hole. A chemical age of 10^5 years was assumed. The solid line corresponds to the Model without a central radiation field.

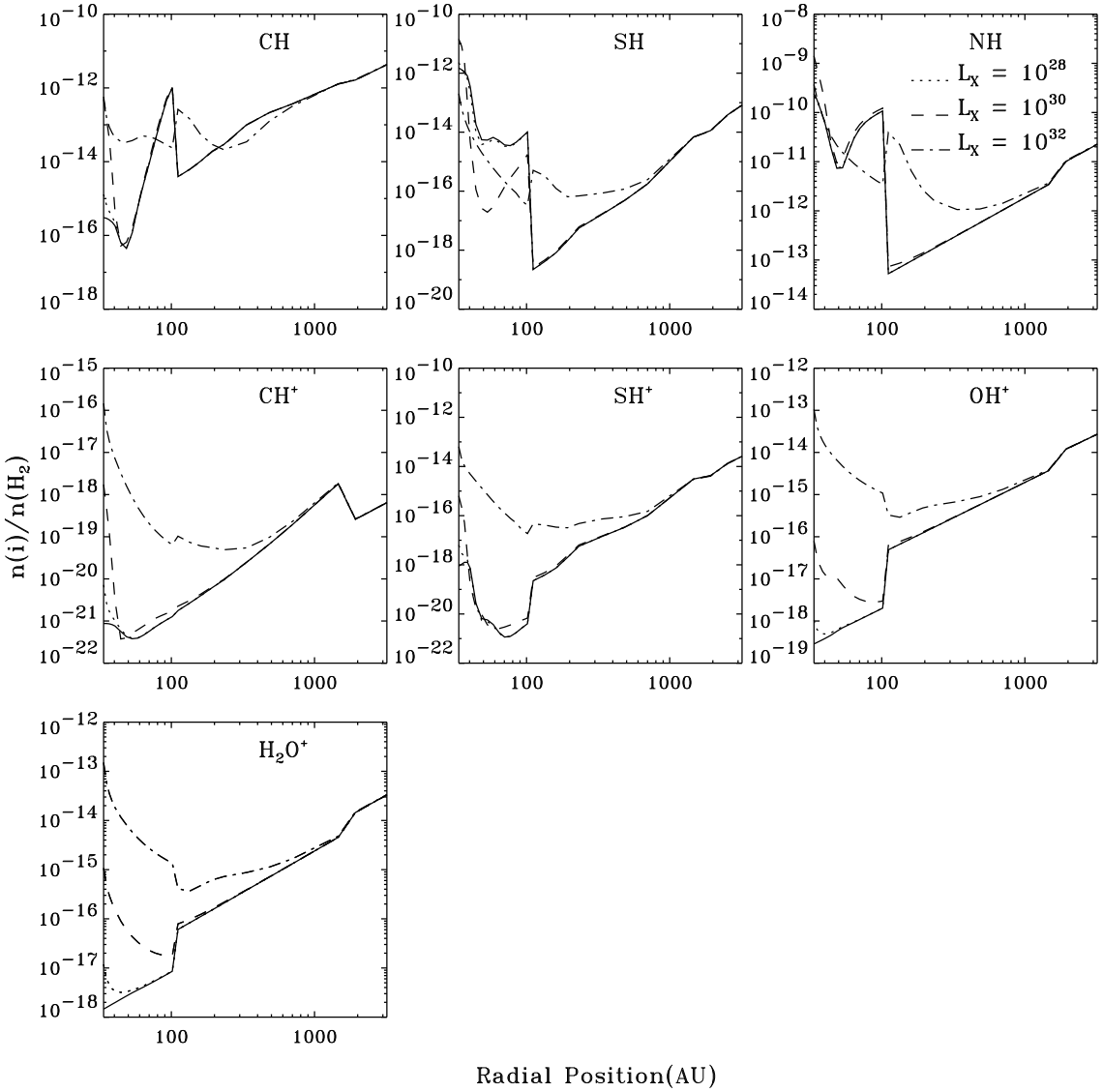

Figure 17: Depth dependent fractional abundances of IRAS 16293-2422. A chemical age of 10^4 years was assumed. The solid line corresponds to the Model without a central radiation field.

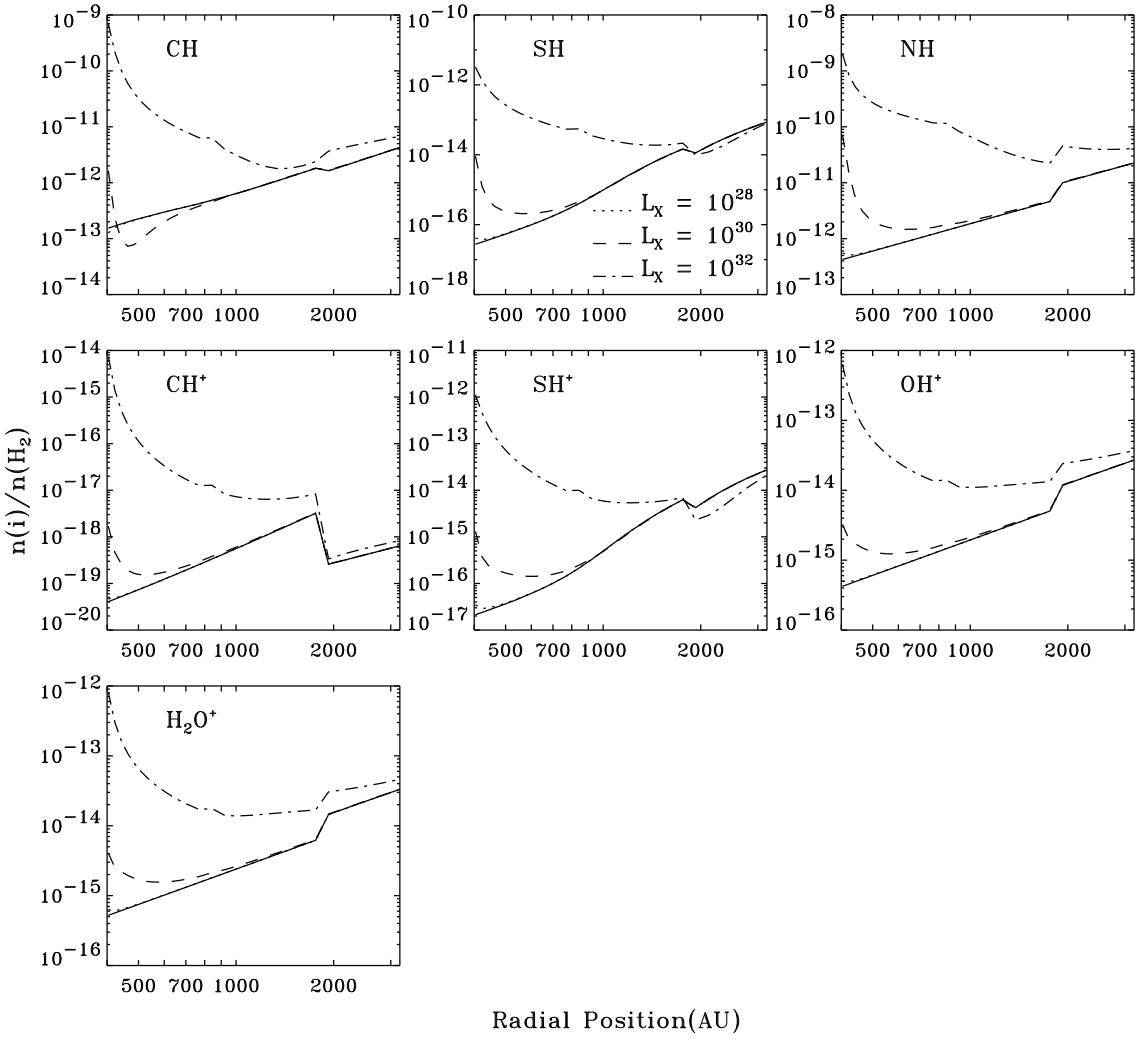

Figure 18: Depth dependent fractional abundances of IRAS 16293-2422 with a protostellar hole. A chemical age of 10^4 years was assumed. The solid line corresponds to the Model without a central radiation field.

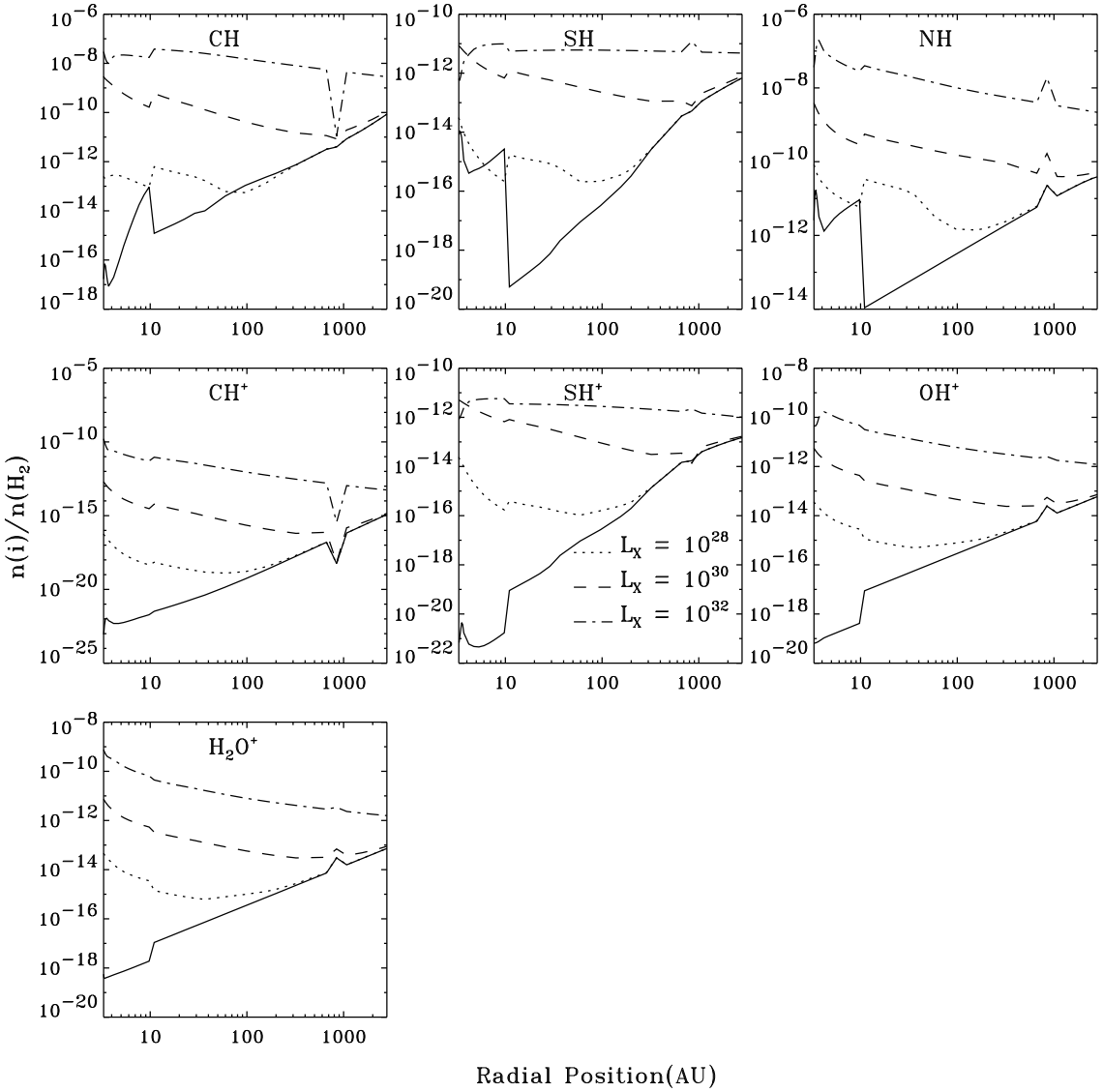

Figure 19: Depth dependent fractional abundances of TMC 1 for the later used hydrides and the water ion. The solid line corresponds to the Model without a central radiation field.

5.3 Molecular Data

The radiation of a molecular cloud can consist of several hundred molecular lines in the 4 GHz bandwidth of Herschel. Therefore, very accurate transition frequencies are needed for a prediction of the spectra. It is not yet possible to calculate the corresponding energy levels in the desired accuracy ab-initio and spectroscopic measurements of real molecules are thus still not avoidable (Bernath 2002). A fit of the recorded spectra to an adequate Hamiltonian delivers then the required spectroscopic constants from which a complete set of all transitions can be calculated (Sect. 4.4). For radio frequency, microwaves to far-infrared radiation, databases of molecular transitions and line strenghts exists, e.g. the Cologne Database for Molecular Spectroscopy CDMS[12] (Müller et al. 2001) or the Jet Propulsion Laboratory (JPL) Molecular Spectroscopy Database[13] (Pickett et al. 1998). The Leiden Atomic and Molecular Database[14] (LAMDA) (Schöier et al. 2005) also contains collision rate coefficients for temperatures up to about 2000 K. The `RATRAN`-Code uses the file format of this database. Unfortunately, none of the considered molecules (CH, CH^+, SH, SH^+, NH, NH^+, OH^+ and H_2O^+) can be found in LAMDA. We will therefore disucss in this section the providing of molecular data in the `RATRAN` file format from the JPL database, the CDMS or from spectroscopic constants.

5.3.1 CH, CH^+, NH, OH^+ and SH

Transition frequencies and line strengths of CH, CH^+, NH and SH are taken from the JPL database and data for OH^+ was obtained from the CDMS. Both databases have the same data format, since they use the `SPFIT` and `SPCAT` - code (Pickett 1991) to calculate spectroscopic constants from measured spectra and predict lines out of the obtained constants. An example of a molecular data file is given in Fig. 20: The first three columns contain the line frequency ν, the estimated error $\Delta\nu$ and the base 10 logarithm of the integrated intensity I at 300 K [nm^2 MHz]. In further columns, the energy of the lower level E_{low} [cm^{-1}] and the upper state degeneracy g' can be found. The last eight columns represent the quantum numbers of the upper and lower state (Q' and Q''). In addition to the "line file", a "documentation file" contains the partition function, information on the ground state, the electric dipol moment and references to the experimental data.

ν	$\Delta\nu$	$log_{10}(I)$	E_{low}		Q'	Q''
536762.6574	.6413	-1.5397 2	.0004	5	13002 224 1-1 2 2	1 1 1 1
536783.5439	.5848	-2.2387 2	.0004	3	13002 224 1-1 2 1	1 1 1 1
536797.2871	.5860	-1.9376 2	0.0000	3	13002 224 1-1 2 1	1 1 1 0
1470682.7713	.6706	-2.1260 2	17.8815	3	13002 224 2-1 2 1	1 1 2 2
1470684.9746	.5532	-1.4271 2	17.8814	3	13002 224 2-1 2 1	1 1 2 1

Figure 20: Example data from the JPL Molecular Spectroscopy Database (http://spec.jpl.nasa.gov and Pickett et al. 1998)

The Einstein-A-Coefficients were calculated by the equation (Pickett et al. 1998)

$$A_{ul} = 2.7964 \cdot 10^{-16} \cdot I_{ul}(T)\, \nu_{ul}^2\, \frac{Q(T)}{g'} \frac{1}{e^{-E''/kT} - e^{-E'/kT}} \ , \tag{87}$$

with I_{ul}, the integrated line intensity [nm^2 MHz] at the reference temperature T [K], $Q(T)$ the partition function evaluated at the same temperature, g' the upper state degenarcy, E' resp. E'' [J] the upper and lower state energies and ν_{ul} the line frequency [MHz]. The reference temperature T is for both JPL database and CDMS 300 K.

[12] http://www.cdms.de
[13] http://spec.jpl.nasa.gov
[14] http://www.strw.leidenuniv.nl/~moldata/

Unfortunately, the databases give the energy levels $E_0, E_1, E_2, \ldots$ only with an accuracy of 10^{-4} cm^{-1} (fifth row in Fig. 20). The molecular data file for the `RATRAN` radiative transport code, however, needs higher accuracy. Calculations with the values of the databases would lead to transition frequencies with an error of about ± 3 MHz. Therefore only the ground state energy was taken directly from the table and further levels where calculated successively by using the transition frequency ν_{ul} and the relation between the upper and lower energy level (E' and E'', resp.)

$$E'' + h\nu = E' \ . \tag{88}$$

Transition frequencies corresponding to the so calculated energies are withhin 0.01 MHz from the frequencies, tabulated in the databases.

The processing of JPL or CDMS data to `RATRAN` molecular data files can be summarised by the following steps, that have been carried out by an IDL - script:

1. The transitions are read from the database.
2. The ground state has to be defined and as the database gives only the degeneracy of the upper state of a transition, the ground state's degeneracy has to be calculated (usually with the last quantum number F by $2 \cdot F + 1$, c.f. Pickett et al. 1998, Sect. 5).
3. Since `RATRAN` needs numbered energy states $\{E_1, E_2, E_3, E_4, E_5, ...\}$, unique numbers are given to the quantum numbers (e.g. "`1-1 2 2`") in the database.
4. The energy levels are calculated as discussed before.
5. Because `RATRAN` needs energy levels in ascending order, the levels are sorted. Care has to be taken for the lines so that transitions still belong to the correct energies.
6. The Einstein-A-Coefficient is calculated with equation (87).
7. Several hyperfine structure transitions are not resolved by the database but listed by more than one entry. Such lines are combined and the coressponding Einstein-A-Coefficient is accumulated.
8. Since `RATRAN` can only handle up to about 500 transitions and 200 energy levels, transitions with frequency outside the HIFI-band are dropped and energy states that are no longer used thereafter removed[15].
9. The data is written out in the molecular data format of `RATRAN`.

This algorithm was applied on the molecules mentioned above :

CH

Carbon hydride or Methylidyne (CH) has a $X^2\Pi_{\frac{1}{2}}$ ground state and can be described by Hund's case (b) (Sect. 4.3). In the JPL database, to which we refer for the raw data, the quantum state is denoted by the quantum numbers K, Λ, J and F. The principal quantum numbers, those not designating the spin state, are $\Lambda = \{-1, +1\}$ and $K = \Lambda + N$, with the angular momentum of the nuclear rotation N. The total parity of the state is denoted by convention as the sign of Λ. With the total angular momentum J, the electronic spin is also given, since $J = K + S$. Hyperfine structure transitions are also resolved in the raw data and specified by the quantum number $F = I + J$ for the nuclear spin I

For example, the ground state ($X^2\Pi_{\frac{1}{2}}$, $F = 0$ and positive parity) has the following quantum numbers in the JPL database:

[15]Strictly speaking, this is only applicable for the LTE calculation, since a Monte Carlo or Escape Probability calculation should take all possibly populated states into account.

$$(K, \Lambda, J, F) = \left(1, +1, \frac{1}{2}, 0\right) \tag{89}$$

Rotational levels with non-vanishing electronic angular momentum ($\Lambda \neq 0$) are usually doubly degenerated, since the projection of $\vec{L}$ on the internuclear axis can take two different values: $+\Lambda$ and $-\Lambda$. If the interaction of the orbital momentum with the total rotation of the molecule is taken into account, the degeneracy is removed. If both states of a transition have $\Lambda \neq 0$, the lines appear as doublets arising due to transitions between the rotational sublevels of different symmetry (Berdyugina 2002a). This splitting is called Λ-type doubling and has been observed in CH. The parity is therefore important for a complete description of the molecules state. The 3.335 GHz ground state Λ-type doubling transition between negative and positive parity has been detected in the ISM by Rydbeck et al. (1976).

In the JPL database, 324 transitions are given and therefrom 20 are observable with HIFI. The accuracy of the frequencies is very good. The estimated error stays below 0.8 MHz in these lines. An exact value for the transition dipol moment is also given.

CH^+

The single ionized carbon hydride or Methylidynium (CH^+) has a $X^1\Sigma$ ground state. The data from the JPL database is based on observations of excited electronic states, since no pure rotational lines are available so far. The estimated error is therefore very high. In the database, no hyperfine-structure is resolved and the quantum number K gives therefore the internuclear rotation of the molecule. Out of totally 10 transitions, 2 with frequency 835.071 ± 0.03 GHz and 1669.160 ± 0.06 GHz are accessible to HIFI. The accuracy of ± 30 MHz and ± 60 MHz respectively, is far to low for an observation. Recently, Falgarone et al. (2005) mentioned a not yet published measurement by J.C. Pearson of $^{12}CH^+$(1-0) to 835.079 ± 0.001 GHz. The transition frequency in the database has been adapted to this value. Corrections of the Einstein-A-Coefficient have not been performed, since they would contribute only marginally.

No exact dipol transition moment of CH^+ is available yet and the JPL database uses therefore the arbitrary value 1 Debye for the calculation. The dipol transition element enters in the calculation of the Einstein-A-Coefficients quadratically and the values are therefore to be treated carefully.

Molecules in the interstellar medium were discovered about 60 years ago in optical wavelengths by the assignment of unknown lines to diatomic molecules. The first three species that have been detected in this way were CH, CH^+ and CN. Douglas et al. (1941) reported the discovery of CH^+ in the ISM. About 20 years later, CH^+ has also been observed in radio wavelengths.

NH

The JPL database provides 1416 transitions of the Imidogen (NH). It has a $X^3\Sigma^-$ ground state and the principal quantum numbers are K for the rotation and J for the total angular momentum. The nuclear spin of the hydrogen and the nitrogen atom are expressed by I_H and I_N respectively (Klaus et al. 1997). The used coupling scheme is

$$J = S + K \tag{90}$$
$$F_1 = I_H + J \tag{91}$$
$$F = I_N + F_1 \ . \tag{92}$$

51 lines are observable with HIFI and the accuracy of the frequency is very good with an estimated error below 0.5 MHz. The dipole momentum is also well known.

The NH radical is well studied in astronomy in absorption towards stars (including the sun) and in comets. According to Klaus et al. (1997), NH has also been detected in diffuse interstellar

clouds. Since the measured column density was 20-40 times larger than obtained by gas-phase chemical model calculations, the formation of NH on grain surfaces was suggested.

OH^+

Data for OH^+ (Oxoniumylidene) was obtained from the Cologne Database for Molecular Spectroscopy. Therein 209 transitions are tabulated, whereas 13 remained after the frequency cut for HIFI. The molecule's ground state is $X^3\Sigma^-$ and Hund's case (b) is the applicable coupling scheme. The states are described by the quantum numbers K (principal), J (total angular momentum, $J = S + K$) and F (nuclear spin, $F = I + J$). The estimated error of the transition frequencies is withhin 2 MHz but since most of the measured data was taken from vibrational states, the predictions of this lower states should be treated with some caution. The dipol moment is from ab initio calculations and therefore also afflicted with some uncertainty.

The OH^+ molecule is a very important key in the chemical network of oxygen and water. It was found in tails of comets and is believed to exist near Saturn's main ring, but the first detection of OH^+ in the interstellar medium is left to Herschel.

SH

The data for the calculation with sulfur hydrogen SH was obtained from the JPL database. 640 transitions are given and 27 fit the frequency range of HIFI. As CH, it has a Π-ground state with ($S = \frac{1}{2}$), but this time with $J = \frac{3}{2}$ and is thus labeld by $X^2\Pi_{\frac{3}{2}}$. This is an inverted state, that means the constant of the spin-orbit coupling is negative. Like CH, SH also shows Λ-type doubling effects (Klisch et al. 1996). The notation of the quantum numbers is similar to those of CH, but as often for heavier molecules, it must be described by Hund's case (a) (c.f. Sect. 4.3). The coupling scheme for Λ, Σ, N and J in this case is

$$J = \Lambda + \Sigma + N \ , \tag{93}$$

but since the JPL database gives an aggregated quantum number $N' = N + \Lambda$, the coupling scheme is simplified to $J = N' + S$ like in Hund's case (b). The quantum number F for the nuclear spin and ν for the vibrational state was introduced. The relation of F to quantum number of the total nuclear spin I is again $F = I + J$. In the JPL database, data for pure rotational transitions in higher excited vibrational states (ν =1 or 2) is available for a few species. Fifteen of the to Herschel accessible SH-lines are transitions between states with $\nu = 1$. The ground state $X^2\Pi_{\frac{1}{2},\nu=1}$ of the first excited vibrational state lies 2598.0256 cm^{-1} higher than the ground state $X^2\Pi_{\frac{3}{2},\nu=0}$. Since this energy corresponds to about 3740 K, levels with $\nu = 1$ are not likely to be excited in the environment of YSOs. The estimated error of $\nu = 0$ transition frequency is about 0.1 MHz and 2 MHz for $\nu = 1$ states.

A detection of SH in the interstellar medium has not yet been reported (Klisch et al. 1996), but electronic transitions have been measured in the solar atmosphere by Berdyugina (2002b).

5.3.2 SH^+, NH^+ and H_2O^+

Since no data is available for the SH^+, NH^+ and H_2O^+ ions in the JPL database and CDMS, the literature[16] has been consulted for spectroscopic constants. A set of sufficiently accurate rotational, fine structure and hyperfine structure constants and at least a first order correction for higher rotational states can be used together with a dipol moment to calculate the required molecular transitions. The prediction of new lines from the constants have been performed with the `SPCAT`-Code (Pickett 1991) and the resulting transitions are in the format of the JPL database or the CDMS (Fig. 20). The calculated data is then processed in the same way as discussed in the previous section.

[16] A starting point for a search is J. Crovisiers database for constants of molecules of astrophysical interest, available at http://wwwusr.obspm.fr/~crovisie/basemole/

For the calculation of the line intensities, we have assumed a temperature of 300 K as in the JPL database and the CDMS. Beside the transition frequency and the line intensity, `SPCAT` also calculates the partition function of the rotational- and spin- states. The contributions of vibrational or electronic states to the partition function can be neglected, since the partition function can be approximated by the separation in factors for the rotational, vibrational and electronic motion by

$$Q \approx Q_{rot.} \cdot Q_{vib.} \cdot Q_{el.} \ , \tag{94}$$

With the partition function for a single mode of motion

$$Q_{mode} = \sum_i g_i \cdot exp\left(-\frac{E_i}{kT}\right) \ , \tag{95}$$

where E_i is the energy and g_i the degeneracy of the state i. The sum has to be taken over all states. For the later calculated SH^+, the rotational ground state of the first vibrational excited level lies at 2449.2217 $cm^{-1} \approx 3600$ K above the ground state (Hovde & Saykally 1987) and for temperatures up to a few hundred Kelvin, the contribution of the vibrational partition function is therefore below 10^{-2}.

SH^+

The single ionized sulfur hydrogen SH^+ has a $X^3\Sigma^-$ ground state and can be described by Hund's case (a). The spectra of SH^+ including fine structure and hyperfine structure has been measured by Hovde & Saykally (1987). Rotational constants from therein and more accurately measured hyperfine structure transitions have been combined by Savage et al. (2004a) to which we refer for the spectroscopic constants (Tab. 3). The transition dipol moment of 1.29 Debye was also taken from this paper. Using `SPCAT`, 258 lines were calculated and therefrom 42 fit the frequency range of HIFI. In Tab. 4, the calculated partion function is presented. The state of the molecule can be expressed by the quantum numbers N for the rotation, J for the total angular momentum and F for the hyperfine structure. For the Hund's case (a) with a Σ ground state, the coupling scheme

$$J = N + S \tag{96}$$
$$F = I + J \ , \tag{97}$$

with the total electron spin S and the total nuclear spin I, applies.

Spectroscopic Constant	Value [MHz]
B (rotational)	273808.4 ± 2
D (rotational distortion)	14.502 ± 0.114
γ (spin-spin)	-4972.52 ± 0.15
λ (spin-rotation)	171234.04 ± 0.34
b_F (hyperfine structure)	-56.87 ± 0.24
c (hyperfine structure)	33.4 ± 2

Table 3: Spectroscopic constants of SH^+ (Savage et al. 2004a)

A large estimated error of the rotational constant B leads to uncertainty in the transition frequency. But for transitions with frequency in the range of the HIFI-Band 1 and 2, the error is withhin 4 MHz and thus still acceptable. The increasing of the error regarding J due to B is almost quadratically (c.f. Sect. 4.4) and the uncertainty of frequency for HIFI-Band 6 is approximately 17 MHz, which is too much for a reliable identification of the transition.

The SH^+ ion has so far not been detected in space.

Temperature [K]	Q(T)
300.000	139.0024
225.000	104.6303
150.000	70.3183
75.000	36.1159
37.500	19.1664
18.750	10.9180
9.375	7.2043

Table 4: Partition function of rotational and spin states for SH^+.

NH^+

An attempt to calculate transitions of the nitrogen hydride ion NH^+ was performed with rotational constants from Colin (1989), hyperfine structure constants from Verhoeve et al. (1986) and a transition dipol moment from de Almedia et al. (1981). The ground state of NH^+ is a regular $X^2\Pi$ state, but the energy of the first exited state $a^4\Sigma^-$ lies only about 500 cm^{-1} above the ground state. Therefore, transitions between the $X^2\Pi$ and $a^4\Sigma^-$ are possible and the energy of the ground state is altered. This can be taken into account by perturbation theory. Unfortunately, the `SPCAT`-code does not support this. Additionally, the rotational constant B for the $X^2\Pi$-state is given by Colin (1989) with an error of $\pm$ 26 MHz and therefore, the uncertainty of the $J = 1 \rightarrow 0$ transtition (at approximately 1000 GHz) would be higher than 50 MHz.

Verhoeve et al. (1986) give the observed frequencies for 12 resolved hyperfine structure transitions in the ground state $X^2\Pi$ ($J = \frac{3}{2} \leftarrow \frac{1}{2}$) with an accuracy of $\pm$ 2 MHz. Using the transition dipol moment of de Almedia et al. (1981), it should be possible to calculate Einstein-A-Coefficients. A sufficiently accurate[17] partition function for NH^+ could be calculated with energies, obtained from the constants in Verhoeve et al. (1986). (However, this was not done due to lack of time.)

H_2O^+

The water ion is an important species in the chemical network of water. It is mainly formed by the reactions

$$OH^+ + H_2 \rightarrow H_2O^+ + H \quad (98)$$
$$H_2O + H^+ \rightarrow H_2O^+ + H \quad (99)$$

and destroyed by collisions with H_2 resulting in H and H_3O^+, which is an important molecule for the formation of water (Stäuber et al. 2005b). The water ion has been detected in the tail of the comet Kohoutek in optical wavelengths (Wehinger et al. 1974), but an observation in the interstellar medium is still pending.

Not like the molecules discussed before, H_2O^+ consists of three atoms. The structure of the water ion is asymmetric in the sense that that three distinct rotational axis have to be considered. Therefore the spectra is far more complicated than for diatomic molecules. The actual rotation of the molecule is expressed by the principal quantum numbers N, K_a and K_c. Often, this three quantum numbers are combined in the notation $N_{K_a\,K_c}$. The total angular momentum J provides together with the coupling scheme $N + S = J$ information on the electron spin state. The sum of the hydrogen nuclear spins is expressed by the quantum number $I_H = I_{H_1} + I_{H_2}$ and the total nuclear spin I_{tot} forms together with J the quantum number $F = J + I_{tot}$. Notice, that oxygen

[17] A calculation of the partion function of SH^+ without resolved fine structure levels and inaccurate constants showed differences to the partition function in Tab. 4 of only a few percent.

has no nuclear spin.

For the calculation of the H_2O^+ - lines, we have used spectroscopic constants from Strahan et al. (1986) and a transition dipole moment of 2.4 Debye, obtained from http://wwwusr.obspm.fr/~crovisie/basemole/ (without reference therein). Totally 235 of the calculated transitions fit in the HIFI frequency range, but only 139 remained when lines with an estimated error larger than 30 MHz were separated. Most of the remained lines in HIFI Band 1,2,4 and 5 have an accuracy better than ±3 MHz, but no accurate line for HIFI Band 3 is available. Many of the transitions in HIFI Band 6 have an estimated error of 5 MHz or larger. The partition function of H_2O^+ is presented in Tab. 5.

Temperature [K]	Q(T)
300.000	376.4331
225.000	252.9054
150.000	140.7429
75.000	51.1707
37.500	19.2995
18.750	8.8040
9.375	6.3129

Table 5: Partition function of rotational and spin states for H_2O^+.

5.3.3 Collision rate coefficients

For the solution of the radiative transport problem in the non local thermal equilibrium, collision rate coefficient are required (c.f. Sect. 3.1). Since H_2 is by far the most abundant molecule in clouds around YSOs, the collision rate coefficients between H_2 and the considered molecule are sufficient to solve a radiative transport problem. Para-H_2 ($J = 1$) and ortho-H_2 ($J = 0$) should be distinguished, since the rate coefficient can differ by a factor of 2 to 5 due to supplementary terms in the interaction potential. The accuracy of the collision rate coefficents is still problematic and the estimated error is often larger than ± 50 %.

For the molecules discussed above, no collision rate coefficients were found in LAMDA or literature. However, for CH^+, OH^+ and H_2O^+ collision rates may be not necessary (c.f. Sect. 5.3.4), since reactions of these ions with H_2 are exothermic (i.e. the molecules are destroyed rather than being excited or deexcited). Schöier et al. (2005) present different ways to estimate collisonal rate coefficients:

Ab intion calculation: For a theoretical determinition, first, the interaction potential of the colliding system has to be calculated and then the collision dynamics is determined. The second step can be performed very accurately with an absolute error less than some percent. The first step, that involves quantum chemistry models, provides the largest source of uncertainty.

Adaption of data: A first rough estimation of the collsional rate coefficients can be obtained by the adaption of available data to the considered molecule. The rate coefficient is the Maxwellian average of the energy dependent collision cross section $\sigma(E)$,

$$K_{ul} = \sqrt{\frac{8}{\pi\mu}} \frac{1}{(kT)^{\frac{3}{2}}} \int \sigma(E) E e^{-E/kT} dE \ , \tag{100}$$

with k the Boltzmann constant, E the center of mass collision energy and μ the reduced mass of the system. If only data for the collision $A \leftrightarrow H_2$ is available, the cross section in

the collision $B \leftrightarrow H_2$ can be assumed to be the same in a first order approximation. The collision rate coefficient can then be expressed as

$$K_{B\leftrightarrow H_2} = K_{A\leftrightarrow H_2} \cdot \sqrt{\frac{\mu_{A\leftrightarrow H_2}}{\mu_{B\leftrightarrow H_2}}} \ . \tag{101}$$

This procedure works best for a substitution of a hydrogen atom by a sulfur atom (O→S, e.g. HCS^+ coefficients adapted from HCO^+ data) since they have a similar structure.

The above mentioned procedure would be possible for SH, since LAMDA contains collision rate coefficients of OH. The assignment of the OH collision rate coefficents to SH states is complex due to the different labeling of the quantum states in the JPL database and due to LAMDA does not provide any information on the quantum numbers of the levels. Therefore this has not yet been done. For CH and NH, measured rate coefficients and an approximation is still lacking.

5.3.4 Excited formation

The extremly reactive molecule CH^+ is well observed in the interstellar medium, but the measured column densities are inconsistent with the assumed low-temperature chemistry (Gerin et al. 2005): The CH^+ ion is mainly formed by the endothermic reaction $C^+ + H_2 \rightarrow CH^+ + H$, which is slow at temperatures of a few 10 Kelvin. As discussed before, CH^+ is very rapidly destroyed by reactions with H_2, leading to a predicted abundance that is much lower than the observed. A possible reason to explain this underestimation is the failing of the assumption of uniform physical conditions: The formation of species in endothermic reaction takes place in small regions with altered physical conditions. Magneto-hydrodynamical shocks or turbulent dissipation can locally heat the gas up to temperatures in the magnitude of the activation energy of the $C^+ + H_2$ reaction (about 4600 K, Gredel 1997).

A correlation between the abundance of CH^+ and CH was found by Gredel (1997) and Crane et al. 1995. The plot of the CH^+ and CH column densities versus the total hydrogen column density shows a ratio of CH^+ and CH between 0.2 and 3.5. An alternative model for CH^+ was therefore calculated by scaling the abundances of CH by a factor of 0.2. Line intensities calculated in this way can thus be considered as a lower limit. Since the CH^+ / CH abundances were observed in absorption of dark clouds towards bright stars rather than in YSOs, the scaling factor is questionable though and the results should be treated carefully. The upper limit of the intensity would be achieved for a scaling factor of 3.5, but since a larger abundance of the ionized CH^+ than the neutral CH is unlikely in envelopes of YSOs, the calculation was not carried out.

Since CH^+ undergoes reactions with H_2 very rapidly, collisions between the two molecules may not lead to an excitation and a subsequent radiation. Therefore, a formation in an excited state followed by a fast radiatve process, like

$$A + B \rightarrow C^* \rightarrow C + h\nu \ , \tag{102}$$

may happen (c.f. Sect. 2.2). The observed radiation would therefore depend on the formation rate and not on the absolute abundance. Since this could not be easily included into the chemical model and no data on the level population after an excited formation is available yet, we have calculated the model with scaled CH abundance assuming a Boltzmann distribution.

Reactions of the OH^+, NH^+ and H_2O^+ ions with H_2 are also exothermic and therefore the same problem as for CH^+ may occur. Since no information on the observed fractional abundances or the excitation mechanism of these ions was found, we did not calculate further models. The activation energy of the reaction between SH^+ and H_2, however, is high enough to treat the molecule as collisionally excited.

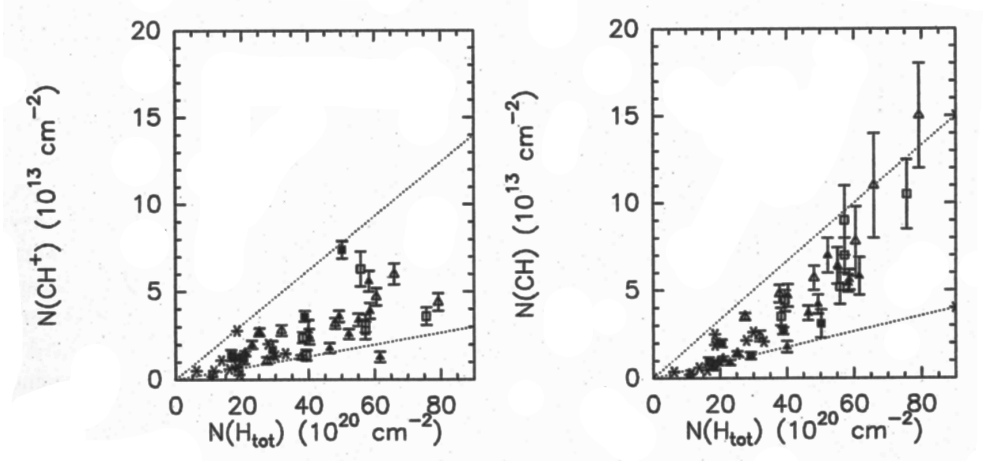

Figure 21: Column densities of CH^+ and CH as a function of the total hydrogen column density (Gerin et al. 2005, with data from Gredel 1997 and Crane et al. 1995).

5.4 Line intensities

Since no collision rate coefficients were available for the considered molecules and the excitation mechanism of some molecules is ambiguous, a complete calculation of the radiative transport problem could not be carried out. The level population was therefore assumed to be in local thermal equilibrium (LTE), which is, however, only approximative for the physical conditions around YSOs. For a molecule with a total density n, the density n_j of molecules in the state j with energy E_j can therefore be expressed by

$$n_j = n \cdot \frac{g_j e^{-\frac{E_j}{kT}}}{Q(T)} \ , \tag{103}$$

with T, the kinetic gas temperature, g_j the degeneracy of the state and $Q(T)$ the partition function (c.f. Sect. 3.3). The partition function of the individual molecules is given in the JPL database and the CDMS for 7 different temperatures (9.375, 18.75, 37.5, 75, 150, 225 and 300 K). Since the innermost calculated point of AFGL 2591 exceeds this temperature range, an extrapolation is needed. To calculate the partition function for points in outer shells, an interpolation is necessary. The CDMS lists partition functions for a few diatomic species up to 1000 K. It is found that a quadratic extrapolation of points for temperatures less than 300 K fits best with points for higher temperatures. Therefore a quadratic interpolation / extrapolation has been used for all temperatures.

After the level population for each grid point of the chemical model is assumed, the emitted intensity can be calculated. This was performed using the radiative transport problem solver `RATRAN` (Hogerheijde & van der Tak 2000), which consists of the `AMC` and the `SKY`-code. `AMC` calculates the level population by an accelerated Monte Carlo algorithm (c.f. Sect. 3.5). The actual intensity and shape of the line is then calculated by `SKY`, that integrates along the line of sight through the molecular cloud. Since the population of the levels is already fixed by the LTE assumption, only `SKY` was used. An IDL - script calculated the LTE level population[18] and arranged the required input files.

In addition to the chemical abundances and level populations, further assumptions had to be made for the calculation with `SKY`:

- The line profile is taken to be Gaussian and the Doppler Parameter b [km s^{-1}] (Full width half maximum times 0.6) is fixed to a value, because no information is available on micro-

[18] Another - more time consuming - possibility would be to use AMC with large arbitrary collision rate coefficients.

turbulences in the considered YSOs. For AFGL 2591 and all models of IRAS 16293-2422, we have taken $b = 1.6$ km s^{-1} and for TMC 1 $b = 1.0$ km s^{-1} was assumed. Since all lines studied in our sample are optically thin, the calculated line shape is Gaussian and the value of b should have no influence on the integrated line intensity. Therefore, the brightness temperature is the integrated line intensity divided by $\sqrt{\pi} \cdot b$.

- A background radiation of 2.735 K (from the cosmic microwave background radiation) was assumed. Dust emission was not taken into account.
- All velocity fields were switched off.
- The frequency resolution of the simulated spectra was set to 0.1 km s^{-1} and 250 channels were calculated. Distances were chosen as described before (Sect. 5.2). The spatial resolution of the 2 dimensional `SKY` images were set to $0.1''$ for all models. The sizes of the images are taken to $60'' \times 60''$ for AFGL 2591, $90'' \times 90''$ for IRAS 16293-2422 and $57'' \times 57''$ for TMC 1.

A telescope measures a broad area rather than a single point due to the limited angular resolution. The observed spectra $O(\alpha, \delta)$ is therefore the convolution of the source intensity $S(\alpha, \delta)$ with a beam response function $B(\alpha, \delta)$

$$O(\alpha, \delta) = S * B = \int\int S(\tilde{\alpha}, \tilde{\delta}) \cdot B(\tilde{\alpha} - \alpha, \tilde{\delta} - \delta)\, d\tilde{\alpha} d\tilde{\delta} \ , \tag{104}$$

We have assumed a Gaussian beam response function, with full width at half maximum (FWHM) after Tab. 6, depending on the frequency of the calculated line. This convolution was carrierd out with "convol" from the `Miriad` package and is the most time-consuming step in calculating line intensities. To conserve the flux in the convolution, a scale factor f was introduced by

$$f = \frac{4 \cdot ln(2)}{\pi} \left(\frac{p}{B}\right)^2 \ , \tag{105}$$

with the FWHM of the beam response function B and the size of the pixel p (in our calculation $0.1''$). The factor $4 \cdot ln(2)/\pi$ corrects the difference between the round beam and the square pixels of the `SKY` image.

Hifi-Band	Frequency Range [GHz]	Beamwidth [arcsec]
1	480-640	39
2	640-800	30
3	800-960	25
4	960-1120	21
5	1120-1250	19
6	1410-1910	13

Table 6: Half power beamwidths and frequency range for the 6 HIFI Bands (after http://www.sron.rug.nl/hifiscience/).

The integrated line intensity was finally determinated with "Class" from the GILDAS package. An example of calculated emission lines for AFGL 2591 is given in Fig. 22.

5.5 Selection of lines for Herschel

In order to schedule observations with HIFI, the object (i.e. the coordinates α and δ) as well as the frequency have to be defined. HIFI can observe a bandwidth of 4 GHz simultaneously. Therefore, the most promising transitions for a detection have to be determined: For a reliable identification of molecules, at least three lines should be observed. To calculate physical condition from a spectra, the line strength should be as big as possible. Good candidates for a first identification of a molecule therefore are hyperfine structure transitions, since their line frequency often lies in a range of a few tenth MHz. Additionally, they have similar excitation temperatures due to the comparable energy of the upper state. Their line intensity therefore can be estimated by scaling with Einstein-A-Coefficients. To obtain physical conditions as well as the excitation temperature, lines with different energies in the upper state are required.

One of the aims of our calculation is to determine the strongest line for each HIFI Band (Tab. 6). Since a full calculation of all line strengths for the molecules in our sample would be too time-consuming, a simplified calculation to estimate relative line strenghts was carried out for all transitions and models: The density $n_u(i)$ of molecules in the upper state u at the grid point i of the chemical model is known due to the LTE assumption[19]. For a transition $u \rightarrow l$, the emission per volume per second is therefore the density $n_u(i)$ times the Einstein-A-Coefficent A_{ul}. Since the emitting area is assumed to be a sphere of radius R, its volume is R^3. The integration along the line of sight is roughly included by taking R^2 instead of R^3 and we assume a perfectly optical thin radiation. Thus, the intensity of the whole cloud consisting of 30 shells is approximately proportional to

$$I_{ul} \propto \sum_{i=1}^{29} (R_{i+1}^2 - R_i^2) \cdot A_{ul} \cdot n_u(i) \ . \tag{106}$$

A comparison between relative intensities estimated in this way and the ones calculated fully as described in Sect. 5.4 showed an agreement within a few percent. This is likely due to the optically thin radiation. Therefore, line intensities of hyperfine transitions that were not calculated can easily be estimated by scaling with the Einstein-A-Coefficient.

The obtained relative intensities were then used to sort the transitions by their intensity. Since the order of the strongest lines showed no difference for the considered models (AFGL 2591, the four models of IRAS 16293-2422 and TMC 1), a common set of selected transitions was established. For every molecule, at least one transition per HIFI Band was selected. The selected frequencies were compared in a range of $\pm$ 15 MHz (equivalent to 4.5 km s^{-1} at 1 THz) with the JPL database to find interfering lines. When transitions of molecules, already observed in YSO, were found, their line strenghts was roughly estimated by the line intensity (from the database) and their supposed abundance. If a comparable intensity is achieved, the selected line was replaced.

The list of selected transitions is given in Tab. 7. For diatomic molecules, the transitions are denoted by the quantum number of the actual rotation of the molecule (N or K). The levels of H_2O^+ are given in the format $N_{K_a K_c}$. Fine and hyperfine structure transitions are indicated by the quantum number S for the total electron spin and F for the nuclear spin.

[19] The same procedure is also applicable for Monte-Carlo calculation, since all level populations are known after the calculation with AMC.

CH

Only lines in HIFI Band 1 and 6 were found for CH. Each of the four selected lines belong to a triplet of hyperfine structure transitions. The quantum state of the two lines in Band 6 differ only by their parity and the difference in the frequency is therefore due to the Λ-type doubling phenomena.

CH^+

Since only two transitions of CH^+ were found, both were selected for the calculation. Both are pure rotational transitions.

NH

The 946.4758 GHz transition of NH in Band 3 belongs to a multiplet of 9 hyperfine structure lines in a frequency range of 147 MHz. In Band 4, the three strongest lines were selected. Due to the HCN line at 974.4884 ± 0.0004 GHz, the three not resolved hyperfine structure lines at 974.4786 GHz were replaced by the pure rotational line at 974.4708 GHz.

OH^+

For OH^+, line frequencies in HIFI Band 3, 4 and 6 were found. For Band 3 and 6, the strongest lines were chosen. In Band 4 we have selected the strongest line of the hyperfine structure triplet at 971 GHz and of the quadruplet (due to the simultaneous spin change $S = 0 \rightarrow 1$) at 1032 / 1033 GHz.

SH

The transitions of SH are in HIFI Band 3 and 6. Lines are grouped in triplets due to hyperfine structure splitting. As mentioned in Sect. 5.3, some of the lines in the HIFI frequency range belong to the first excited vibrational state and the upper level has therefore too highan energy to get excited in the environment of YSOs. Out of the remaining 12 lines, the strongest of each triplet was chosen. The 866.9467 GHz line belongs to a not resolved hyperfine structure transition and the quantum number of the not resolved hyperfine component is given in brackets. The two lines in Band 6 show Λ-type doubling, as CH. The selected 1447.0123 GHz transition lies withhin 2 MHz to the other components of its hyperfine triplet and a resolved observation will therefore not be possible.

SH^+

Lines of SH^+ are predicted in all HIFI Bands. The selected lines in Band 1, 4 and 6 are pure rotational transitions. In Band 5, the 1230.6275 GHz line is affected by a transition of CH_3CN and was therefore replaced by the almost equally strong line at 1230.5673 GHz. The selected line in Band 4 at 1082.9094 GHz is close to the SO_2 line at 1082.9075 GHz: The abundance of SO_2 in the chemical model is about 5 orders of magnitude higher than that of SH^+ and the Einstein-A-Coefficient of the SO_2 transition is with $1.8 \cdot 10^{-3}$ s^{-1} about two times bigger than the one for SH^+. Since the upper level of the SO_2 line has a temperature of approximately 2500 K, the SH^+ line should not be affected. A further calculation could be carrierd out with the 1094.7724 GHz line which is less disturbed.

H_2O^+

For H_2O^+, lines in all HIFI Bands were found. In Band 1, 2 and 4 the strongest lines were selected. The 876.8793 GHz (Band 3), 1139.5719 GHz (Band 5) and 1625.6044 GHz (Band 6) lines are close to CH_3CN transitions and were therefore replaced.

Molecule	Transition	Frequency ν ($\Delta\nu$) [GHz] ([MHz])	Band	Einstein-A $[s^{-1}]$	E_{up} $[K]$
CH	$1^+ \rightarrow 1^-$ $S = \frac{1}{2} \rightarrow -\frac{1}{2}$	532.7255 (0.6)	1	6.6(-4)	25.7
	$1^- \rightarrow 1^+$ $S = \frac{1}{2} \rightarrow -\frac{1}{2}$	536.7627 (0.6)	1	6.8(-4)	25.8
	$1^- \rightarrow 0^+$	1656.9563 (0.7)	6	4.0(-2)	105.2
	$1^+ \rightarrow 0^-$	1661.1024 (0.7)	6	4.0(-2)	105.5
CH^+	$1 \rightarrow 0$	835.079 (1)	3	2.3(-3)	40.1
	$2 \rightarrow 1$	1669.1595 (60)	6	2.2(-2)	120.2
NH	$1 \rightarrow 0$ $S = -1 \rightarrow 1$	946.4758 (0.1)	3	3.3(-3)	45.4
	$1 \rightarrow 0$	974.4708 (0.3)	4	5.7(-3)	46.8
	$1 \rightarrow 0$ $S = 0 \rightarrow 1$	999.9734 (0.1)	4	5.2(-3)	48.0
	$1 \rightarrow 0$ $S = 0 \rightarrow 1$ $F = \frac{3}{2} \rightarrow \frac{5}{2}$	1000.0010 (0.1)	4	2.9(-3)	48.0
OH^+	$1 \rightarrow 0$ $S = -1 \rightarrow 1$	909.1588 (1)	3	1.1(-2)	43.6
	$1 \rightarrow 0$	971.8038 (2)	4	1.8(-2)	46.6
	$1 \rightarrow 0$ $S = 0 \rightarrow 1$	1033.1186 (1)	4	1.8(-2)	49.6
	$2 \rightarrow 1$ $S = -1 \rightarrow 0$	1892.2272 (2)	6	5.9(-2)	140.4
SH	$2 \rightarrow 1$ (F=2 $\rightarrow$ 1)	866.9467 (0.1)	3	2.0(-3)	571.2
	$2 \rightarrow 1$	875.2671 (0.1)	3	1.5(-3)	572.0
	$3^+ \rightarrow 2^-$	1447.0123 (0.1)	6	8.1(-3)	640.6
	$3^- \rightarrow 2^+$	1455.1005 (0.1)	6	8.2(-3)	641.8
SH^+	$1 \rightarrow 0$	526.0480 (4)	1	9.7(-4)	25.2
	$1 \rightarrow 0$ $S = 0 \rightarrow 1$	683.4168 (4)	2	1.5(-3)	32.8
	$2 \rightarrow 1$ $S = 0 \rightarrow 1$	893.1406 (9)	3	2.5(-3)	75.7
	$2 \rightarrow 1$	1082.9094 (9)	4	9.9(-3)	77.2
	$2 \rightarrow 1$ $F = \frac{1}{2} \rightarrow \frac{1}{2}$	1230.5673 (9)	5	6.8(-3)	75.7
	$3 \rightarrow 2$	1632.5175 (17)	6	3.6(-2)	155.6
H_2O^+	$1_{10} \rightarrow 1_{01}$	607.2582 (1)	1	6.20(-3)	59.2
	$2_{02} \rightarrow 1_{11}$	742.0332 (1)	2	3.6(-3)	89.1
	$5_{23} \rightarrow 4_{32}$	841.9973 (27)	3	1.3(-3)	580.7
	$1_{11} \rightarrow 0_{00}$	1115.0860 (1)	4	3.1(-2)	53.5
	$1_{11} \rightarrow 1_{00}$ $F = \frac{3}{2} \rightarrow \frac{1}{2}$	1139.5152 (1)	5	1.5(-2)	54.7
	$2_{12} \rightarrow 1_{01}$	1638.2007 (1)	6	7.3(-2)	108.7

Table 7: Selected lines for HIFI.

5.6 Results and Discussion

The results of the calculations can be found in Tab. 10 - 15. For each of the calculated chemical models with different X-ray fluxes, the integrated line intensity $\int T_{mb} dv$ is given in the format $a(b) \equiv a \cdot 10^b$. The integrated line intensity was determined by fitting a Gaussian profile to the calculated spectra. To obtain the brightness temperature T_{mb} instead of the line intensity, a Doppler Parameter b [km s^{-1}], which is depending on the kinetic temperature and microturbulences, has to be assumed. Dividing the integrated intensity by $b \cdot \sqrt{\pi}$ gives then the brightness temperature.

Estimated observation time

The required observation time to measure the calculated lines with HIFI can be estimated by using T_{rms} [K], the Root Mean Square[20] (RMS) temperature of the noise level. To ensure a detection, the brightness temperature of the considered line should be at least three times higher than T_{rms} (c.f. Sect. 6). The radiometer equation (Kraus 1966) gives a relation between T_{rms} and the integration time t_{tot} [s]

$$T_{rms} = \frac{T_{sys}}{\sqrt{A \cdot \Delta\nu \cdot t_{tot}}} \ , \tag{107}$$

with the bandwidth $\Delta\nu$ [s^{-1}] of each recorded channel, the noise power of the instrument (receiver, antenna etc.) indicated by the "system temperature" T_{sys} [K] and an efficiency factor A depending on the mode of the observation. For HIFI, this parameters are given in Tab. 8. The two spectrometers of HIFI have a spectral resolution of 1 MHz and 134 kHz, respectively. For our calcuation, we have assumed the 1 MHz resolution, an observation with 134 kHz would however take 7.5 times longer. The efficiency was chosen to be 0.125 for an on-off-source observation. The achieved sensitivity after an integration time of 3 minutes up to 5 hours is presented in Fig. 23. This figure also shows the limitations of the sensitivity: As T_{rms} is proportional to $1/\sqrt{t_{tot}}$, the total integration time must be 100 times longer to achieve one order of magnitude in T_{rms}. On the other hand, t_{tot} is highly sensitive on changes of T_{rms}, especially for low values.

Parameter	Value
efficiency factor (observation mode)	$A = 0.25$ (frequency switching) $A = 0.125$ (on-off-source) $A = 0.3 - 0.5$ (on-the-fly)
system temperature	$T_{sys} = 200\,\mathrm{K} \cdot (\nu\,[\mathrm{GHz}]/500[\mathrm{GHz}])$ (Band 1-5) $T_{sys} = 1600\,\mathrm{K}$ (Band 6)
Frequency resolution	$\Delta\nu = 134\,\mathrm{kHz}, 1\,\mathrm{MHz}$

Table 8: Parameters for the radiometer equation for HIFI in different observation modes (from http://www.strw.leidenuniv.nl/~kempen/HIFI/integr.php)

A list of the estimated integration times for the calculated molecules is given in Tab. 9. For every model / transition, the strongest line was chosen to calculate the integration time. The RMS temperature T_{rms} was assumed to be one third of the line strengths, corresponding to a signal-to-noise ratio of about 3. Estimated integration times longer than 10^3 hours are left out and only transitions with at least one value below this cut-off are given in the table. To compare integration times and intensities of TMC 1 with the other models, one has to keep in mind that the Doppler parameter for TMC 1 was 1 km s^{-1} in contrast to 1.6 km s^{-1} (AFGL 2591 and IRAS 16293-2422).

[20] The RMS or quadratic mean x_{rms} of a collection of n values $x_1, x_2, \ldots, x_n$ - in our case the recorded channels $T_1, T_2, \ldots, T_n$ - is defined by $x_{rms} = \sqrt{\frac{1}{n}\sum_{i=1}^{n} x_i^2}$.

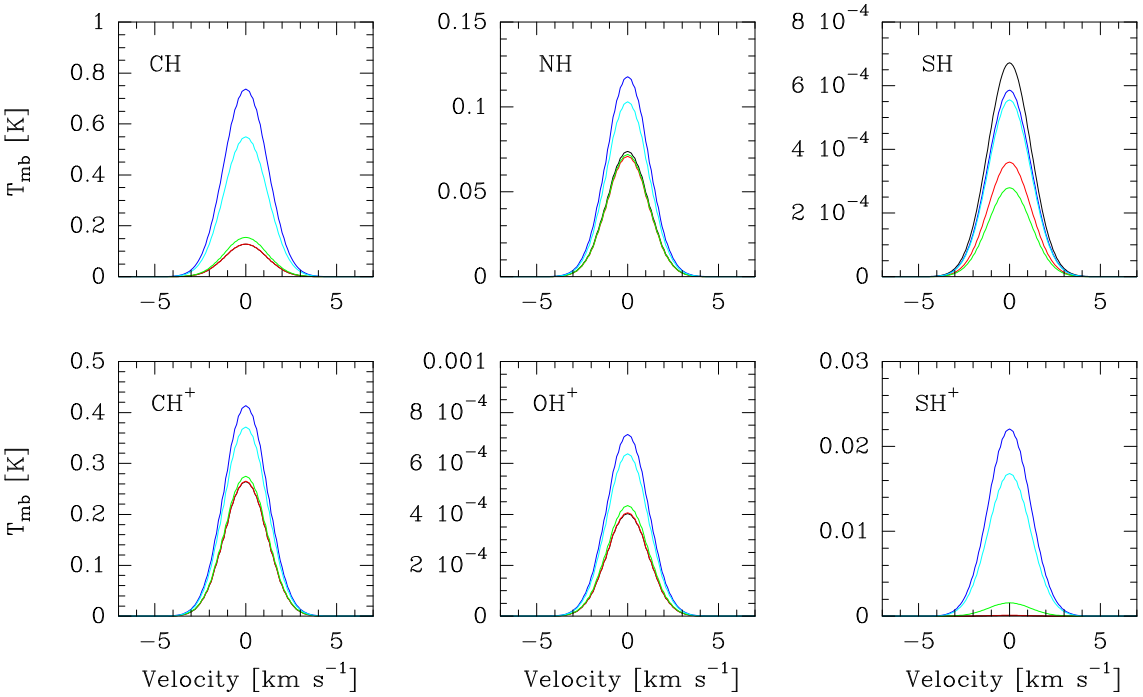

Figure 22: Calculated line profiles for AFGL 2591. For each calculated molecule, the strongest line was chosen. For CH^+, the alternative model is plotted. The different models are indicated by the line color: Model 0 (black), Model 1 (red), Model 2 (green), Model 3 (blue) and Model 6 (cyan). The transition frequencies are 1656.9563 GHz for CH, 835.079 GHz for CH^+, 974.4708 GHz for NH, 971.8038 GHz for OH^+, 1455.1005 GHz for SH and 1632.5175 GHz for SH^+.

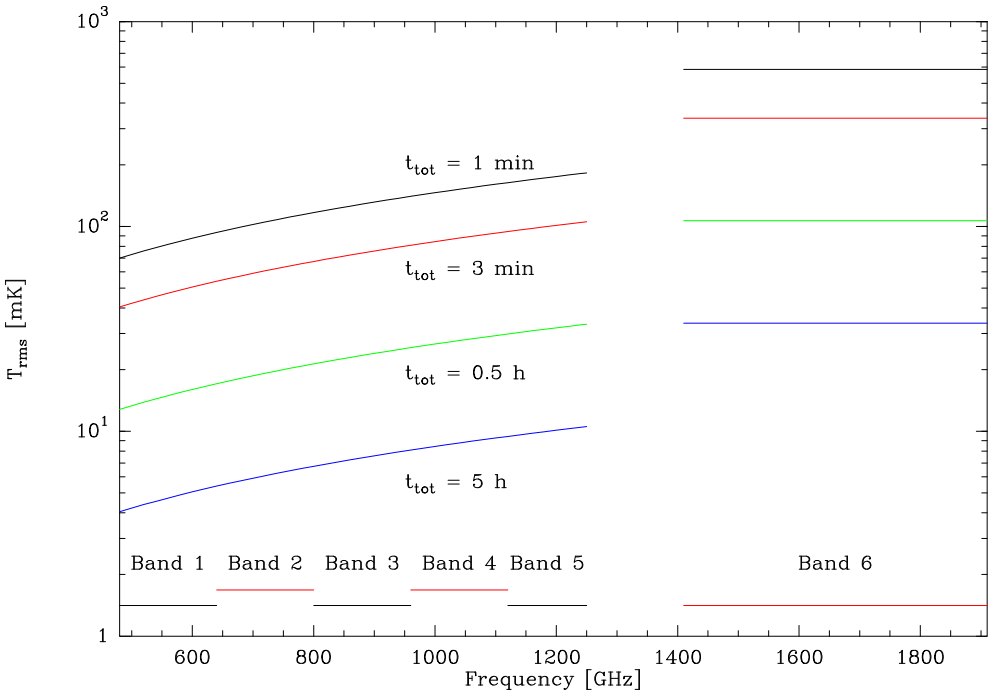

Figure 23: Sensitivity of HIFI for an on-off-source measurement with a spectral resolution of 1 MHz. The RMS Temperature T_{rms} is given in mK. The integration time is 5 h (blue line), 0.5 h (green line), 3 min (red line) and 1 min (black line).

Molecule	Frequency [GHz]	AFGL 2591	IRAS 16293 (a)	IRAS 16293 (b)	IRAS 16293 (c)	IRAS 16293 (d)	TMC 1
CH	532.7255	24.1 s	11.0 h	35.1 min	1.9 h	23.9 min	17.8 s
	536.7627	24.0 s	10.9 h	34.9 min	1.9 h	23.8 min	17.8 s
	1656.9563	5.1 min	-	33.2 min	505.0 h	33.3 min	4.1 min
	1661.1024	5.1 min	-	33.4 min	510.0 h	33.5 min	4.2 min
CH^+	835.079	43.4 s	42.9 h	18.7 min	5.8 h	15.5 min	19.2 s
alternat.	1669.1595	22.4 min	-	2.8 h	-	2.8 h	14.3 min
NH	946.4758	1.8 h	31.4 min	1.7 min	2.6 h	3.5 min	2.2 min
	974.4708	12.7 min	5.2 min	13.1 s	23.2 min	24.9 s	18.6 s
	999.9734	19.6 min	8.2 min	19.6 s	36.0 min	36.7 s	27.5 s
	1000.0010	2.3 h	56.3 min	2.0 min	4.1 h	3.8 min	2.5 min
OH^+	971.8038	-	-	-	-	665.2 h	150.8 h
	1033.1186	-	-	-	-	-	663.2 h
H_2O^+	1115.0860	-	-	-	-	-	232.5 h

Table 9: Estimated integration times for a $3 \cdot T_{rms}$ detection. Integration times longer than 10^3 hours have been suppressed. The four IRAS 16293-2422 models are label by (a) age 10^5 y / (b) age 10^5 y & protostellar hole / (c) age 10^4 y / (d) age 10^4 y & protostellar hole.

As shown in Tab. 9, no transitions of the considered ions (OH^+, SH^+, H_2O^+ and CH^+ with abundances according to the chemical model) were found with reasonable observation times. This is due to their very low density, since for all ions, there would be transitions with upper level energy and Einstein-A-Coefficient in the same order of magnitude as NH, for example. Fig. 14-19 also confirm this.

The lines of SH might be missing due to the same reason. In addition, the upper level energies correspond to temperatures one order of magnitude higher than those of NH. Levels with an upper energy equivalent to 500 K are, compared to those with 50 K, in the LTE assumption at a temperature of 50 K by a factor of $exp(9) \approx 10^4$ less populated. This is reflected in the calculated integrated intensities (Tab. 10 - 15): The integrated intensity of SH for IRAS 16293-2422 is three to nine (!) orders of magnitude smaller for the two models with a protostellar hole. The kinetic temperature for those models at the innermost point is only 40 K compared to 270 K for models without a protostellar hole. The 841.9973 GHz transition of H_2O^+ also shows this feature.

Integrated line intensities of CH^+ are about 5 orders of magnitude smaller than those of CH, whereas the alternative model of CH^+ has comparable integrated intensities. Comparing the 532.7255 GHz line of CH with the 835.079 GHz line of CH^+, this is very likely: The chemical abundances of the alternative CH^+ model were obtained by scaling the model of CH by a factor of 0.2 and the kinetic temperatures are comparable to the energy of the upper level in a wide range of the model. Since the Einstein-A-Coefficient of the CH^+ transition ($2.3 \cdot 10^{-3}$ s^{-1}) is about a factor of 4 larger than the coefficient for CH ($6.6 \cdot 10^{-4}$ s^{-1}), a similar intensity is achieved.

AFGL 2591

Despite the mass of AFGL 2591, which is about 1200 times larger than for TMC 1, the line intensities are of the same order, if the central source of TMC 1 is assumed to be a very strong X-ray emitter ($L_x = 10^{32}$ $ergs^{-1}$). Due to the very strong enhancement of the molecules by X-rays in TMC 1 (c.f. Fig. 19) the absolute abundances of the considered molecules can compete with those of AFGL 2591, even if TMC 1 has a much lower mass. The radiation of TMC 1 is also supported by its shorter distance of 140 pc compared to about 1 kpc for AFGL 2591, leading to a dilution of the luminosity by a factor of 50 compared with TMC 1.

Some lines of AFGL 2591 are strongly enhanced by X-rays, e.g. those of CH^+ or the two lines of CH at 1656.9563 GHz and 1661.1024 GHz are five times stronger for model 3 than for model 0 without radiation. Both lines of CH and the 1669.1595 GHz line of CH^+ still indicate X-ray enhancement, if we take a calibration uncertainty of 30 % into account. Line intenities of other transitions, especially those of SH^+ and the 841.9973 GHz transition of H_2O^+ are even more enhanced by X-rays (up to factors of 500) but have unfortunately a very weak absolute intensity.

The intensity of SH for model 1 and 2 are by a factor of 2 lower than those of model 0. This is likely due to the lower abundance for these models in the innermost area (c.f. Fig. 14), where temperatures are high enough to excite the upper state.

IRAS 16293-2422

The intensities of IRAS 16293-2422 depend very much on the chosen model. For the model with a chemical age of 10^4 and a protostellar hole, the strongest line intensities are achieved for all molecules except NH. Compared to AFGL 2591, the intensities of CH and CH^+ are about 1 order of magnitude weaker, whereas NH has a stronger intensity. In comparison to the other calculated low-mass object, TMC 1, this model shows stronger intensities by a factor of about 10 for low X-ray fluxes, whereas the intensities are similar for models with $L_X = 10^{32}$ ergs s^{-1} (except CH^+ and SH).

Comparing the models with a protostellar hole to those without one, the stronger X-ray dependency is obvious: For example, the 532.7255 GHz transition of CH shows no variation with the X-ray flux in the two models without a protostellar hole, whereas in the models with a protostellar hole an increasing up to a factor of 16 can be observed. For the three molecules which were identified as observable (CH, CH^+ with the alternative model and NH), the variation covers a range including the intensities of the models without X-ray radiation and therefore additional information is needed to determine the X-ray flux.

TMC 1

As mentioned before, the abundances of all considered molecules are strongly enhanced by X-rays. The integrated line intensity of CH increases by about 2 - 3.5 orders of magnitude, the intensity of CH^+ (according to the chemical model) increases by 5 orders of magnitude and the 841.9973 GHz transition of H_2O^+ even by 7 orders of magnitude. The strongest rise of the intensities is seen for X-ray fluxes L_X between 10^{30} and 10^{32} ergs s^{-1}. For lower fluxes, most molecules are increased only by a factor of 2 - 10. Transitions with upper energies equivalent to above 100 K, however, are increased up to 2 orders of magnitude for $L_X = 0$ to 10^{30} ergs s^{-1}.

Absolute intensities of TMC 1 are about 2 orders of magnitude weaker than for AFGL 2591 for X-ray intensities up to 10^{30} ergs s^{-1} . Compared to IRAS 16293-2422, the integrated intensities are also weaker, besides for the model with chemical age 10^5 years and a protostellar hole, where similar intensities are achieved.

Molecule	Frequency [GHz]	Model 0 [K km s^{-1}]	Model 1 [K km s^{-1}]	Model 2 [K km s^{-1}]	Model 3 [K km s^{-1}]	Model 6 [K km s^{-1}]
CH	532.7255	7.8(-1)	7.8(-1)	8.0(-1)	1.0(0)	9.7(-1)
	536.7627	7.9(-1)	7.9(-1)	8.1(-1)	1.1(0)	9.8(-1)
	1656.9563	3.7(-1)	3.7(-1)	4.5(-1)	2.2(0)	1.6(0)
	1661.1024	3.7(-1)	3.7(-1)	4.5(-1)	2.2(0)	1.6(0)
CH^+	835.079	6.0(-5)	6.0(-5)	6.2(-5)	9.0(-5)	8.9(-5)
	1669.1595	1.3(-5)	1.3(-5)	1.6(-5)	8.4(-5)	1.6(-4)
CH^+	835.079	7.7(-1)	7.8(-1)	8.1(-1)	1.2(0)	1.1(0)
alternat.	1669.1595	1.4(-1)	1.4(-1)	1.8(-1)	1.1(0)	7.7(-1)
NH	946.4758	7.4(-2)	7.1(-2)	7.2(-2)	1.1(-1)	1.0(-1)
	974.4708	2.1(-1)	2.0(-1)	2.1(-1)	3.4(-1)	3.0(-1)
	999.9734	1.7(-1)	1.7(-1)	1.7(-1)	2.8(-1)	2.4(-1)
	1000.0010	6.6(-2)	6.3(-2)	6.4(-2)	1.1(-1)	9.3(-2)
OH^+	909.1588	2.4(-4)	2.4(-4)	2.6(-4)	4.0(-4)	3.6(-4)
	971.8038	1.1(-3)	1.2(-3)	1.2(-3)	2.0(-3)	1.8(-3)
	1033.1186	5.6(-4)	5.6(-4)	6.1(-4)	1.0(-3)	9.2(-4)
	1892.2272	3.2(-5)	3.4(-5)	5.8(-5)	2.9(-4)	2.2(-4)
SH	866.9467	2.3(-4)	1.2(-4)	9.6(-5)	2.2(-4)	2.0(-4)
	875.2671	2.3(-4)	1.2(-4)	9.6(-5)	2.2(-4)	2.0(-4)
	1447.0123	2.0(-3)	1.1(-3)	8.2(-4)	1.7(-3)	1.6(-3)
	1455.1005	2.0(-3)	1.1(-3)	8.2(-4)	1.7(-3)	1.6(-3)
SH^+	526.0480	1.1(-3)	1.2(-3)	1.3(-3)	4.1(-3)	3.4(-3)
	683.4168	6.6(-4)	6.6(-4)	8.4(-4)	3.4(-3)	2.8(-3)
	893.1406	1.1(-4)	1.1(-4)	2.9(-4)	2.9(-3)	2.3(-3)
	1082.9094	7.1(-4)	7.3(-4)	2.1(-3)	2.2(-2)	1.7(-2)
	1230.5673	1.1(-4)	1.2(-4)	3.4(-4)	3.6(-3)	2.8(-3)
	1632.5175	2.5(-4)	3.2(-4)	4.5(-3)	6.4(-2)	4.9(-2)
H_2O^+	607.2582	1.4(-4)	1.4(-4)	1.5(-4)	2.3(-4)	2.1(-4)
	742.0332	3.9(-5)	3.9(-5)	4.3(-5)	8.8(-5)	7.7(-5)
	841.9973	9.7(-10)	3.3(-9)	3.3(-8)	3.4(-7)	4.7(-7)
	1115.0860	1.0(-3)	1.0(-3)	1.1(-3)	1.7(-3)	1.5(-3)
	1139.5152	3.2(-4)	3.2(-4)	3.4(-4)	5.5(-4)	4.9(-4)
	1638.2007	1.1(-4)	1.1(-4)	1.4(-4)	4.3(-4)	3.6(-4)

Table 10: Integrated line intensities $\int T_{mb}\, dv$ of AFGL 2591.

Molecule	Frequency [GHz]	$L_X = 0$ [K km s^{-1}]	$L_X = 10^{28}$ [K km s^{-1}]	$L_X = 10^{30}$ [K km s^{-1}]	$L_X = 10^{32}$ [K km s^{-1}]
CH	532.7255	2.6(-2)	2.6(-2)	2.6(-2)	2.6(-2)
	536.7627	2.6(-2)	2.6(-2)	2.6(-2)	2.6(-2)
	1656.9563	3.4(-3)	3.4(-3)	3.5(-3)	6.1(-3)
	1661.1024	3.3(-3)	3.3(-3)	3.4(-3)	6.0(-3)
CH^+	835.079	2.3(-8)	2.3(-8)	2.3(-8)	3.7(-8)
	1669.1595	7.0(-9)	7.0(-9)	8.4(-9)	1.2(-7)
CH^+	835.079	2.0(-2)	2.0(-2)	2.0(-2)	2.0(-2)
alternat.	1669.1595	1.1(-3)	1.1(-3)	1.2(-3)	2.4(-3)
NH	946.4758	1.8(-1)	1.8(-1)	1.9(-1)	2.1(-1)
	974.4708	4.4(-1)	4.3(-1)	4.7(-1)	5.3(-1)
	999.9734	3.5(-1)	3.5(-1)	3.8(-1)	4.3(-1)
	1000.0010	1.3(-1)	1.3(-1)	1.5(-1)	1.7(-1)
OH^+	909.1588	3.5(-4)	3.5(-4)	3.5(-4)	3.7(-4)
	971.8038	1.5(-3)	1.5(-3)	1.5(-3)	1.5(-3)
	1033.1186	7.0(-4)	7.0(-4)	7.0(-4)	7.4(-4)
	1892.2272	1.4(-5)	1.4(-5)	1.4(-5)	5.2(-5)
SH	866.9467	2.1(-6)	4.0(-6)	2.1(-5)	2.7(-7)
	875.2671	2.1(-6)	4.0(-6)	2.1(-5)	2.7(-7)
	1447.0123	1.7(-5)	3.2(-5)	1.7(-4)	2.2(-6)
	1455.1005	1.7(-5)	3.2(-5)	1.7(-4)	2.2(-6)
SH^+	526.0480	3.8(-5)	3.8(-5)	3.8(-5)	3.9(-5)
	683.4168	1.7(-5)	1.7(-5)	1.7(-5)	1.8(-5)
	893.1406	1.2(-6)	1.2(-6)	1.2(-6)	1.9(-6)
	1082.9094	6.2(-6)	6.2(-6)	6.2(-6)	1.2(-5)
	1230.5673	9.3(-7)	9.3(-7)	9.4(-7)	1.8(-6)
	1632.5175	3.4(-7)	3.4(-7)	5.0(-7)	1.9(-5)
H_2O^+	607.2582	1.9(-4)	1.9(-4)	1.9(-4)	2.0(-4)
	742.0332	3.6(-5)	3.6(-5)	3.6(-5)	3.9(-5)
	841.9973	5.4(-11)	6.4(-11)	1.1(-9)	1.4(-7)
	1115.0860	9.6(-4)	9.6(-4)	9.6(-4)	1.0(-3)
	1139.5152	2.8(-4)	2.8(-4)	2.8(-4)	2.9(-4)
	1638.2007	5.1(-5)	5.1(-5)	5.1(-5)	7.6(-5)

Table 11: Integrated line intensities $\int T_{mb}\, dv$ of IRAS 16293-2422. The chemical age of the model was 10^5 years.

Molecule	Frequency [GHz]	$L_X = 0$ [K km s^{-1}]	$L_X = 10^{28}$ [K km s^{-1}]	$L_X = 10^{30}$ [K km s^{-1}]	$L_X = 10^{32}$ [K km s^{-1}]
CH	532.7255	6.4(-3)	6.4(-3)	6.6(-3)	1.1(-1)
	536.7627	6.5(-3)	6.5(-3)	6.7(-3)	1.1(-1)
	1656.9563	2.0(-3)	2.0(-3)	4.1(-3)	8.6(-1)
	1661.1024	1.9(-3)	1.9(-3)	4.1(-3)	8.6(-1)
CH^+	835.079	1.9(-8)	1.9(-8)	2.3(-8)	8.7(-6)
	1669.1595	5.1(-9)	5.1(-9)	9.8(-9)	1.6(-5)
CH^+	835.079	6.9(-3)	6.9(-3)	7.4(-3)	2.4(-1)
alternat.	1669.1595	6.4(-4)	6.4(-4)	1.6(-3)	3.8(-1)
NH	946.4758	7.6(-2)	7.6(-2)	9.2(-2)	9.0(-1)
	974.4708	2.0(-1)	2.0(-1)	2.5(-1)	2.6(0)
	999.9734	1.6(-1)	1.6(-1)	2.0(-1)	2.2(0)
	1000.0010	6.1(-2)	6.1(-2)	7.8(-2)	8.7(-1)
OH^+	909.1588	1.5(-4)	1.5(-4)	1.6(-4)	8.8(-4)
	971.8038	6.8(-4)	6.8(-4)	7.1(-4)	4.8(-3)
	1033.1186	3.3(-4)	3.3(-4)	3.5(-4)	2.5(-3)
	1892.2272	6.9(-6)	6.9(-6)	8.9(-6)	4.3(-4)
SH	866.9467	9.0(-15)	1.1(-14)	2.3(-12)	9.6(-10)
	875.2671	8.9(-15)	1.1(-14)	2.3(-12)	9.5(-10)
	1447.0123	1.2(-14)	1.6(-14)	4.0(-12)	1.6(-9)
	1455.1005	1.2(-14)	1.5(-14)	3.9(-12)	1.6(-9)
SH^+	526.0480	7.2(-6)	7.2(-6)	7.8(-6)	3.8(-4)
	683.4168	4.0(-6)	4.0(-6)	4.4(-6)	3.0(-4)
	893.1406	5.2(-7)	5.2(-7)	6.5(-7)	1.3(-4)
	1082.9094	3.0(-6)	3.0(-6)	4.0(-6)	9.4(-4)
	1230.5673	4.7(-7)	4.7(-7)	6.3(-7)	1.6(-4)
	1632.5175	2.3(-7)	2.4(-7)	7.7(-7)	6.0(-4)
H_2O^+	607.2582	7.7(-5)	7.7(-5)	7.9(-5)	5.1(-4)
	742.0332	1.8(-5)	1.8(-5)	1.9(-5)	2.4(-4)
	841.9973	4.1(-13)	4.2(-13)	1.9(-12)	3.5(-10)
	1115.0860	4.6(-4)	4.6(-4)	4.8(-4)	4.0(-3)
	1139.5152	1.4(-4)	1.4(-4)	1.5(-4)	1.4(-3)
	1638.2007	3.1(-5)	3.1(-5)	3.5(-5)	1.3(-3)

Table 12: Integrated line intensities $\int T_{mb}\, dv$ of IRAS 16293-2422. The chemical age of the model was 10^5 years and a protostellar hole was assumed.

Molecule	Frequency [GHz]	$L_X = 0$ [K km s^{-1}]	$L_X = 10^{28}$ [K km s^{-1}]	$L_X = 10^{30}$ [K km s^{-1}]	$L_X = 10^{32}$ [K km s^{-1}]
CH	532.7255	6.2(-2)	6.2(-2)	6.2(-2)	6.2(-2)
	536.7627	6.3(-2)	6.3(-2)	6.3(-2)	6.3(-2)
	1656.9563	2.8(-2)	2.8(-2)	2.9(-2)	2.5(-2)
	1661.1024	2.8(-2)	2.8(-2)	2.8(-2)	2.4(-2)
CH^+	835.079	1.0(-7)	1.0(-7)	1.0(-7)	1.2(-7)
	1669.1595	2.5(-8)	2.5(-8)	2.6(-8)	1.4(-7)
CH^+	835.079	5.6(-2)	5.6(-2)	5.6(-2)	5.6(-2)
alternat.	1669.1595	1.1(-2)	1.1(-2)	1.1(-2)	9.2(-3)
NH	946.4758	8.3(-2)	8.3(-2)	9.5(-2)	8.5(-2)
	974.4708	2.1(-1)	2.1(-1)	2.5(-1)	2.2(-1)
	999.9734	1.7(-1)	1.7(-1)	2.1(-1)	1.8(-1)
	1000.0010	6.6(-2)	6.6(-2)	7.9(-2)	6.8(-2)
OH^+	909.1588	6.0(-4)	6.0(-4)	6.0(-4)	6.3(-4)
	971.8038	2.5(-3)	2.5(-3)	2.5(-3)	2.6(-3)
	1033.1186	1.2(-3)	1.2(-3)	1.2(-3)	1.3(-3)
	1892.2272	2.0(-5)	2.0(-5)	2.0(-5)	6.5(-5)
SH	866.9467	5.4(-6)	4.1(-6)	2.0(-5)	2.7(-7)
	875.2671	5.4(-6)	4.1(-6)	2.0(-5)	2.7(-7)
	1447.0123	4.3(-5)	3.3(-5)	1.6(-4)	2.2(-6)
	1455.1005	4.3(-5)	3.3(-5)	1.6(-4)	2.2(-6)
SH^+	526.0480	1.2(-3)	1.2(-3)	1.2(-3)	1.2(-3)
	683.4168	5.3(-4)	5.3(-4)	5.3(-4)	5.3(-4)
	893.1406	3.9(-5)	3.9(-5)	3.9(-5)	3.9(-5)
	1082.9094	2.0(-4)	2.0(-4)	2.0(-4)	2.1(-4)
	1230.5673	3.0(-5)	3.0(-5)	3.0(-5)	3.1(-5)
	1632.5175	6.5(-6)	6.5(-6)	6.7(-6)	2.5(-5)
H_2O^+	607.2582	4.5(-4)	4.5(-4)	4.5(-4)	4.7(-4)
	742.0332	8.1(-5)	8.1(-5)	8.2(-5)	8.9(-5)
	841.9973	8.5(-11)	9.5(-11)	1.1(-9)	1.4(-7)
	1115.0860	2.2(-3)	2.2(-3)	2.2(-3)	2.3(-3)
	1139.5152	6.5(-4)	6.5(-4)	6.5(-4)	6.9(-4)
	1638.2007	1.1(-4)	1.1(-4)	1.1(-4)	1.5(-4)

Table 13: Integrated line intensities $\int T_{mb}\, dv$ of IRAS 16293-2422. The chemical age of the model was 10^4 years.

Molecule	Frequency [GHz]	$L_X = 0$ [K km s^{-1}]	$L_X = 10^{28}$ [K km s^{-1}]	$L_X = 10^{30}$ [K km s^{-1}]	$L_X = 10^{32}$ [K km s^{-1}]
CH	532.7255	2.0(-2)	2.0(-2)	2.0(-2)	1.4(-1)
	536.7627	2.0(-2)	2.0(-2)	2.0(-2)	1.4(-1)
	1656.9563	1.5(-2)	1.5(-2)	1.5(-2)	8.6(-1)
	1661.1024	1.5(-2)	1.5(-2)	1.5(-2)	8.6(-1)
CH^+	835.079	9.3(-8)	9.3(-8)	9.9(-8)	8.8(-6)
	1669.1595	2.2(-8)	2.2(-8)	2.8(-8)	1.6(-5)
CH^+	835.079	2.5(-2)	2.5(-2)	2.5(-2)	2.6(-1)
alternat.	1669.1595	5.4(-3)	5.3(-3)	5.3(-3)	3.8(-1)
NH	946.4758	3.2(-2)	3.2(-2)	3.9(-2)	6.3(-1)
	974.4708	8.5(-2)	8.5(-2)	1.1(-1)	1.9(0)
	999.9734	6.9(-2)	6.9(-2)	8.8(-2)	1.6(0)
	1000.0010	2.6(-2)	2.6(-2)	3.3(-2)	6.4(-1)
OH^+	909.1588	2.5(-4)	2.5(-4)	2.6(-4)	1.1(-3)
	971.8038	1.1(-3)	1.1(-3)	1.2(-3)	6.0(-3)
	1033.1186	5.5(-4)	5.5(-4)	5.8(-4)	3.1(-3)
	1892.2272	1.0(-5)	1.0(-5)	1.4(-5)	4.4(-4)
SH	866.9467	5.1(-14)	5.5(-14)	1.9(-12)	9.6(-10)
	875.2671	5.0(-14)	5.4(-14)	1.9(-12)	9.5(-10)
	1447.0123	6.5(-14)	7.3(-14)	3.4(-12)	1.6(-9)
	1455.1005	6.3(-14)	7.1(-14)	3.3(-12)	1.6(-9)
SH^+	526.0480	3.1(-4)	3.1(-4)	3.1(-4)	5.8(-4)
	683.4168	1.7(-4)	1.7(-4)	1.7(-4)	4.1(-4)
	893.1406	1.9(-5)	1.9(-5)	1.9(-5)	1.4(-4)
	1082.9094	1.1(-4)	1.1(-4)	1.1(-4)	1.0(-3)
	1230.5673	1.7(-5)	1.7(-5)	1.7(-5)	1.7(-4)
	1632.5175	5.7(-6)	5.7(-6)	6.4(-6)	6.0(-4)
H_2O^+	607.2582	1.8(-4)	1.8(-4)	1.8(-4)	7.1(-4)
	742.0332	4.0(-5)	4.0(-5)	4.3(-5)	2.9(-4)
	841.9973	7.8(-13)	8.3(-13)	3.2(-12)	3.5(-10)
	1115.0860	1.0(-3)	1.0(-3)	1.1(-3)	5.3(-3)
	1139.5152	3.2(-4)	3.2(-4)	3.3(-4)	1.8(-3)
	1638.2007	6.3(-5)	6.3(-5)	7.6(-5)	1.4(-3)

Table 14: Integrated line intensities $\int T_{mb}\, dv$ of IRAS 16293-2422. The chemical age of the model was 10^4 years and a protostellar hole was assumed.

Molecule	Frequency [GHz]	$L_X = 0$ [K km s^{-1}]	$L_X = 10^{28}$ [K km s^{-1}]	$L_X = 10^{30}$ [K km s^{-1}]	$L_X = 10^{32}$ [K km s^{-1}]
CH	532.7255	4.1(-3)	4.1(-3)	7.5(-3)	7.6(-1)
	536.7627	4.1(-3)	4.1(-3)	7.6(-3)	7.7(-1)
	1656.9563	4.4(-4)	4.4(-4)	1.2(-2)	1.5(0)
	1661.1024	4.4(-4)	4.3(-4)	1.2(-2)	1.5(0)
CH^+	835.079	2.4(-7)	2.4(-7)	4.3(-7)	3.3(-4)
	1669.1595	4.0(-9)	4.2(-9)	3.2(-7)	5.6(-4)
CH^+	835.079	3.5(-3)	3.5(-3)	8.3(-3)	1.1(0)
alternat.	1669.1595	1.3(-4)	1.3(-4)	5.4(-3)	8.2(-1)
NH	946.4758	8.2(-4)	8.8(-4)	7.0(-3)	4.9(-1)
	974.4708	2.3(-3)	2.5(-3)	2.2(-2)	1.4(0)
	999.9734	1.8(-3)	2.0(-3)	1.8(-2)	1.1(0)
	1000.0010	7.0(-4)	7.5(-4)	6.9(-3)	4.9(-1)
OH^+	909.1588	6.7(-6)	6.8(-6)	2.0(-5)	1.4(-3)
	971.8038	3.0(-5)	3.1(-5)	1.0(-4)	7.9(-3)
	1033.1186	1.4(-5)	1.5(-5)	4.9(-5)	4.0(-3)
	1892.2272	1.4(-7)	1.9(-7)	6.6(-6)	7.6(-4)
SH	866.9467	1.5(-11)	2.1(-11)	1.1(-8)	1.5(-8)
	875.2671	1.6(-11)	2.1(-11)	1.1(-8)	1.5(-8)
	1447.0123	1.1(-10)	1.5(-10)	7.8(-8)	9.2(-8)
	1455.1005	1.1(-10)	1.5(-10)	7.8(-8)	9.2(-8)
SH^+	526.0480	2.3(-5)	2.4(-5)	3.4(-5)	5.2(-4)
	683.4168	1.2(-5)	1.2(-5)	1.9(-5)	3.3(-4)
	893.1406	7.3(-7)	7.3(-7)	2.5(-6)	6.8(-5)
	1082.9094	4.4(-6)	4.4(-6)	1.7(-5)	4.8(-4)
	1230.5673	7.2(-7)	7.3(-7)	2.9(-6)	8.1(-5)
	1632.5175	1.6(-7)	1.7(-7)	1.2(-5)	1.8(-4)
H_2O^+	607.2582	3.4(-6)	3.5(-6)	1.0(-5)	8.3(-4)
	742.0332	5.7(-7)	6.0(-7)	3.3(-6)	3.5(-4)
	841.9973	3.4(-14)	3.2(-11)	4.9(-9)	5.1(-7)
	1115.0860	2.7(-5)	2.8(-5)	8.8(-5)	7.3(-3)
	1139.5152	8.4(-6)	8.7(-6)	2.9(-5)	2.5(-3)
	1638.2007	1.1(-6)	1.3(-6)	1.5(-5)	1.9(-3)

Table 15: Integrated line intensities $\int T_{mb}\, dv$ of TMC 1.

6 Observations

In the second part of the work, observations of star forming regions were carried out. For our measurements with the KOSMA radio telescope, we have chosen the massive star formation areas W3 and S140. Unfortunately, we got our observation time in the last quarter of the four month diploma thesis and therefore not much time was left to do a thoroughly analyze of the obtained data. In a first section, we will give a brief introduction to the telescope and refer to Kramer et al. (2000) and the homepage of KOSMA[21] for further information. Then, we will present a simple chemical network in order to determine the cosmic ray ionization rate from HCO^+ observations. Afterwards, we will present the results our observations of S140 and W3.

The KOSMA Telescope

The KOSMA (Kölner Observatorium für Submillimeter Astronomie - The Cologne Obsevatory for Submillimeter Astronomy) telescope is located on Gornergrat at 3089 m above sealevel, near Zermatt (Switzerland). It is operated by the I. Physikalisches Institut (University of Cologne) and the Radioastronomisches Institut (University of Bonn) and administrated by the Stiftung Hochalpine Forschungsstation Gornergrat und Jungfraujoch (Bern). The location in the high alps is ideal for observations in millimeter and submillimeter wavelengths due to very good atmospherical conditions. Crucial for measurements at these frequencies is a low atmospherical water column density above the telescope. In winter time, conditions are sometimes good enough to make measurements at a frequency of 820 GHz.

The telescope is built in the Cassegrain design with a 3 m diameter main mirror and a 27 cm subreflector, which can be aligned up to ±3' (on the sky). This so-called wobbler mechanism is used for the later discussed beam switching measuring mode. The telescope has a pointing accuracy of ±10" which can be checked by a measurement of a strong point-like radio source like Mars or Jupiter. The observation instruments are located in the two focii on the side of the elevation axis (Nasmyth-focus). Dual-channel-SIS (Superconductor-Isolator-Superconductor) receiver are operated in conjunction with acusto-optical spectrometers (AOS). The incoming signal is mixed in the receiver with the frequency of a local oscillator to a lower frequency that might be amplified before being analysed by the spectrometers. Five receivers cover all atmospheric windows from 210 - 820 GHz. The spectrometers cover a bandwidth of 1 GHz and have a resolution of approximately 0.5 MHz. For the calibration, a hot and cold load (superfluid nitrogen) are used.

Observation in different modes can be carried out. We will only discuss the later used modes and refer to Brémaud (2002):

Position switching: The source (called "on"-position) and a position without emission in the considered frequency range ("off"-position) are measured alternately to determine the atmospherical disturbance. Since the conditions and the receiver parameters do not stay constant in time, the off-measurement has to be repeated after a certain time. To achieve a good signal-to-noise ratio, the integration time has to be chosen as long as the off-source measurement is: After an initial decreasing of the noise level as described by the radiometer equation (107), before the drift of the receiver and the change of atmospherical conditions take overhand and the noise level increases again. The point of the minima can be determined using the Allan-variance (e.g. Bruderer 2004).

Raster mapping: This observation mode is similar to the position switching mode, but more than one on-position is measured after an off-measurement. Typically 3 to 5 on-measurements are taken and then calibrated by the same off-measurement. The calibrated system stays stable for a certain time and the total on-source measurement should not exceed this time limit. To achieve an optimized signal-to-noise ration for n on-source measurements, the off-position integration time should be $\sqrt{n}$ times longer than the on-source time,

$$t_{off} = \sqrt{n} \cdot t_{on} \ . \tag{108}$$

[21] http://www.ph1.uni-koeln.de/gg/

Beam switching: For small sources, the longsome moving of the telescope can be replaced by the faster alignment of the subreflector, avoiding the so-called deadtimes, when the telescope is moving. Thus, the integration time can be chosen shorter and a better calibration is achieved.

On-the-fly (OTF): The telescope is moved continously along a line for this measuring mode. One off-position is used to calibrate the measurement of the whole line. For an optimal signal-to-noise ratio, the relation in Eq. (108) between the on-time t_{on} and the off-time t_{off} should be fulfilled: The number of measurements n corresponds to the extracted on-positions of the continously measured line. If we plug this equation into the total measuring time

$$t_{OTF} = n \cdot t_{on} + t_{off} \tag{109}$$

and compare t_{on} with the optimal on-source integration time of a position switching measurement, we can estimate a gain of time up to a factor of 4! Another important point in on-the-fly measurements is the smoothed out observation due to the movement of the telescope. The beam width is therefore enlarged in this direction. The loss in resolution is however only about 1 % to 4 %, depending on the beam size (Beuther 1999).

Observations

The observations were obtained between 6^{th} and 13^{th} of February 2006. The weather conditions were good but due to problems with the chopper, the "beam switching" mode was not available. This problem has also affected the point accuracy, since the subreflector was in a undefined position. Pointing checks, previous to our measurement however have shown no deviation. In our observation time, two receivers for frequencies between 210 and 270 GHz and 330 and 365 GHz were operating.

Out of the in Sect. 5 discussed molecules, only lines for SH^+ and H_2O^+ were found in the observable frequency range. The two lines of SH^+ at 345.843 ± 0.003 GHz and 345.930 ± 0.003 GHz have Einstein-A-Coefficents of the order 10^{-4} s^{-1} and upper level energies equivalent to 16 K. Due to the low abundance of the molecules, a detection seemed to be unpromising tough. We have found 20 lines of H_2O^+ in the range of the KOSMA receivers. Unfortunately, the Einstein-A-Coefficents for this transitions are below $2 \cdot 10^{-5}$ s^{-1} and they have a too high upper level energy (above 420 K) to get excited in the environment of YSOs. We have therefore chosen another X-ray sensitive molecule, the formyl cation HCO^+ for our measurements. The $J = 4 \rightarrow 3$ transition of HCO^+ has a frequency of 356.734 GHz and the $J = 3 \rightarrow 2$ line lays at 267.557 GHz. Since the two lines fit the frequency range of different receivers, they can be observed simultaneously. In addition to the HCO^+ transitions, we had the possibility to measure the $J = 2 \rightarrow 1$ line of ^{13}CO at 220.399 GHz and the $J = 3 \rightarrow 2$ line of CO at 345.796. Einstein-A-Coefficents and upper level energies for the observed lines are given in Tab. 16.

Transition	Frequency [GHz]	Einstein-A [s^{-1}]	E_{up} [K]	Beam [arcsec]	Beam eff. %
HCO^+(3-2)	267.557	$1.48 \cdot 10^{-3}$	25.68	130	68
HCO^+(4-3)	356.734	$3.63 \cdot 10^{-3}$	42.8	82	70
^{13}CO(2-1)	220.399	$6.07 \cdot 10^{-7}$	15.87	130	68
CO(3-2)	345.796	$2.50 \cdot 10^{-6}$	33.19	82	70

Table 16: Observed transitions: KOSMA beam efficiencies and half power beamdiths can be found at http://www.ph1.uni-koeln.de/gg/. The molecular data were obtained from the Leiden Atomic and Molecular Database LAMDA (Schöier et al. 2005).

The telescope was operated in the raster mapping mode for the measurement of a cut through S140 and in the on-the-fly mode for all maps. The off-position measurements were always carried

out at (-10'/-10') relative to the center (0'/0') of the sources. As center point for the observation of S140, we have chosen the infrared source 1 (IRS1) at $\alpha_{1950} = 22^h\,17^m\,41^s$ and $\delta_{1950} = 63°3'\,40''$. The measurements of W3 were carried out around $\alpha_{2000} = 2^h\,25^m\,37.8^s$ and $\delta_{2000} = 62°5'\,52''$ centering the infrared source IRS3a. A map of both HCO^+ transitions with a resolution 0.5' covering an area of 10' × 10' was obtained for S140. These maps were measured 19 times, each taking about 50 minutes. The recording of the maps for W3 were also perfomed for both transitions of HCO^+, for the CO(3-2) transition and the ^{13}CO(2-1) transition. An angular resolution of 0.5' and a size of 6' × 6' were chosen after a first observation of a 10' × 10' map. The observation of the HCO^+ maps was repeated 9 times, whereas the map for CO and ^{13}CO were recorded 6 times. Each measurement lasted 25 minutes. For the raster mapping observations of S140, three on-source measurements with an integration time of 20 s were obtained and calibrated with one off-source measurement of 30 s.

Reduction of Data

The data were reduced using the Gildas package[22]. The recorded spectra are already calibrated by KOSMA and the atmospheric attenuation is taken into account. The so achieved antenna temperature T_A^* was then calibrated to the correct main-beam brightness temperature T_{mb} by

$$T_{mb} = \frac{F_{eff}}{B_{eff}} \cdot T_A^* \ , \tag{110}$$

with a forward efficiency F_{eff} of 90 % and beam efficiancy B_{eff} as given in Tab. 16 for each line.

Some of the recorded spectra have shown only noise at positions where for most recorded spectra lines were clearly visible. We have found no relation between the recorded header-parameters (e.g. T_{rms}, H_2O column density, Elevation or T_{sys}) and the occurrence of such empty spectra. Pointing errors can be considered as unlikely, since the driving program marks spectra, if the telescope is not tracking the target properly.

A statistical criterion was applied to filter out bad spectra: For every position on a map, all recorded spectra were checked for a line exceeding[23] $3 \cdot T_{rms}$. If more than half of the spectra showed such a line, the spectra without lines have been removed for this position. The method does only work for points with a strong intensity, mostly close to the center. For S140, Fig. 32 indicates positions in red, where the test was applicable. Out of the totally 441 points (21 × 21), 17 % of the HCO^+(3-2) spectra were removed at 62 positions and 25 % of the HCO^+(4-3) spectra at 21 positions. Points with a $3 \cdot T_{rms}$ line which is only observable after averaging several spectra are indicated in the same figure by green color. Such points are however critical for an accurate determination of line intensities. A test at the (-1.5'/-2') position of S140 has shown an integrated line intensity for the HCO^+(3-2) transition between 0.2 and 1 K km s^{-1} depending on the selection of the lines.

After the bad spectra have been removed, a baseline of the order 1 was subtracted and all spectra for a point were averaged. The line window for this processing were -16 to 2 km s^{-1} for S140 and -55 to -25 km s^{-1} for W3.

[22] http://iram.fr/IRAMFR/GILDAS/

[23] We use in this section the threshold $3 \cdot T_{rms}$, a $3 \cdot T_\sigma$ value would however deliver similar results, since the definition for $1 \cdot \sigma$ is $1.3\sqrt{\Delta\nu\Delta v} \cdot T_{rms}$, with $\Delta\nu$ the channel width, Δv the estimated line width and a factor 1.3 including a 30 % calibration uncertainty (Jørgensen et al. 2004). With $\Delta\nu = 0.28$ km s^{-1} for KOSMA and $\Delta v \approx 3$ km s^{-1} (c.f. Tab.20), we obtain $T_\sigma \approx 1.2 \cdot T_{rms}$.

6.1 Formation of HCO^+

The formyl cation HCO^+ is a highly reactive molecule, that cannot exist under terrestrial conditions (Ewald 1986). It is suitable as X-ray tracer, since X-rays enhance its abundance more than UV radiation (Stäuber et al. 2005a). In our work we will however try to estimate the cosmic ray ionization rate ζ [s^{-1}] rather than the X-ray luminosity. The comprehensive chemical network of Sect. 5 is replaced by a simple network that only consists of the most important reactions for HCO^+ (Jørgensen et al. 2004):

The starting point to form HCO^+ is the production of H_3^+, which is mainly formed through the ionization of H_2 by cosmic rays (c.r.)

$$\begin{aligned} H_2 + \text{c.r.} &\rightarrow H_2^+ + e^- && (111)\\ H_2^+ + H_2 &\rightarrow H_3^+ + H \ . && (112) \end{aligned}$$

Due to the high abundance of H_2, we will assume that each H_2^+ immediately reacts with H_2 and forms H_3^+. The rate equation of this reaction is therefore

$$\zeta \cdot n(H_2) = \frac{dn(H_3^+)}{dt} \ , \tag{113}$$

where n(A) denotes the density of the molecule A. The dominant mechanism for the formation of HCO^+ is

$$H_3^+ + CO \rightarrow HCO^+ + H_2 \ . \tag{114}$$

For temperatures above 100 K, HCO^+ is mainly destroyed by reactions with water and therefore also important in the chemical network of water (Stäuber et al. 2005b). In the observed region, the temperature is presumably lower and electron recombination is the most important reaction for the destruction of HCO^+. We will therefore take only the reaction

$$HCO^+ + e^- \rightarrow CO + H \tag{115}$$

into account. We introduce the rate coefficient k_{HCO^+} and k_{CO} for the forming and destructing reaction. The rate equations can then be equated, leading to

$$k_{HCO^+} \cdot n(H_3^+) \cdot n(CO) = k_{CO} \cdot n(HCO^+) \cdot n(e) \ , \tag{116}$$

with the electron density n(e). Assuming a standard fractional abundance of CO (10^{-4}), the main removal mechanism for H_3^+ is through the forming of HCO^+. The rate of the destruction of H_3^+ is therefore equal to the formation rate of HCO^+:

$$\zeta \cdot n(H_2) = k_{HCO^+} \cdot n(H_3^+) \cdot n(CO) \tag{117}$$

We can rewrite the equations (116) and (117) to an expression for the cosmic ray ionization rate ζ [s^{-1}] :

$$\zeta = k_{CO} \cdot \frac{n(HCO^+) \cdot n(e)}{n(H_2)} \tag{118}$$

The rate coefficient k_{CO} can be obtained from the UMIST database (Millar et al. 1997)

$$k_{CO} = 2.4 \cdot 10^7 \cdot \left(\frac{T}{300}\right)^{-0.69} \ , \tag{119}$$

with the kinetic temperature T [K]. Therefore, the electron density, the densities of HCO^+ and H_2 and the gas temperature (for k_{CO}) have to be obtained from measurements.

6.2 Observations of S140

S140 is a HII region located at the south-east edge of the L1202 cloud in the Cepheus constellation, at a distance of approximately 900 pc (Stäuber 2003). The region is illuminated from the south-western side by the B0V star HD211880. The cloud extends over more than 30' (8 pc) and is partly so opaque, that it completely blocks the view to stars behind it. Clouds like this are therefore called "dark clouds".

S140 contains a small cluster with three highly obscured infrared sources, that are optically invisible (Preibisch et al. 2002 and references therein). The brightest source is called IRS 1 and will be the center point for our observations. The two other sources IRS 2 and IRS 3 lay 17" in the north and 9" in the east of IRS 1. Observations in the infrared show, that these sources are deeply embedded Young Stellar Objects associated with circumstellar material. The luminosities of IRS 1, 2 and 3 are estimated to be $5 \cdot 10^3$ $L_\odot$, $3 \cdot 10^3$ $L_\odot$ and $2 \cdot 10^3$ $L_\odot$ respectively, leading to stellar masses between 6 and 10 $M_\odot$.

The Young Stellar Objects in S140 are the source of strong molecular outflows. A strong bipolar CO outflow is detected. IRS1 lies exactly in the middle between blue- and red-shifted outflow and can therefore be considered as the source of the outflow. Another promintent feature of S140 is its photon dominated region (PDR), where FUV photons with energy between 6 eV and 13.6 eV control the heating and chemical processes. The border between ionized and unionized species, called ionization front, is also within the PDR (c.f. Fig. 4). The PDR and the ionization front is visible in optical wavelengths by the recombination line of HII: The $J = 3 \rightarrow 2$ transition produces so-called H_α photons with a wavelength of 656 nm, in the red part of the visible spectra.

Large scale maps in ^{12}CO and ^{13}CO for a first orientation and deeper introductions to this object are given in Stäuber (2003) and Brémaud (2002).

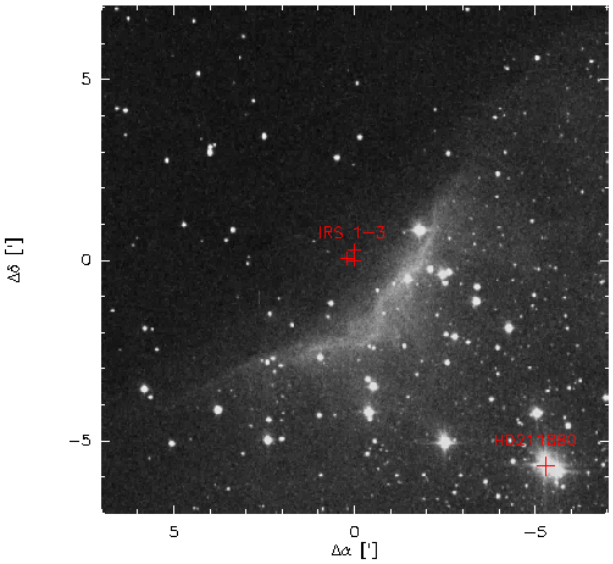

Figure 24: An optical image of S140. Only the red glowing HII region and the illuminating B0V star HD 211880 are visible in optical wavelengths.

6.2.1 Maps of S140

The maps of the integrated intensity of HCO^+ are presente in Fig. 26 for the $J = 3 \rightarrow 2$ transition and in Fig. 27 for the $J = 4 \rightarrow 3$ transition. Both have been oversampled from 21 × 21 measured positions to 42 × 42 points. Equidistant conture levels from 2 to to maximum, in steps of 2 K km s^{-1}, are plotted. Additionally, the half maximum conture level is indicated by a red line. Two further maps are presented with a stretched data axis (Fig. 28 and 29). In order to identify a position with a single spectra (c.f. Appendix B), these maps have not been oversampled and seem therefore coarse-grained. The data obtained from the on-the-fly measurement are combined with the data from the raster mapping measurement.

In contrast to maps of ^{12}CO (Stäuber 2003), the emission of HCO^+ is very strongly concentrated around the center position. The extensions to the north-east, as observed in CO, can only be suspected. The emission of HCO^+(4-3) is more concentrated than those of HCO^+(3-2) due to the fact that the upper level of this transition needs a higher temperature to get populated. The concentration of higher-J-transitions to the center has also been observed by Stäuber (2003) in comparing the ^{12}CO(7-6) with the ^{12}CO(2-1) line.

The T_{rms} of the maps is very low, since the measurements were repeated several times. The average T_{rms} for the HCO^+(4-3) map with 0.08 K is about 2 times higher than for the HCO^+(3-2) map with 0.2 K. This is possibly due to the higher system temperature at higher frequency (c.f. the system temperature of HIFI, Sect. 5.6). The map of the $J = 4 \rightarrow 3$ transition shows structures that are likely to be not real: The two vertical lines at $\Delta\delta$ = -1.5' and $\Delta\delta$ = 2' are suspected to be artefacts. Since the lines lie in the direction of the scanning, a problem with the on-the-fly observation mode could be a reason. On the "overexposed" maps, the situation is even more prominent: Points with negative integrated intensity are given in black. For the HCO^+(3-2) map, such points can generally be found near the border of the map, as expected. For the HCO^+(4-3) map, however, many positions without a detected line (c.f. Fig. 32) lie close to the center in an irregular distribution. Some points, seperated from the center, were found with an integrated intensity above 1.5 K km s−1 (e.g. the two points at $\Delta\alpha$ = -4' and $\Delta\delta$ = -1.5' & 2'). A possible reason is the very bad baseline for the spectra recorded with this receiver (330 - 365 GHz). In addition, strange lines that do not always occure at the same position were found (c.f. Fig. 25). Improper off-measurements can be excluded, since their position was fixed to a coordinate for the whole map.

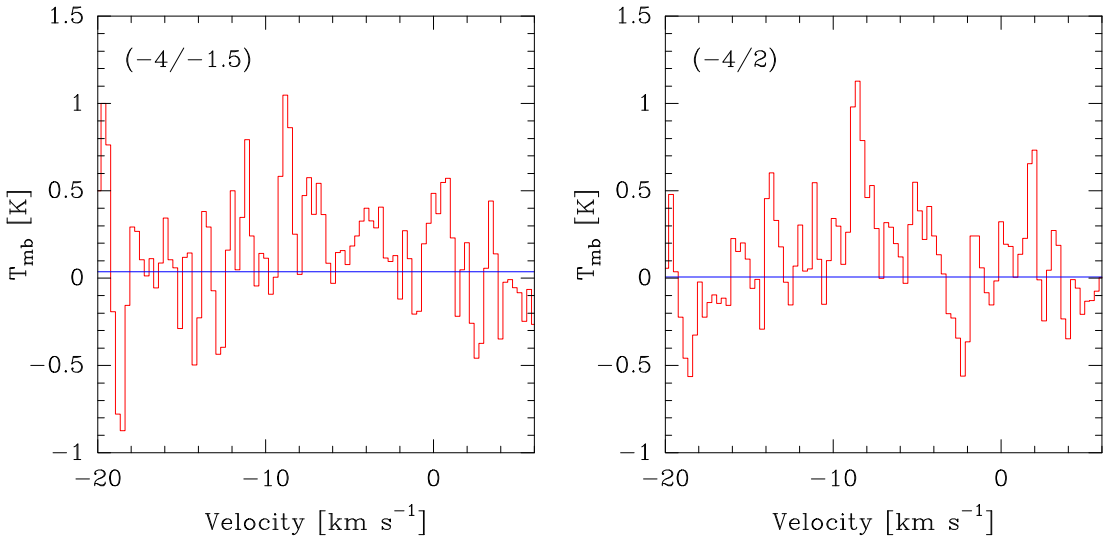

Figure 25: Map of the recorded spectra for HCO^+(4-3) of S140 at an offset of (-1.5'/-2') relative to the center ($\alpha_{1950} = 22^h\,17^m\,41^s$ and $\delta_{1950} = 63°3'\,40''$). A baseline of order 0 is plotted in blue.

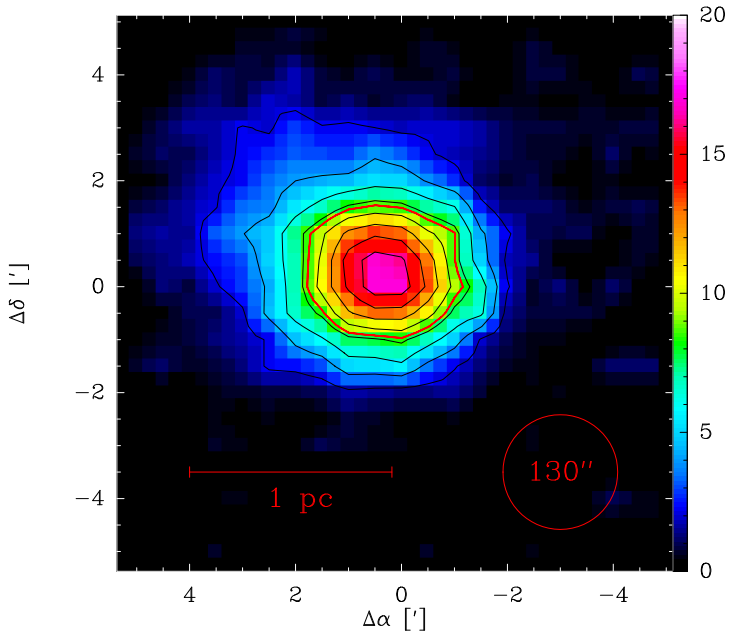

Figure 26: Map of the HCO^+(3-2) integrated intensity [K km s^{-1}] for S140, integrated from $v = -14$ to 0 $km\,s^{-1}$. The coordinates are relative to $\alpha_{1950} = 22^h\,17^m\,41^s$ and $\delta_{1950} = 63°3'\,40''$. Conture levels are from 2 K km s^{-1} to 18 K km s^{-1} in steps of 2 K km s^{-1}. The bold red conture level is to the value 8.65 K. The peak value is 17.29 K km s^{-1} at the offset (0.5'/0') and the average T_{rms} is 0.08 K.

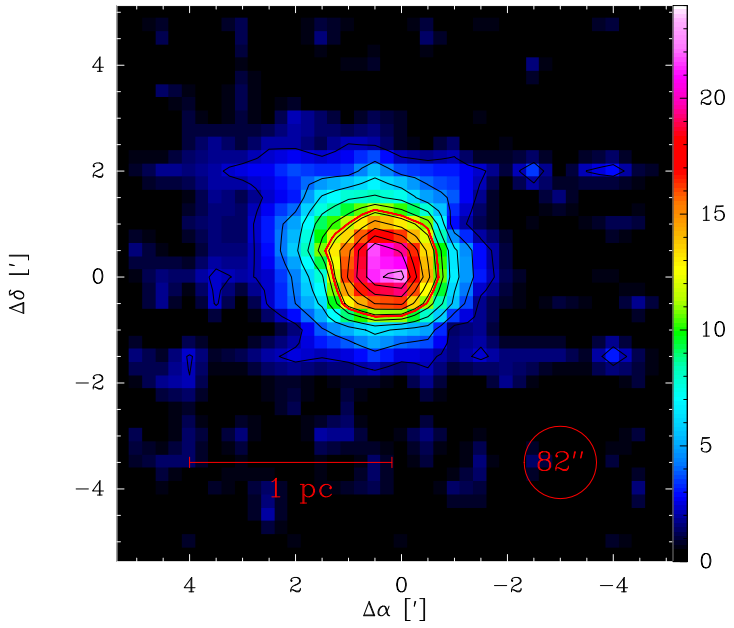

Figure 27: Map of the HCO^+(4-3) integrated intensity [K km s^{-1}] for S140, integrated from $v = -14$ to 0 $km\,s^{-1}$. The coordinates are relative to $\alpha_{1950} = 22^h\,17^m\,41^s$ and $\delta_{1950} = 63°3'\,40''$. Conture levels are from 2 K km s^{-1} to 22 K km s^{-1} in steps of 2 K km s^{-1}. The bold red conture level is to the value 11.35 K. The peak value is 22.7 K km s^{-1} at the center point and the average T_{rms} is 0.2 K.

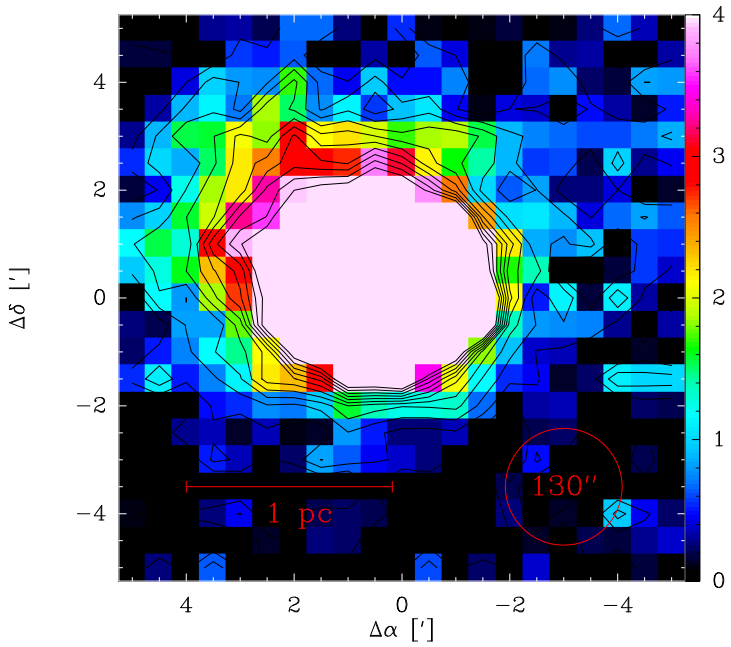

Figure 28: "Overexposed" map of the HCO^+(3-2) integrated intensity [K km s^{-1}] for S140, integrated from $v = -14$ to 0 km s^{-1}. Coordinates are relative to $\alpha_{1950} = 22^h\,17^m\,41^s$ and $\delta_{1950} = 63°3'\,40''$. The data axis is stretched from 20 K km s^{-1} to 4 K km s^{-1} and conture levels are from 0.2 K km s^{-1} to 4 K km s^{-1} in steps of 0.2 K km s^{-1}. The average T_{rms} is 0.08 K.

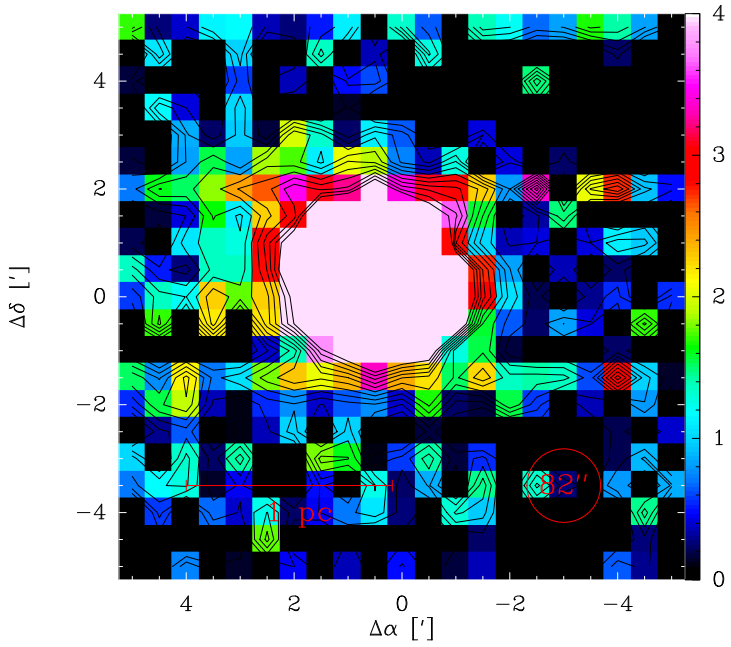

Figure 29: "Overexposed" map of the HCO^+(4-3) integrated intensity [K km s^{-1}] for S140, integrated from $v = -14$ to 0 km s^{-1}. Coordinates are relative to $\alpha_{1950} = 22^h\,17^m\,41^s$ and $\delta_{1950} = 63°3'\,40''$. The data axis is stretched from 24 K km s^{-1} to 4 K km s^{-1} and conture levels are from 0.2 K km s^{-1} to 4 K km s^{-1} in steps of 0.2 K km s^{-1}. The average T_{rms} is 0.2 K.

6.2.2 A cut through S140

In order to investigate the physical conditions throughout the cloud, several positions on a line from the south-west to the north-east were measured in the raster mapping mode. The offset relative to the center of the positions as well as the obtained data can be found in Tab. 20 and the recorded spectra are presented in Fig. 34. Positions without a line exceeding $3 \cdot T_{rms}$ are left out and negative integrated line intensities are also omitted, since a measurement in absorption is unlikely. Negative integrated intensities with a detected $3 \cdot T_{rms}$ line are observed in the (13'/17') position for HCO^+(3-2) and in the (10'/13'), (11.5'/15') and (9.5'/12.5') positions for HCO^+(4-3). The disturbance of the receiver for 330-365 GHz, discussed in Sect. 6.2.1, is therefore again observed. The plot of the (-1.5'/-2') position in Fig. 30 also shows a much larger noise in HCO^+(4-3) than in HCO^+(3-2), although the T_{rms} is comparable (0.02 K and 0.01 K, resp.). In Fig. 34, we also present interpolated data, obtained from the maps (on-the-fly measurement). Such positions are in agreement with the measurement for the cut due to the fact, that also raster mapping spectra were used for the map (and vice versa). The errorbars in the figure indicate the pointing error in the direction of $\Delta\alpha$ and T_{rms} for the integrated intensity.

Measurements at the same position for the ^{13}CO(2-1) and ^{12}CO(3-2) positions have been perfomed by Stäuber (2003): His measurements have shown a ratio of the integrated intensity between the (-1.5'/-2') position and the center position in the order of 10 for both transitions. Since the PDR lies in between and a comparison of the cosmic ray ionization rate on both sides is aimed, we have measured at an offset of (-1.5'/-2') for several hours for a high signal-to-noise ratio. For HCO^+(3-2), we have obtained a ratio of the integrated intensity between the positions of 26, whereas the ratio for HCO^+(4-3) is with 150 even higher. The higher ratio for the $J = 4 \rightarrow 3$ transition is likely due to the lower temperature in front of the dense core at the offset (-1.5'/-2'), leading to a depopulated upper level. In addition, the density at this point may not be high enough to achieve the critical density needed for this transition. On the northern part of the center, the observed intensities are also diverse to those of ^{13}CO(2-1) and ^{12}CO(3-2): Up to the (15'/19.5') position, both CO transitions show integrated intensities not below 22 % of the peak value (for ^{13}CO(2-1)) and 14 % (for ^{12}CO(3-2)). As given in Fig. 35 and Fig. 36, the HCO^+ emission is much more concentrated aroud the center. At distances from (0'/0') further than 9' for $J = 3 \rightarrow 2$ and 5' for $J = 4 \rightarrow 3$ no line has been detected up to a distance of 24'. This strong concentration has also been observed in the maps (Sect. 6.2.1). The two weak lines, observed at (14.5'/19') and (15'/19.5'), are red-shifted compared to the center positions. Center velocities of the line within -13 to -10 km s^{-1} in the north-east compared to approximately -7 km s^{-1} in the center have also been observed in ^{13}CO(2-1) by Stäuber (2003). The emission in the north-east is likely due to another source: Tafalla et al. (1993) have identified a Young Stellar Object at (14'/20'), denoted by core F in this paper. They have discovered several YSOs in S140/L1204 that lay not in the center, by searching high-velocity emission in CS(2-1) due to molecular outflows. In the same work, further sources at (6'/8') and (8'/12') (called C- and D-core, resp.) are found. Their estimated masses and integrated intensities in CS(2-1) are about 2 times higher than for the F-core. The F-core lies within 1' from the (15'/19.5') positions at which a line was detected in our work. The C-core lies about 1' form the (5.5'/7') and 1.5' from the (7'/9') position and the D-core at 1.5' from (9.5'/12.5'). However, no emission was measured in our work for the C- and D-core.

The emitting area

Since the emitting area may not fill the beam, the question is, whether the source is point-like or spread out: As a model for the emission of the source, we have assumed a Gaussian peak with a certain FWHM and a maximum value at the center position equal to the highest measured integrated intensity. As discussed in Sect. 5.4, the measured intensity is averaged over a broad area due to the limited angular resolution. For our calculation, the beam response function of KOSMA was assumed to be Gaussian with FWHM given in Tab. 16. No side lobes have therefore been taken into account. The observed intensity $O(\alpha, \delta)$ can be expressed as the convolution of two Gaussians as (c.f. Eq. 104)

$$O(\alpha,\delta) = O_0 \cdot \frac{4ln(2)}{\pi} \cdot \frac{F_{Source}^2 + F_{Beam}^2}{F_{Source}^2 \cdot F_{Beam}^2} \int\int e^{-\frac{4ln(2)\left((\alpha-\tilde{\alpha})^2+(\delta-\tilde{\delta})^2\right)}{F_{Beam}^2}} \cdot e^{-\frac{4ln(2)\left(\tilde{\alpha}^2+\tilde{\delta}^2\right)}{F_{Source}^2}} d\tilde{\alpha}d\tilde{\delta} \ ,$$

with the FWHM of the beam response function F_{Beam}, the FWHM of the source F_{Source} and the intensity O_0 at the center position of the source, assumed to be at (0'/0') for this equation. The integral cannot be solved analytically and was therefore evaluated numerically.

To determine the center of the source and the observed FWHM $F_{Obs.}$, the conture level to 50 % of the maximum value were determined for the maps of HCO^+(3-2) and HCO^+(4-3) (Fig. 26 and 27). A circle was then fitted on this conture levels, using the least-square method. The so obtained FWHM and center are presented in Tab. 17 and Fig. 33. Both circle fit quite accurately the conture level. The center of the two circles are in the north-east of the (0'/0') position. Since the deviation to the (0'/0') position is larger than the pointing accuracy and both positions are very close (4"), a real effect cannot be excluded, but further investigation would be needed. A positive result would not be in agreement to Wilner et al. (1993). They have found the emission peak of HCO^+(1-0) close to center using a 5" resolution aperture synthesis observation.

Map	Center (α,δ) [arcmin]	$F_{Obs.}$ [arcmin]	F_{Source} [arcmin]	F_{Beam} [arcmin]
HCO^+(3-2)	(0.35, 0.29)	2.73	1.67	2.16
HCO^+(4-3)	(0.33, 0.23)	2.08	1.57	1.36

Table 17: Circle fitted on the 50 % conture levels of the S140 maps.

The so obtained values for $F_{Obs.}$ were then used to determine F_{Source}. The convolution was evaluated at a point $(\alpha_\circ/\delta_\circ)$ of the circle with the correct F_{Beam}. F_{Source} was varied until $O(\alpha_\circ, \delta_\circ)$ fitted to the integrated intensity of the 50 % conture level. This method is in principle a deconvolution. In the case of two Gaussians, it can be replaced by the equation $F_{Obs.}^2 = F_{Source}^2 + F_{Beam}^2$ (Kraus 1966) leading to the same results. The calculated values are presented in Tab. 17. Using a distance of 910 pc, the diameter of the emitting region can be estimated to be between 0.5 and 0.7 pc.

On the other side, the convolution can be used to estimate values of at a certain point: If the center of the source is assumed to be on the above determined point, the evaluation of the convolution at (-1.5'/-2') gives for the $J = 3 \rightarrow 2$ transition an integrated intensity of 0.7 K km s^{-1} and for the $J = 4 \rightarrow 3$ transition an integrated intensity of 0.11 K km s^{-1}. Both values are in the same size as the measured integrated intensity (Tab. 20). We have therefore to take the values at this point as an upper limit. The value of the convolution is very sensitive on the center position and the evaluated point: If we assume the center position of the source at (0'/0') and take a pointing error of 10" into account for the (-1.5'/-2') position, the calculated values are 2.58 K km s^{-1} and 0.84 K km s^{-1} for HCO^+(3-2) and HCO^+(4-3), respectively.

The values of the convolution at each point along the cut are given in Fig. 35 and 36. For this plot, a source positions after Tab. 17 has been used. The good agreement with the on-the-fly points is obvious, especially for HCO^+(3-2). To the north-east of the core, an excess to the convolved values is visible for points at a distance above 3'. The Gaussian for the sources are also plotted in this figures.

Column density

For the calculation of the cosmic ray ionization rate, the density and the kinetic temperature is needed. We will calculate approximations under the assumption of a local thermal equilibrium (LTE), as introduced in Sect. 3.3. We refer to Blake et al. (1987) for this section.

Under the assumption that the lines are optically thin and the background radiation temperature T_{BG} is much smaller than the excitation temperature T_{ex}, the radiative transfer equation (22) with the emission expressed by the Einstein-A-Coefficient (Eq. 23) is

$$\frac{dI_\nu}{ds} = \epsilon_\nu = \frac{h\nu}{4\pi}\phi(\nu) n_u A_{ul} \ . \tag{120}$$

Integration over s and ν leads together with the Doppler relation to

$$\int T_{mb} dv = \frac{hc^3 A_{ul}}{8\pi k \nu^2} \int n_u ds \ . \tag{121}$$

For this step, we have neglected the background radiation. With the level population for LTE, we get

$$\int T_{mb} dv = \frac{hc^3 A_{ul}}{8\pi k \nu^2} \int n \frac{g_u e^{-\frac{E_u}{kT_{ex}}}}{Q(T_{ex})} ds \ . \tag{122}$$

We assume a spatially constant excitation temperature T_{ex} and density n. The equation takes then the form

$$\frac{8\pi k \nu^2 \int T_{mb} dv}{hc^3 A_{ul} g_u} = \frac{N}{Q(T)} e^{-\frac{E_u}{kT_{ex}}} = \frac{N_u}{g_u} \ . \tag{123}$$

We have introduced the column density N as the integral along the line of sight over the density ($N = \int n \, ds$). We have also used N_u to express the colum density of molecules in the state u. The natural logarithm of the equation is

$$ln\left(\frac{8\pi k \nu^2 \int T_{mb} dv}{hc^3 A_{ul} g_u}\right) = ln\left(\frac{N}{Q(T)}\right) - \frac{E_u}{kT_{ex}} \ , \tag{124}$$

and a plot of the left hand side versus the energy should produce a stright line whose intercept is

$$ln\left(\frac{N}{Q(T)}\right) \ , \tag{125}$$

leading to the column density. The excitation temperature can be estimated by the slope of the line

$$-\frac{1}{kT_{ex}} \ . \tag{126}$$

We have performed this calculation for the (0'/0') position of the cut through S140. In addition to our measurements of the HCO^+(4-3) and HCO^+(3-2) transitions, data for HCO^+(1-0) were found in Ewald (1986). He has also measured this line with the KOSMA telescope. His values of the antenna temperature have been corrected to the main beam brightness temperature by the coefficent $\eta_S = 0.7$ found in the same thesis and the line width has been used to calculated an integrated intensity of 7.87 K km s^{-1}.

A plot of Eq. (123) (called LTE diagramm) for our data is presented in Fig. 31. The linear regression line for all three transitions and the line through the two points of our measurement are shown in this figure. The errorbars indicate a 30 % error due to the calibration uncertainty. By using this error, we find the line for all three points nearly within the errorbars. For the calculation, molecular data from the LAMDA (Schöier et al. 2005) have been used and the partition function $Q(T)$ was obtained from the JPL database and interpolated to the value of the excitation temperature T_{ex}. The so obtained column density and excitation temperature can be found in Tab. 18. The two calculated values for the column density lay within 12 %, whereas the excitation temperatures deviate by a factor of more than 2. Savage et al. (2004b) have achieved a column density of $2.3 \cdot 10^{14}$ cm^{-2} which is slightly higher than our value.

Transitions HCO^+	Column Density [cm^{-2}]	T_{ex} [K]
(4-3), (3-2)	$9.8 \cdot 10^{13}$	57.3
(4-3), (3-2), (1-0)	$1.1 \cdot 10^{14}$	22.0

Table 18: Column densities and excitation temperature T_{ex} of HCO^+ at the (0'/0') position.

Cosmic ray ionization rate

For an estimation of the cosmic ray ionization rate ζ [s^{-1}] by equation (118), further assumptions on the H_2 and the electron density are needed. In addition, the density n(HCO^+) is required rather than the column density N(HCO^+). An estimation of the density however was not possible in our simple model of the emitting region. We have therefore replaced the ratio of the density by the ratio of the column density as a first approximation:

$$\frac{n(\mathrm{HCO^+})}{n(\mathrm{H_2})} \approx \frac{N(\mathrm{HCO^+})}{N(\mathrm{H_2})} = \frac{\int n(\mathrm{HCO^+})dl}{\int n(\mathrm{H_2})dl} \tag{127}$$

Savage et al. (2004b) give for the hydrogen column density at the center of S140 a value of $\approx 8 \cdot 10^{22}$ cm^{-2}, which was used for our calculation.

The electron density can be estimated by the fact that the electron abundance $x_e = n(e)/n(\mathrm{H_2})$ lies within the small range between $10^{-6.9}$ and $10^{-7.3}$ for massive cores like S140 (Bergin et al. 1999). The range of possible values for x_e leads to an uncertainty in the cosmic ray ionization rate of a factor of 2.5. Since the electron density $n(e)$ is necessary, an estimation of $n(\mathrm{H_2})$ is needed. We have used an averaged value, since the radially dependent profile of HCO^+ is not known. Zhou et al. (1993) present the density of H_2 for a spherical symmetric model of S140 as the power-law

$$n(r) = n_0 \cdot \left(\frac{r}{r_{in}}\right)^{-0.8} , \tag{128}$$

with a density of $n_0 = 1.4 \cdot 10^6$ cm^{-3} at the innermost radius $r_{in} = 0.026$ pc of the model (c.f. Sect. 5.2). The outer radius of the model was $r_{out} = 0.44$ pc. This size is slightly larger than the range of the emitting region of HCO^+ as determined before (0.5 - 0.7 pc diameter). The integral for the averaged H_2 density in the sphere

$$\bar{n} = \frac{1}{\frac{4\pi}{3}(r_{out}^3 - r_{in}^3)} \int_{r_{in}}^{r_{out}} 4\pi n(r) r^2 dr \propto r_{out}^{-0.8} , \tag{129}$$

is strongly dependent on r_{out} for $r_{out} \leq 1$ pc and therefore a possible source of uncertainty. We assume $r_{out} = 0.44$ pc as suggested in Zhou et al. (1993) and obtain $\bar{n} = 2.0 \cdot 10^5$ cm^{-3}. An outer radius r_{out} of 0.25-0.35 pc as found from the estimated size of the emitting area leads to $\bar{n} = (2.5 - 3.1) \cdot 10^5$ cm^{-3}. Using an averaged H_2 density of $\bar{n} = 2.0 \cdot 10^5$ cm^{-3}, the electron density

$n(e)$ is between $1.0 \cdot 10^{-2}$ cm^{-3} and $2.5 \cdot 10^{-2}$ cm^{-3}, depending on x_e.

Since LTE was assumed, we have used the excitation temperature T_{ex} to calculate k_{CO}. The cosmic ray ionization rate obtained from the equation

$$\zeta = k_{CO}(T) \cdot \frac{n(\mathrm{HCO^+}) \cdot n(e)}{n(\mathrm{H_2})} \approx k_{CO}(T_{ex}) \cdot x_e \cdot n(\mathrm{H_2}) \cdot \frac{N(\mathrm{HCO^+})}{N(\mathrm{H_2})} \tag{130}$$

is presented in Tab. 19. We give ζ using both values of the column densities and temperature determined above. The difference of ζ for the two sets (N(HCO$^+$),T_{ex}) is due to the much larger temperature obtained from the HCO$^+$(4-3) and HCO$^+$(3-2) transition. Since k_{CO} is scaled by $T^{-0.69}$, ζ is approximately by a factor of 2 larger for the set with $T = 57.3$ K. Together with the factor of 2 uncertainty in x_e, the value of the cosmic ray ionization rate is $(0.93 - 4.9) \cdot 10^{-17}$ s^{-1}. If r_{out} is chosen as suggested in our work, the value of ζ is about 25 % to 55 % larger, i.e. $(1.2 - 7.6) \cdot 10^{-17}$ s^{-1}.

van der Tak & van Dishoeck (2000) have calculated ζ using submillimeter observations of the H^{13}CO$^+$(4-3) and H^{13}CO$^+$(3-2) line. They give a cosmic ray ionization rate at the center of S140 to $3.7 \cdot 10^{-17}$ s^{-1} which lies within the span of the value in our work.

$N(\mathrm{HCO^+})$ [cm^{-2}]	T_{ex} [K]	ζ ($x_e = 10^{-6.9}$) [s^{-1}]	ζ ($x_e = 10^{-7.3}$) [s^{-1}]
$9.8 \cdot 10^{13}$	57.3	$2.3 \cdot 10^{-17}$	$9.3 \cdot 10^{-18}$
$1.1 \cdot 10^{14}$	22.0	$4.9 \cdot 10^{-17}$	$2.0 \cdot 10^{-17}$

Table 19: Cosmic ray ionization rate ζ [s^{-1}] of S140 at the center position.

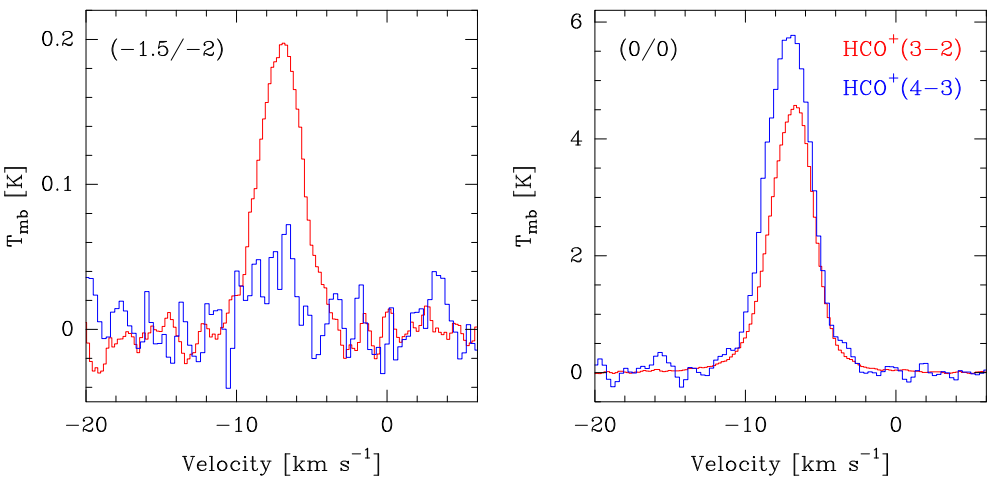

Figure 30: Map of the recorded spectra for HCO^+ of S140 at an offset of (-1.5'/-2') and at the center (0'/0'). The $J = 3 \rightarrow 2$ transition (267.557 GHz) is indicated by a red line and the $J = 4 \rightarrow 3$ transition (356.734 GHz) by a blue line.

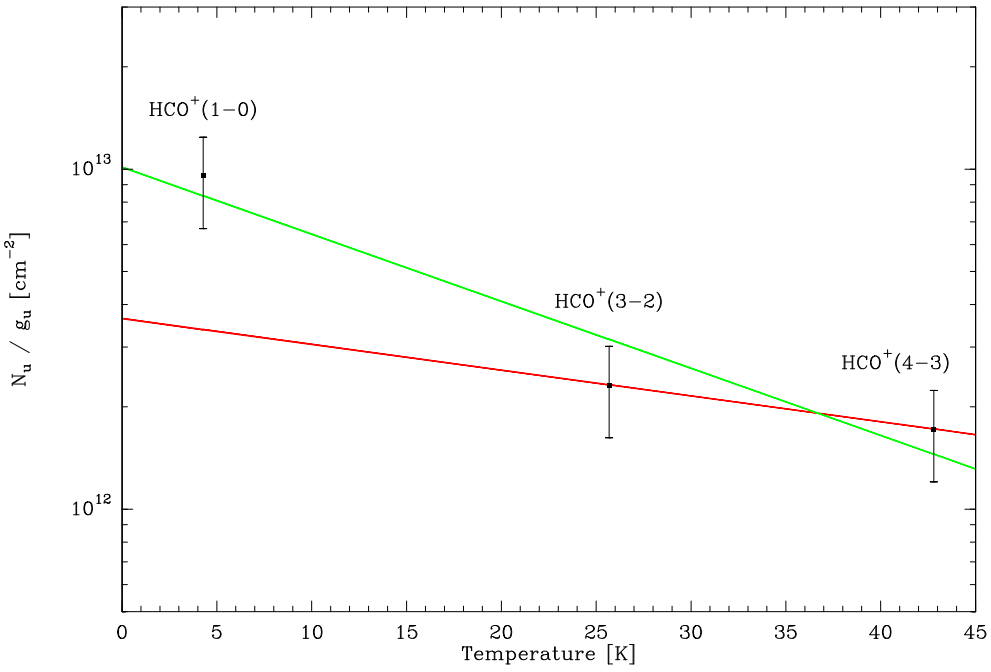

Figure 31: LTE diagram for HCO^+ at the center position of S140. The two lines were used to determine the column density and excitation temperature T_{ex}. The line through the two points obtained with our data is given in red and the line in green indicates the fit for all 3 points.

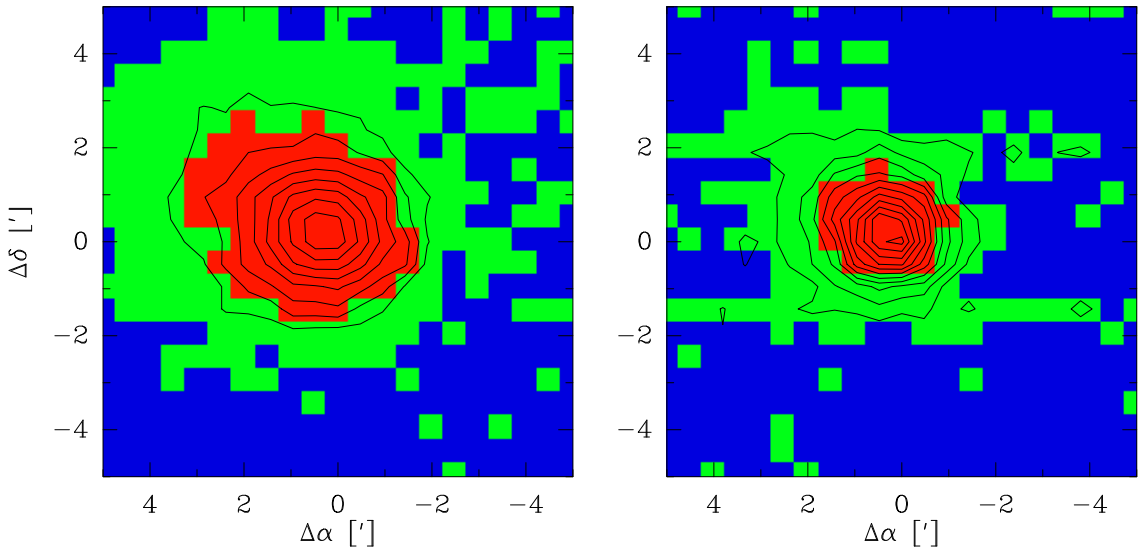

Figure 32: Maps of the detected lines in S140 for HCO^+(3-2) (left) and HCO^+(4-3) (right). Points without a detected line are given in blue. Lines that are only detected by averaging over several measurements are given in green. Positions where the selection criterion applies are given in red. The conture lines from Fig. 26 and 27 are superimposed.

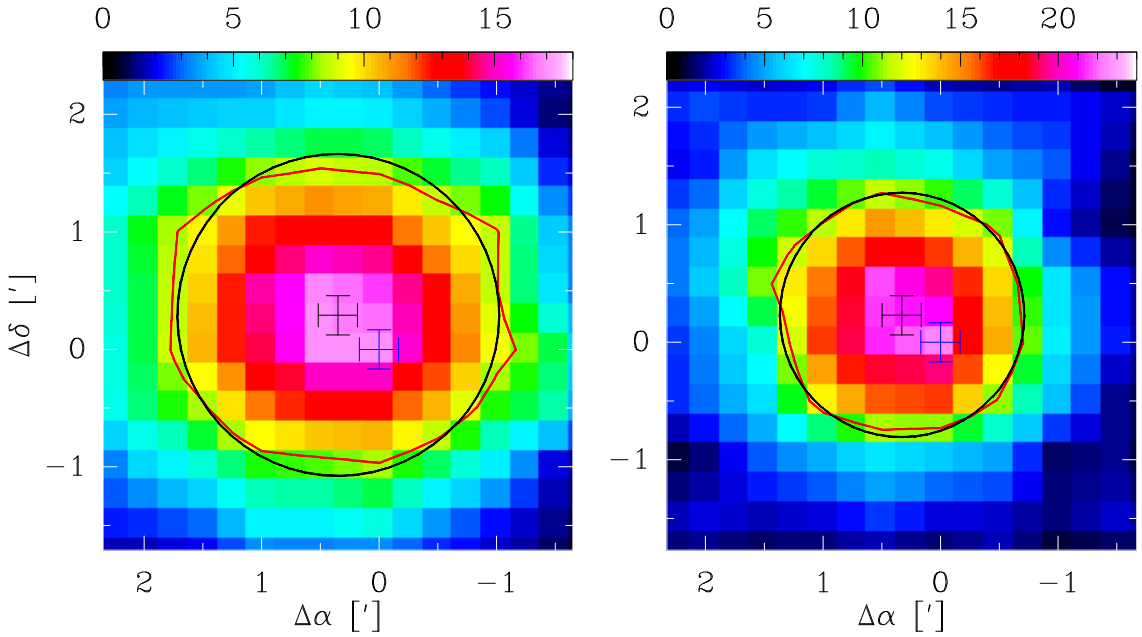

Figure 33: A circle was fitted on the FWHM conture line (red) of the HCO^+(3-2) transition (left) and HCO^+(4-3) transition (right). The center of the circle and the (0'/0') position are given by a blue cross and a black cross, respectively. The size of the cross indicates the the pointing accuracy of 10".

Position	HCO^+(3-2)						HCO^+(4-3)					
	T_{mb} [K]	$\int T_{mb}dv$ [K km s^{-1}]	RMS [K]	Width [km s^{-1}]	Pos. [km s^{-1}]	Int. Time [s]	T_{mb} [K]	$\int T_{mb}dv$ [K km s^{-1}]	RMS [K]	Width [km s^{-1}]	Pos. [km s^{-1}]	Int. Time [s]
(-1.5'/-2')	0.20	0.65	0.01	3.3	-7.1	9247	0.07	0.15	0.02	2.7	-7.4	9247
(0'/0')	4.57	17.20	0.02	3.4	-6.9	3019	5.8	22.7	0.1	3.5	-7.1	2995
(1.5'/2')	1.58	4.28	0.03	2.6	-7.1	884	1.2	3.1	0.1	2.2	-7.3	892
(3'/4')	0.37	0.79	0.03	2.0	-7.5	888	0.19	0.55	0.06	4.4	-8.2	888
(4.5'/6')	0.12	0.26	0.03	3.6	-7.4	820	0.11	-	0.06	-	-	820
(5.5'/7')	0.18	0.31	0.03	2.2	-7.0	820	0.13	-	0.05	-	-	820
(7'/9')	0.06	-	0.03	-	-	820	0.07	-	0.05	-	-	820
(9.5'/12.5')	0.04	-	0.03	-	-	820	0.12	-	0.04	-	-	820
(10'/13')	0.03	-	0.03	-	-	820	0.13	-	0.04	-	-	820
(10.5'/13.5')	0.04	-	0.03	-	-	800	0.10	-	0.04	-	-	800
(11.5'/15')	0.04	-	0.03	-	-	800	0.14	-	0.04	-	-	800
(13'/17')	0.11	-	0.03	-	-	800	0.07	-	0.05	-	-	800
(14.5'/19')	0.63	1.02	0.03	1.8	-10.4	800	0.45	0.93	0.05	1.7	-10.6	800
(15'/19.5')	0.43	0.57	0.04	1.8	-10.4	800	0.33	0.63	0.05	1.5	-10.5	800

Table 20: Characteristics of the cut through S140. The integrated intensity was calculated between v = -14 km s^{-1} and 0 km s^{-1}. The integration time gives the total on-source time of the measurement. Integrated intensities are only given for positions with detected lines. The position and width (FWHM) of the lines were obtained by fitting a Gaussian on the spectra.

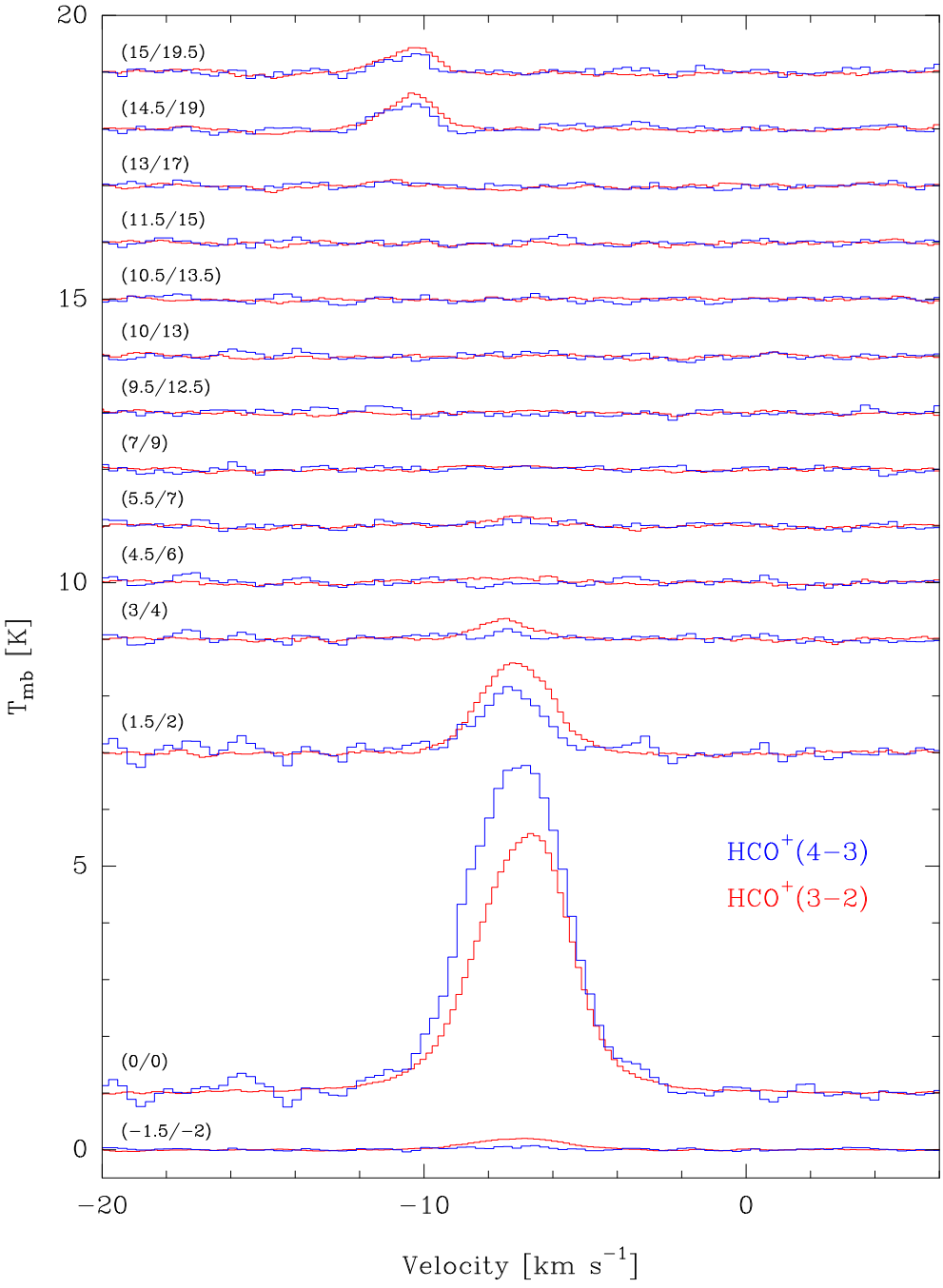

Figure 34: Line profiles for HCO^+ of a cut through S140 from the core to the north-east. The line profiles have an offset of 1, 7, 9, 10, 11, 12, ... K and the positions relative to the center ($\alpha_{1950} = 22^h\,17^m\,41^s$ and $\delta_{1950} = 63°3'\,40''$) are given on the left to the spectra. The x-range is -20 to 6 km s^{-1}.

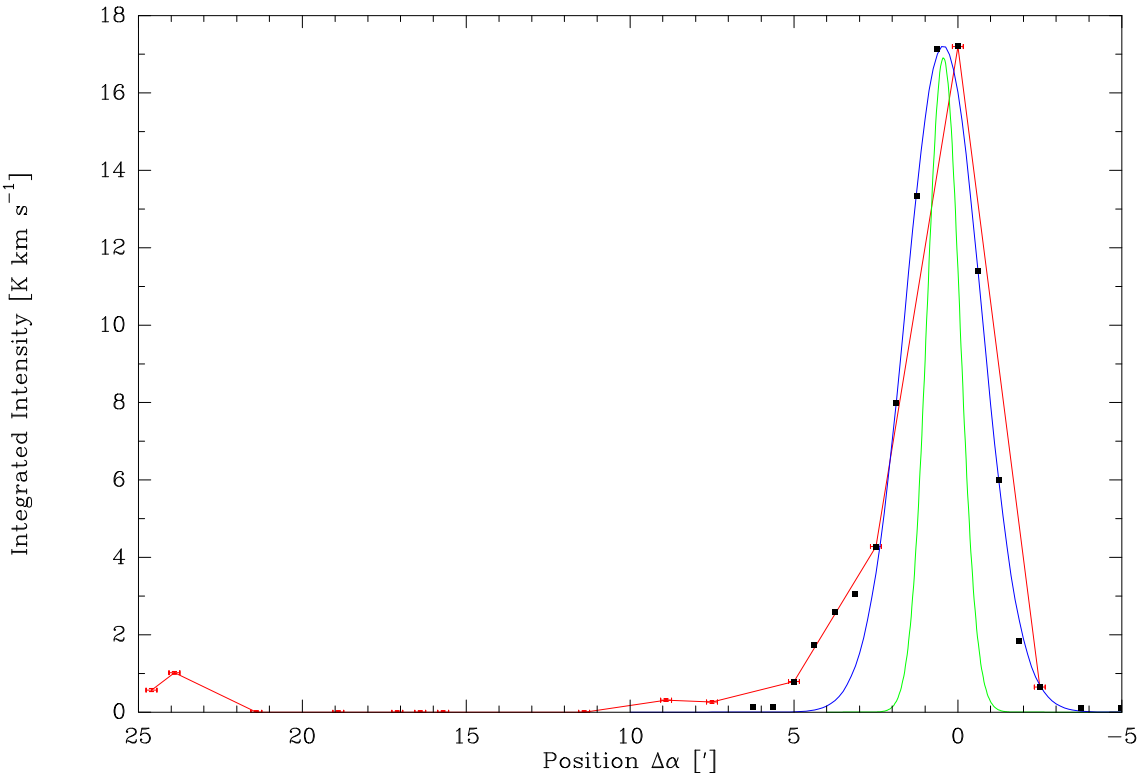

Figure 35: A cut through S140 from the core to the north-east of the integrated intensity $\int T_{mb} dv$ of HCO^+(3-2). The position $\Delta\alpha$ corresponds to the offsets given in Tab. 20. The two curves indicate the source (green) and its convolution with the antenna beam (blue). Data from the maps are denoted by black squares.

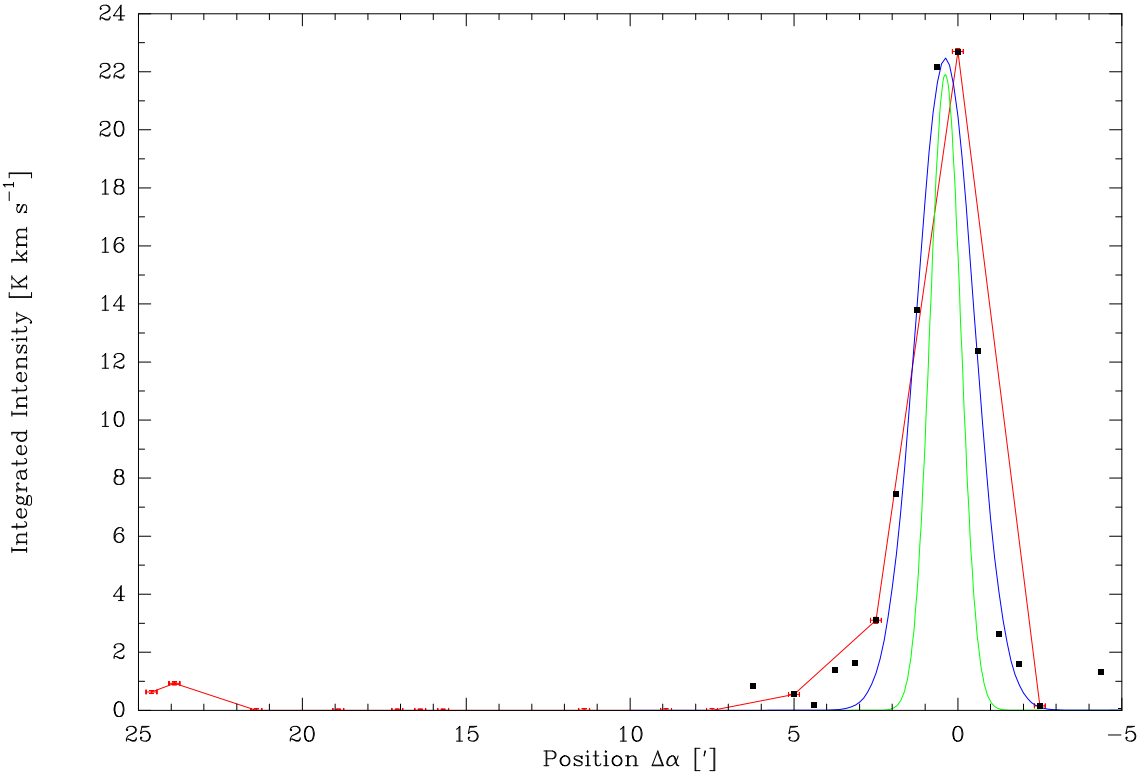

Figure 36: A cut through S140 from the core to the north-east of the integrated intensity $\int T_{mb} dv$ of HCO^+(4-3). The position $\Delta\alpha$ corresponds to the offsets given in Tab. 20. The two curves indicate the source (green) and its convolution with the antenna beam (blue). Data from the maps are denoted by black squares.

6.3 Observations of W3

W3 is a giant molecular cloud with ongoing star formation. It lies in a chain of giant HII regions (W3, W4 and W5) in the Perseus spiral arm of our galaxy. The mass of the molecular cloud is more than 10^5 $M_\odot$ at a distance of 2.3 kpc (Kramer et al. 2004). W3 contains the giant molecular cloud called W3-Core and a smaller core in the south-east called W3(H_2O) and W3(OH) (Fig. 37). In W3-Core, which was observed in our work, various infrared sources (IRS 2 - 7) have been found previously. The brightest among them is IRS5 with a luminosity of $3 \cdot 10^5$ $L_\odot$. It is believed that this source consists of more than one B stars, each with a mass of 10 $M_\odot$. Another well observed source in W3-Core is IRS4, an early-O9 star which is more evolved than the other protostars in the W3-Core and has already broken free from its parent cloud (Helmich et a. 1997). W3(H_2O) and W3(OH) also contain YSOs. In these two compact HII regions, H_2O and OH maser have been observed. The center of our observation, IRS3a lies in W3-Core and is believed to be the ionizing star of one of the HII regions in W3-Core, W3B. IRS3a is a young O6 star. IRS3a has also been detected in X-rays with the Chandra X-Ray Observatory .

Maps

The maps of our observations are presented in Fig. 38 and 39 for HCO^+(3-2) and HCO^+(4-3), respectively. In Fig. 40, we give the map for ^{13}CO(2-1) and in Fig. 41 the map for ^{12}CO(3-2). The emitting area of HCO^+ is much more concentrated at the center than for CO, as was also observed in S140. The lines of both CO transitions are optically thick in the center (c.f. Appendix B). A line position of about -40 km s^{-1} has also been observed by Helmich et a. (1997).

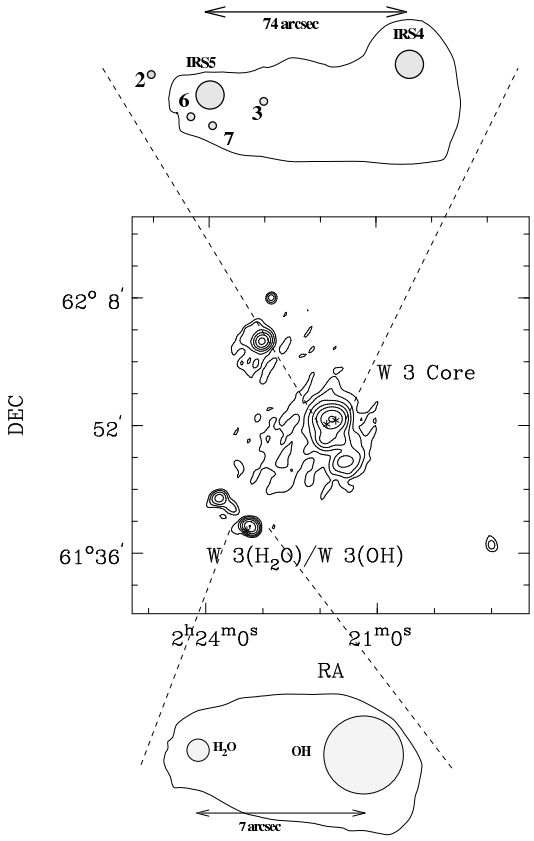

Figure 37: A high resolution 25 μm IRAS map of the W3 region. The condensation in the center is the core of the giant molecular cloud, W3-Core. W3(OH) and W(H_2O) are situated to the south-east. Note that coordinates in this map are for the equinox 1950.

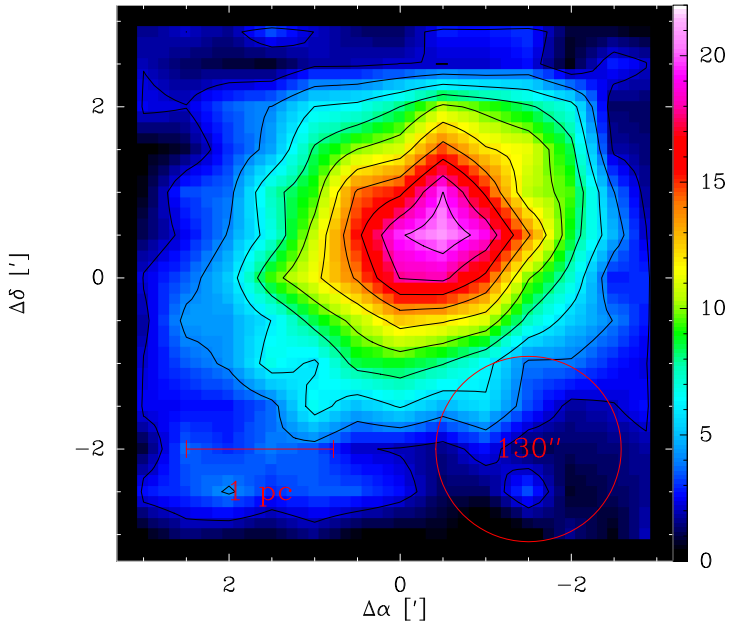

Figure 38: Map of the HCO^+(3-2) integrated intensity [K km s^{-1}] for W3, integrated from $v = -55$ to -25 km s^{-1}. The coordinates are relative to $\alpha_{2000} = 2^h\,25^m\,37.8^s$ and $\delta_{2000} = 62°5'\,52''$. Conture levels are from 2 K km s^{-1} to 20 K km s^{-1} in steps of 2 K km s^{-1}. The peak value is 21.1 K km s^{-1} at the offset (-0.5'/0.5') and the average T_{rms} is 0.1 K.

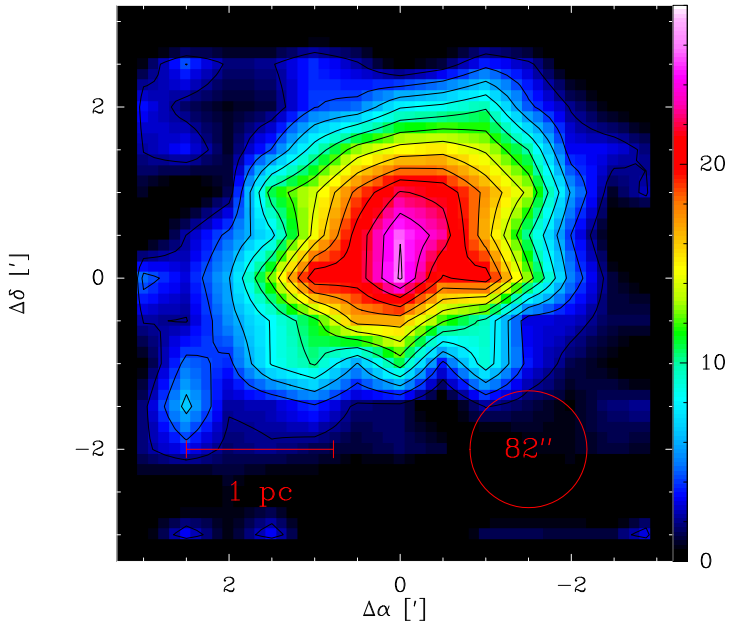

Figure 39: Map of the HCO^+(4-3) integrated intensity [K km s^{-1}] for W3, integrated from $v = -55$ to -25 km s^{-1}. The coordinates are relative to $\alpha_{2000} = 2^h\,25^m\,37.8^s$ and $\delta_{2000} = 62°5'\,52''$. Conture levels are from 2 K km s^{-1} to 26 K km s^{-1} in steps of 2 K km s^{-1}. The peak value is 26.3 K km s^{-1} at the center point and the average T_{rms} is 0.2 K.

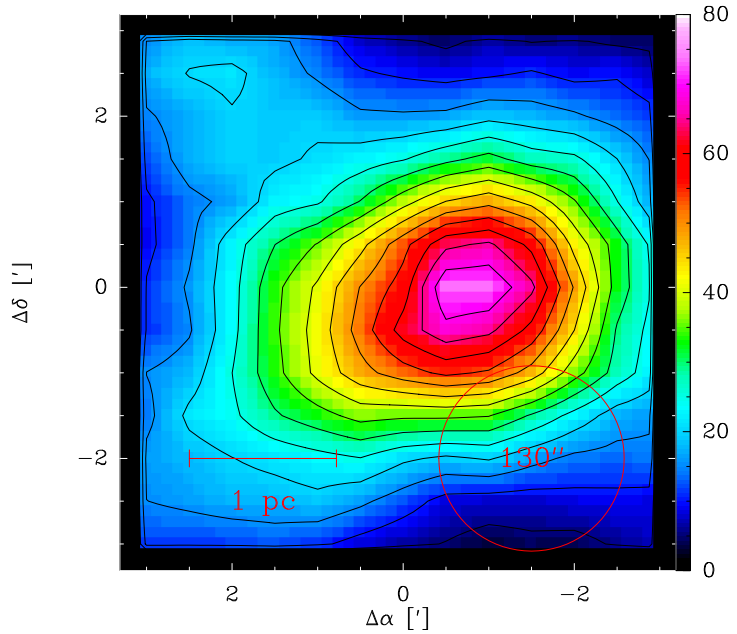

Figure 40: Map of the ^{13}CO(2-1) integrated intensity [K km s^{-1}] for W3, integrated from $v = -55$ to -25 km s^{-1}. The coordinates are relative to $\alpha_{2000} = 2^h\,25^m\,37.8^s$ and $\delta_{2000} = 62°5'\,52''$. Conture levels are from 5 K km s^{-1} to 70 K km s^{-1} in steps of 5 K km s^{-1}. The peak value is 74.4 K km s^{-1} at the offset (-1'/0') and the average T_{rms} is 0.2 K.

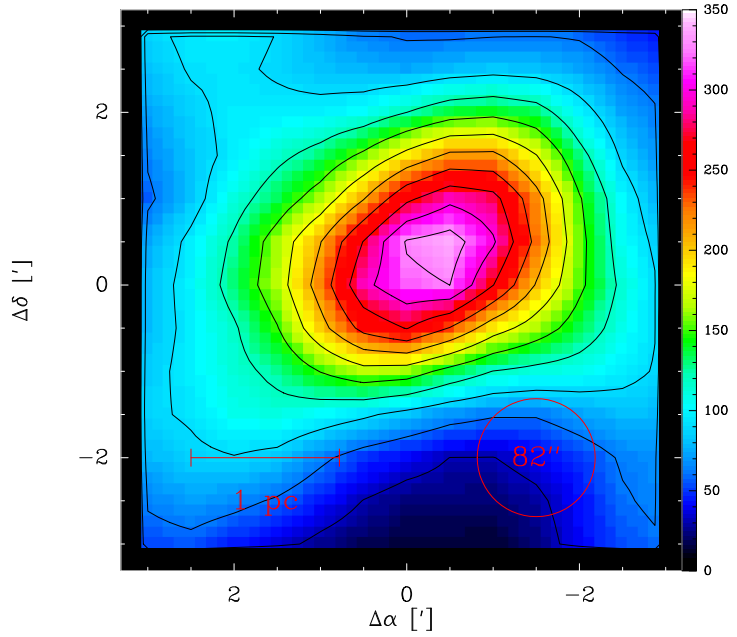

Figure 41: Map of the CO(3-2) integrated intensity [K km s^{-1}] for W3, integrated from $v = -60$ to -20 km s^{-1}. The coordinates are relative to $\alpha_{2000} = 2^h\,25^m\,37.8^s$ and $\delta_{2000} = 62°5'\,52''$. Conture levels are from 30 K km s^{-1} to 330 K km s^{-1} in steps of 30 K km s^{-1}. The peak value is 336.1 K km s^{-1} at the offset (-0.5'/0.5') and the average T_{rms} is 0.4 K.

7 Conclusion and Outlook

We have calculated the line intensities of the CH, CH^+, NH, OH^+, SH and SH^+ hydrides and the water ion H_2O^+ for the high-mass object AFGL 2591 and the two low-mass objects IRAS 16293-2422 (Class I) and TMC 1 (Class 0). For several species, very weak line intensities below 10^{-3} K km s^{-1} were found. CH, an alternative model of CH^+ and NH have shown line intensities that are promising for a detection with HIFI. For weak lines however, the estimated integration time is very sensitive on the calculated intensity. Therefore, the predicted values should be seen as a rough approximation.

For our calculation, we have used the LTE assumption since no collision rate coefficients were available for the considered molecules. The excitation mechanism for some molecules is ambiguous, because they are destroyed by collisions rather than excited. For SH, further investigations could be carried out with approximative collision rate coefficients in order to compare the fully solved radiative transfer problem with the LTE approximation used in our work. In an altered chemical simulation, the CH^+ and OH^+ line intensity could be calculated with the formation rate rather than with the abundances, as it was done in our work. We did not achieve to calculate the Einstein-A-Coefficients of NH^+, since this was not possible with `SPCAT`. An estimation of these coefficients could be done as described in Whiting et al. (1974).

Observations of HCO^+ and CO in S140 and W3 were carried out with the KOSMA telescope. Maps of both objects were measured in the on-the-fly mode and aditionally, a cut through S140 from the core to the north-east was observed in the raster mapping mode. The observations have shown, that the radiation of HCO^+ is much more concentrated to the center than that for CO. The size of the emitting area was estimated for S140 by the convolution of the beam response function with a simple model of the source. For the center of S140, the column density and excitation temperature of HCO^+ was estimated under the LTE assumption. The calculated cloumn density lies within a factor of two to a value found by Savage et al. (2004b). The cosmic ray ionization rate ζ was determined with a simple chemical network for HCO^+. Due to large uncertainties in the H_2 density $n(H_2)$, the fractional abundance of electrons and the excitation temperature, the calculated value lies in the large range between $0.9 \cdot 10^{-17}$ s^{-1} and $4.9 \cdot 10^{-17}$ s^{-1}.

Due to a not yet identified problem with KOSMA, some of the recorded spectra contained only noise. For positions with a strong line intensity, such spectra were removed. The integrated intensity at points with a weak intensity, however, is afflicted with uncertainty, since no method was found to remove empty spectra there. The column density was obtained under the LTE assumption and could be replaced by a full radiative transfer calculation, since collion rate coefficients would be available for HCO^+. This would likely lead to a lower column density, since values obtained with LTE tend to be too high. The range of possible values for ζ could probably be lessen, if the simple chemical network which consists only of the main HCO^+ forming and destructing reactions would be replaced by the chemical model as used in Sect. 5.2. A further analyse of the W3 data is pending due to lake of time at the end of the thesis.

A Molecular Data

The used molecular data is presented here: References and the notation of the quantum numbers for the indivual molecules are given in Sect. 5. The estimated error of the frequency (in MHz) is given in parentheses to the right of the frequency (in GHz). The Einstein-A-Coefficients are presented in the following way: $a(b) \equiv a \cdot 10^b$. "Band" denotes the Herschel-Band of the transition (Tab. 6) and E_{up} is the energy of the upper level expressed in Kelvin by $E = kT$.

Transitions of H_2O^+ with an estimated error larger than 30 MHz are omitted. Not resolved lines (e.g. the first and second tabulated transition of NH) are not consolidated as it was performed for the calculation to emphasize the existenz of hyperfine structure lines which might be overlapping.

A cross **(X)** to the right of the transition frequency indicates, that the line intensity was calculated in Sect. 5.

A.1 CH

Transition (K, Λ, J, F)	Frequency ν ($\Delta\nu$) [GHz] ([MHz])	Band	Einstein-A $[s^{-1}]$	E_{up} $[K]$
$(1,1,\frac{3}{2},1) \rightarrow (1,-1,\frac{1}{2},1)$	532.7233 (0.6)	1	2.2(-4)	25.7
$(1,1,\frac{3}{2},2) \rightarrow (1,-1,\frac{1}{2},1)$	532.7255 (0.6) **(X)**	1	6.6(-4)	25.7
$(1,1,\frac{3}{2},1) \rightarrow (1,-1,\frac{1}{2},0)$	532.7950 (0.6)	1	4.4(-4)	25.7
$(1,-1,\frac{3}{2},2) \rightarrow (1,1,\frac{1}{2},1)$	536.7627 (0.6) **(X)**	1	6.8(-4)	25.8
$(1,-1,\frac{3}{2},1) \rightarrow (1,1,\frac{1}{2},1)$	536.7835 (0.6)	1	2.3(-4)	25.8
$(1,-1,\frac{3}{2},1) \rightarrow (1,1,\frac{1}{2},0)$	536.7973 (0.6)	1	4.6(-4)	25.8
$(2,-1,\frac{3}{2},1) \rightarrow (1,1,\frac{3}{2},2)$	1470.6828 (0.7)	6	9.5(-4)	96.3
$(2,-1,\frac{3}{2},1) \rightarrow (1,1,\frac{3}{2},1)$	1470.6850 (0.6)	6	4.7(-3)	96.3
$(2,-1,\frac{3}{2},2) \rightarrow (1,1,\frac{3}{2},2)$	1470.7327 (0.6)	6	5.1(-3)	96.3
$(2,-1,\frac{3}{2},2) \rightarrow (1,1,\frac{3}{2},1)$	1470.7349 (0.7)	6	5.7(-4)	96.3
$(2,1,\frac{3}{2},1) \rightarrow (1,-1,\frac{3}{2},1)$	1477.2854 (0.6)	6	4.7(-3)	96.7
$(2,1,\frac{3}{2},1) \rightarrow (1,-1,\frac{3}{2},2)$	1477.3063 (0.7)	6	9.4(-4)	96.7
$(2,1,\frac{3}{2},2) \rightarrow (1,-1,\frac{3}{2},1)$	1477.3585 (0.7)	6	5.7(-4)	96.7
$(2,1,\frac{3}{2},2) \rightarrow (1,-1,\frac{3}{2},2)$	1477.3794 (0.6)	6	5.1(-3)	96.7
$(2,-1,\frac{5}{2},3) \rightarrow (1,1,\frac{3}{2},2)$	1656.9563 (0.7) **(X)**	6	4.0(-2)	105.2
$(2,-1,\frac{5}{2},2) \rightarrow (1,1,\frac{3}{2},2)$	1656.9656 (0.8)	6	4.0(-3)	105.2
$(2,-1,\frac{5}{2},2) \rightarrow (1,1,\frac{3}{2},1)$	1656.9678 (0.8)	6	3.6(-2)	105.2
$(2,1,\frac{5}{2},3) \rightarrow (1,-1,\frac{3}{2},2)$	1661.1024 (0.7) **(X)**	6	4.0(-2)	105.5
$(2,1,\frac{5}{2},2) \rightarrow (1,-1,\frac{3}{2},1)$	1661.1131 (0.8)	6	3.6(-2)	105.5
$(2,1,\frac{5}{2},2) \rightarrow (1,-1,\frac{3}{2},2)$	1661.1339 (0.8)	6	4.0(-3)	105.5

Table 21: Molecular data of CH

A.2 CH^+

Transition K	Frequency ν ($\Delta\nu$) [GHz] ([MHz])	Band	Einstein-A $[s^{-1}]$	E_{up} $[K]$
$1 \rightarrow 0$	835.079 (1) **(X)**	3	2.3(-3)	40.1
$2 \rightarrow 1$	1669.1595 (60) **(X)**	6	2.2(-2)	120.2

Table 22: Molecular data of CH^+

A.3 NH

Transition (K, J, F_1, F)	Frequency ν ($\Delta\nu$) [GHz] ([MHz])	Band	Einstein-A $[s^{-1}]$	E_{up} $[K]$
$(1,0,\frac{1}{2},\frac{1}{2}) \rightarrow (0,1,\frac{1}{2},\frac{3}{2})$	946.3808 (0.1)	3	2.4(-3)	45.4
$(1,0,\frac{1}{2},\frac{3}{2}) \rightarrow (0,1,\frac{1}{2},\frac{3}{2})$	946.3808 (0.1)	3	9.6(-4)	45.4
$(1,0,\frac{1}{2},\frac{1}{2}) \rightarrow (0,1,\frac{1}{2},\frac{1}{2})$	946.4198 (0.03)	3	3.7(-4)	45.4
$(1,0,\frac{1}{2},\frac{3}{2}) \rightarrow (0,1,\frac{1}{2},\frac{1}{2})$	946.4200 (0.1)	3	9.0(-4)	45.4
$(1,0,\frac{1}{2},\frac{3}{2}) \rightarrow (0,1,\frac{3}{2},\frac{5}{2})$	946.4758 (0.1) **(X)**	3	3.3(-3)	45.4
$(1,0,\frac{1}{2},\frac{1}{2}) \rightarrow (0,1,\frac{3}{2},\frac{3}{2})$	946.5092 (0.1)	3	1.9(-3)	45.4
$(1,0,\frac{1}{2},\frac{3}{2}) \rightarrow (0,1,\frac{3}{2},\frac{3}{2})$	946.5092 (0.1)	3	1.2(-3)	45.4
$(1,0,\frac{1}{2},\frac{1}{2}) \rightarrow (0,1,\frac{3}{2},\frac{1}{2})$	946.5275 (0.1)	3	1.8(-3)	45.4
$(1,0,\frac{1}{2},\frac{3}{2}) \rightarrow (0,1,\frac{3}{2},\frac{1}{2})$	946.5276 (0.04)	3	1.8(-4)	45.4
$(1,2,\frac{5}{2},\frac{3}{2}) \rightarrow (0,1,\frac{1}{2},\frac{3}{2})$	974.3156 (0.1)	4	1.8(-6)	46.8
$(1,2,\frac{5}{2},\frac{5}{2}) \rightarrow (0,1,\frac{1}{2},\frac{3}{2})$	974.3426 (0.1)	4	6.0(-6)	46.8
$(1,2,\frac{5}{2},\frac{3}{2}) \rightarrow (0,1,\frac{1}{2},\frac{1}{2})$	974.3547 (0.1)	4	4.5(-6)	46.8
$(1,2,\frac{5}{2},\frac{3}{2}) \rightarrow (0,1,\frac{3}{2},\frac{5}{2})$	974.4106 (0.1)	4	8.9(-5)	46.8
$(1,2,\frac{3}{2},\frac{1}{2}) \rightarrow (0,1,\frac{1}{2},\frac{3}{2})$	974.4114 (0.1)	4	5.1(-4)	46.8
$(1,2,\frac{3}{2},\frac{3}{2}) \rightarrow (0,1,\frac{1}{2},\frac{3}{2})$	974.4368 (0.2)	4	2.3(-3)	46.8
$(1,2,\frac{5}{2},\frac{5}{2}) \rightarrow (0,1,\frac{3}{2},\frac{5}{2})$	974.4368 (0.2)	4	1.3(-3)	46.8
$(1,2,\frac{5}{2},\frac{3}{2}) \rightarrow (0,1,\frac{3}{2},\frac{3}{2})$	974.4440 (0.1)	4	1.8(-3)	46.8
$(1,2,\frac{3}{2},\frac{1}{2}) \rightarrow (0,1,\frac{1}{2},\frac{1}{2})$	974.4504 (0.1)	4	4.8(-3)	46.8
$(1,2,\frac{5}{2},\frac{3}{2}) \rightarrow (0,1,\frac{3}{2},\frac{1}{2})$	974.4622 (0.1)	4	5.0(-3)	46.8
$(1,2,\frac{5}{2},\frac{5}{2}) \rightarrow (0,1,\frac{3}{2},\frac{3}{2})$	974.4708 (0.3) **(X)**	4	5.7(-3)	46.8
$(1,2,\frac{3}{2},\frac{3}{2}) \rightarrow (0,1,\frac{1}{2},\frac{1}{2})$	974.4786 (0.5)	4	3.4(-3)	46.8
$(1,2,\frac{3}{2},\frac{5}{2}) \rightarrow (0,1,\frac{1}{2},\frac{3}{2})$	974.4786 (0.5)	4	6.0(-3)	46.8
$(1,2,\frac{5}{2},\frac{7}{2}) \rightarrow (0,1,\frac{3}{2},\frac{5}{2})$	974.4786 (0.5)	4	6.9(-3)	46.8
$(1,2,\frac{3}{2},\frac{3}{2}) \rightarrow (0,1,\frac{3}{2},\frac{5}{2})$	974.5313 (0.1)	4	2.6(-4)	46.8
$(1,2,\frac{3}{2},\frac{1}{2}) \rightarrow (0,1,\frac{3}{2},\frac{3}{2})$	974.5398 (0.1)	4	6.5(-4)	46.8
$(1,2,\frac{3}{2},\frac{1}{2}) \rightarrow (0,1,\frac{3}{2},\frac{1}{2})$	974.5581 (0.1)	4	9.8(-4)	46.8
$(1,2,\frac{3}{2},\frac{3}{2}) \rightarrow (0,1,\frac{3}{2},\frac{3}{2})$	974.5648 (0.1)	4	7.7(-4)	46.8
$(1,2,\frac{3}{2},\frac{5}{2}) \rightarrow (0,1,\frac{3}{2},\frac{5}{2})$	974.5744 (0.1)	4	8.1(-4)	46.8
$(1,2,\frac{3}{2},\frac{3}{2}) \rightarrow (0,1,\frac{3}{2},\frac{1}{2})$	974.5830 (0.1)	4	2.6(-4)	46.8
$(1,2,\frac{3}{2},\frac{5}{2}) \rightarrow (0,1,\frac{3}{2},\frac{3}{2})$	974.6079 (0.1)	4	1.2(-4)	46.8
$(1,1,\frac{3}{2},\frac{5}{2}) \rightarrow (0,1,\frac{1}{2},\frac{3}{2})$	999.8781 (0.5)	4	9.9(-4)	48.0

Transition (K, J, F_1, F)	Frequency ν ($\Delta\nu$) [GHz] ([MHz])	Band	Einstein-A $[s^{-1}]$	E_{up} $[K]$
$(1,1,\frac{1}{2},\frac{3}{2}) \rightarrow (0,1,\frac{1}{2},\frac{3}{2})$	999.8821 (0.1)	4	3.9(-3)	48.0
$(1,1,\frac{3}{2},\frac{3}{2}) \rightarrow (0,1,\frac{1}{2},\frac{3}{2})$	999.9060 (0.04)	4	3.2(-7)	48.0
$(1,1,\frac{3}{2},\frac{1}{2}) \rightarrow (0,1,\frac{1}{2},\frac{3}{2})$	999.9079 (0.1)	4	3.0(-3)	48.0
$(1,1,\frac{1}{2},\frac{1}{2}) \rightarrow (0,1,\frac{1}{2},\frac{3}{2})$	999.9192 (0.1)	4	1.1(-3)	48.0
$(1,1,\frac{1}{2},\frac{3}{2}) \rightarrow (0,1,\frac{1}{2},\frac{1}{2})$	999.9210 (0.2)	4	9.6(-4)	48.0
$(1,1,\frac{3}{2},\frac{3}{2}) \rightarrow (0,1,\frac{1}{2},\frac{1}{2})$	999.9451 (0.1)	4	1.8(-3)	48.0
$(1,1,\frac{3}{2},\frac{1}{2}) \rightarrow (0,1,\frac{1}{2},\frac{1}{2})$	999.9470 (0.03)	4	1.8(-4)	48.0
$(1,1,\frac{1}{2},\frac{1}{2}) \rightarrow (0,1,\frac{1}{2},\frac{1}{2})$	999.9582 (0.1)	4	1.7(-3)	48.0
$(1,1,\frac{3}{2},\frac{5}{2}) \rightarrow (0,1,\frac{3}{2},\frac{5}{2})$	999.9734 (0.1) **(X)**	4	5.2(-3)	48.0
$(1,1,\frac{1}{2},\frac{3}{2}) \rightarrow (0,1,\frac{3}{2},\frac{5}{2})$	999.9771 (0.1)	4	3.9(-4)	48.0
$(1,1,\frac{3}{2},\frac{3}{2}) \rightarrow (0,1,\frac{3}{2},\frac{5}{2})$	1000.0010 (0.1) **(X)**	4	2.9(-3)	48.0
$(1,1,\frac{3}{2},\frac{5}{2}) \rightarrow (0,1,\frac{3}{2},\frac{3}{2})$	1000.0068 (0.1)	4	1.2(-3)	48.0
$(1,1,\frac{1}{2},\frac{3}{2}) \rightarrow (0,1,\frac{3}{2},\frac{3}{2})$	1000.0105 (0.1)	4	1.7(-3)	48.0
$(1,1,\frac{1}{2},\frac{3}{2}) \rightarrow (0,1,\frac{3}{2},\frac{1}{2})$	1000.0288 (0.1)	4	4.9(-4)	48.0
$(1,1,\frac{3}{2},\frac{3}{2}) \rightarrow (0,1,\frac{3}{2},\frac{3}{2})$	1000.0345 (0.1)	4	1.6(-3)	48.0
$(1,1,\frac{3}{2},\frac{1}{2}) \rightarrow (0,1,\frac{3}{2},\frac{3}{2})$	1000.0363 (0.04)	4	4.4(-5)	48.0
$(1,1,\frac{1}{2},\frac{1}{2}) \rightarrow (0,1,\frac{3}{2},\frac{3}{2})$	1000.0474 (0.2)	4	4.5(-3)	48.0
$(1,1,\frac{3}{2},\frac{1}{2}) \rightarrow (0,1,\frac{3}{2},\frac{1}{2})$	1000.0539 (0.3)	4	4.1(-3)	48.0
$(1,1,\frac{3}{2},\frac{3}{2}) \rightarrow (0,1,\frac{3}{2},\frac{1}{2})$	1000.0539 (0.3)	4	1.1(-3)	48.0
$(1,1,\frac{1}{2},\frac{1}{2}) \rightarrow (0,1,\frac{3}{2},\frac{1}{2})$	1000.0658 (0.1)	4	1.6(-4)	48.0

Table 23: Molecular data of NH

A.4 OH^+

Transition (K, J, F)	Frequency ν ($\Delta\nu$) [GHz] ([MHz])	Band	Einstein-A $[s^{-1}]$	E_{up} $[K]$
$(1,0,1) \rightarrow (0,1,1)$	909.0452 (1)	3	5.2(-3)	43.6
$(1,0,1) \rightarrow (0,1,2)$	909.1588 (1) **(X)**	3	1.0(-2)	43.6
$(1,2,3) \rightarrow (0,1,2)$	971.8038 (2) **(X)**	4	1.8(-2)	46.6
$(1,2,2) \rightarrow (0,1,1)$	971.8053 (2)	4	1.5(-2)	46.6
$(1,2,2) \rightarrow (0,1,2)$	971.9192 (1)	4	3.0(-3)	46.6
$(1,1,1) \rightarrow (0,1,1)$	1032.9980 (1)	4	1.4(-2)	49.6
$(1,1,2) \rightarrow (0,1,1)$	1033.0044 (1)	4	3.5(-3)	49.6
$(1,1,1) \rightarrow (0,1,2)$	1033.1119 (1)	4	7.0(-3)	49.6
$(1,1,2) \rightarrow (0,1,2)$	1033.1186 (1) **(X)**	4	1.8(-2)	49.6
$(2,1,1) \rightarrow (1,1,2)$	1892.1066 (2)	6	2.4(-2)	140.4
$(2,1,1) \rightarrow (1,1,1)$	1892.1133 (2)	6	4.7(-2)	140.4
$(2,1,2) \rightarrow (1,1,2)$	1892.2272 (2) **(X)**	6	5.9(-2)	140.4
$(2,1,2) \rightarrow (1,1,1)$	1892.2338 (2)	6	1.2(-2)	140.4

Table 24: Molecular data of OH^+

A.5 SH

Transition (N', Λ, ν, J, F)	Frequency ν ($\Delta\nu$) [GHz] ([MHz])	Band	Einstein-A $[s^{-1}]$	E_{up} $[K]$
$(2,-1,1,\frac{3}{2},1) \rightarrow (1,1,1,\frac{1}{2},1)$	840.8606 (2)	3	4.4(-4)	4308.7
$(2,-1,1,\frac{3}{2},2) \rightarrow (1,1,1,\frac{1}{2},1)$	840.8610 (2)	3	1.3(-3)	4308.7
$(2,-1,1,\frac{3}{2},1) \rightarrow (1,1,1,\frac{1}{2},0)$	840.8744 (2)	3	8.8(-4)	4308.7
$(2,1,1,\frac{3}{2},1) \rightarrow (1,-1,1,\frac{1}{2},1)$	848.8408 (2)	3	4.5(-4)	4309.4
$(2,1,1,\frac{3}{2},2) \rightarrow (1,-1,1,\frac{1}{2},1)$	848.8713 (2)	3	1.4(-3)	4309.5
$(2,1,1,\frac{3}{2},1) \rightarrow (1,-1,1,\frac{1}{2},0)$	848.8922 (2)	3	9.1(-4)	4309.4
$(2,-1,0,\frac{3}{2},1) \rightarrow (1,1,0,\frac{1}{2},1)$	866.9467 (0.1) **(X)**	3	4.8(-4)	571.2
$(2,-1,0,\frac{3}{2},2) \rightarrow (1,1,0,\frac{1}{2},1)$	866.9467 (0.1) **(X)**	3	1.5(-3)	571.2
$(2,-1,0,\frac{3}{2},1) \rightarrow (1,1,0,\frac{1}{2},0)$	866.9603 (0.1)	3	9.7(-4)	571.2
$(2,1,0,\frac{3}{2},1) \rightarrow (1,-1,0,\frac{1}{2},1)$	875.2365 (0.1)	3	5.0(-4)	572.0
$(2,1,0,\frac{3}{2},2) \rightarrow (1,-1,0,\frac{1}{2},1)$	875.2671 (0.1) **(X)**	3	1.5(-3)	572.0
$(2,1,0,\frac{3}{2},1) \rightarrow (1,-1,0,\frac{1}{2},0)$	875.2882 (0.1)	3	9.9(-4)	572.0
$(3,-1,1,\frac{5}{2},2) \rightarrow (2,1,1,\frac{3}{2},2)$	1411.2170 (2)	6	7.5(-4)	4377.2
$(3,-1,1,\frac{5}{2},3) \rightarrow (2,1,1,\frac{3}{2},2)$	1411.2440 (2)	6	7.5(-3)	4377.2
$(3,-1,1,\frac{5}{2},2) \rightarrow (2,1,1,\frac{3}{2},1)$	1411.2475 (2)	6	6.8(-3)	4377.2
$(3,1,0,\frac{5}{2},3) \rightarrow (2,-1,0,\frac{3}{2},2)$	1447.0123 (0.1) **(X)**	6	8.1(-3)	640.6
$(3,1,0,\frac{5}{2},2) \rightarrow (2,-1,0,\frac{3}{2},2)$	1447.0143 (0.1)	6	8.1(-4)	640.6
$(3,1,0,\frac{5}{2},2) \rightarrow (2,-1,0,\frac{3}{2},1)$	1447.0147 (0.1)	6	7.3(-3)	640.6
$(3,-1,0,\frac{5}{2},2) \rightarrow (2,1,0,\frac{3}{2},2)$	1455.0734 (0.1)	6	8.2(-4)	641.8
$(3,-1,0,\frac{5}{2},3) \rightarrow (2,1,0,\frac{3}{2},2)$	1455.1005 (0.1) **(X)**	6	8.2(-3)	641.8
$(3,-1,0,\frac{5}{2},2) \rightarrow (2,1,0,\frac{3}{2},1)$	1455.1039 (0.1)	6	7.4(-3)	641.8
$(3,-1,1,\frac{7}{2},3) \rightarrow (2,1,1,\frac{5}{2},3)$	1879.5365 (2)	6	7.6(-4)	3892.4
$(3,-1,1,\frac{7}{2},4) \rightarrow (2,1,1,\frac{5}{2},3)$	1879.5373 (2)	6	1.6(-2)	3892.4
$(3,-1,1,\frac{7}{2},3) \rightarrow (2,1,1,\frac{5}{2},2)$	1879.5412 (2)	6	1.5(-2)	3892.4
$(3,1,1,\frac{7}{2},3) \rightarrow (2,-1,1,\frac{5}{2},3)$	1880.1402 (2)	6	7.6(-4)	3892.5
$(3,1,1,\frac{7}{2},4) \rightarrow (2,-1,1,\frac{5}{2},3)$	1880.1413 (2)	6	1.6(-2)	3892.5
$(3,1,1,\frac{7}{2},3) \rightarrow (2,-1,1,\frac{5}{2},2)$	1880.1450 (2)	6	1.5(-2)	3892.5

Table 25: Molecular data of SH

A.6 SH^+

Transition (N, J, F)	Frequency ν ($\Delta\nu$) [GHz] ([MHz])	Band	Einstein-A $[s^{-1}]$	E_{up} $[K]$
$(1,2,\frac{3}{2}) \rightarrow (0,1,\frac{1}{2})$	526.0388 (4)	1	8.1(-4)	25.3
$(1,2,\frac{5}{2}) \rightarrow (0,1,\frac{3}{2})$	526.0480 (4) **(X)**	1	9.7(-4)	25.2
$(1,2,\frac{3}{2}) \rightarrow (0,1,\frac{3}{2})$	526.1250 (4)	1	1.6(-4)	25.3

Transition (N, J, F)	Frequency ν ($\Delta\nu$) [GHz] ([MHz])	Band	Einstein-A $[s^{-1}]$	E_{up} $[K]$
$(1,1,\frac{3}{2}) \rightarrow (0,1,\frac{1}{2})$	683.3306 (4)	2	2.9(-4)	32.8
$(1,1,\frac{1}{2}) \rightarrow (0,1,\frac{1}{2})$	683.3565 (4)	2	1.2(-3)	32.8
$(1,1,\frac{3}{2}) \rightarrow (0,1,\frac{3}{2})$	683.4168 (4) **(X)**	2	1.5(-3)	32.8
$(1,1,\frac{1}{2}) \rightarrow (0,1,\frac{3}{2})$	683.4427 (4)	2	5.8(-4)	32.8
$(2,1,\frac{1}{2}) \rightarrow (1,1,\frac{1}{2})$	893.0544 (9)	3	2.0(-3)	75.7
$(2,1,\frac{1}{2}) \rightarrow (1,1,\frac{3}{2})$	893.0803 (9)	3	1.0(-3)	75.7
$(2,1,\frac{3}{2}) \rightarrow (1,1,\frac{1}{2})$	893.1146 (9)	3	5.0(-4)	75.7
$(2,1,\frac{3}{2}) \rightarrow (1,1,\frac{3}{2})$	893.1406 (9) **(X)**	3	2.5(-3)	75.7
$(2,1,\frac{1}{2}) \rightarrow (1,2,\frac{3}{2})$	1050.3721 (9)	4	1.3(-4)	75.7
$(2,1,\frac{3}{2}) \rightarrow (1,2,\frac{3}{2})$	1050.4324 (9)	4	1.3(-5)	75.7
$(2,1,\frac{3}{2}) \rightarrow (1,2,\frac{5}{2})$	1050.5093 (9)	4	1.2(-4)	75.7
$(2,3,\frac{5}{2}) \rightarrow (1,2,\frac{3}{2})$	1082.9064 (9)	4	9.2(-3)	77.2
$(2,3,\frac{7}{2}) \rightarrow (1,2,\frac{5}{2})$	1082.9094 (9) **(X)**	4	9.9(-3)	77.2
$(2,3,\frac{5}{2}) \rightarrow (1,2,\frac{5}{2})$	1082.9834 (9)	4	6.6(-4)	77.2
$(2,2,\frac{3}{2}) \rightarrow (1,1,\frac{1}{2})$	1094.7609 (9)	4	6.4(-3)	85.3
$(2,2,\frac{5}{2}) \rightarrow (1,1,\frac{3}{2})$	1094.7724 (9)	4	7.6(-3)	85.3
$(2,2,\frac{3}{2}) \rightarrow (1,1,\frac{3}{2})$	1094.7868 (9)	4	1.3(-3)	85.3
$(2,1,\frac{1}{2}) \rightarrow (1,0,\frac{1}{2})$	1230.5673 (9) **(X)**	5	6.8(-3)	75.7
$(2,1,\frac{3}{2}) \rightarrow (1,0,\frac{1}{2})$	1230.6275 (9)	5	6.8(-3)	75.7
$(3,2,\frac{3}{2}) \rightarrow (2,2,\frac{3}{2})$	1461.0890 (17)	6	4.2(-3)	155.5
$(3,2,\frac{3}{2}) \rightarrow (2,2,\frac{5}{2})$	1461.1035 (17)	6	4.6(-4)	155.5
$(3,2,\frac{5}{2}) \rightarrow (2,2,\frac{3}{2})$	1461.1516 (17)	6	3.1(-4)	155.5
$(3,2,\frac{5}{2}) \rightarrow (2,2,\frac{5}{2})$	1461.1660 (17)	6	4.3(-3)	155.5
$(3,2,\frac{3}{2}) \rightarrow (2,3,\frac{5}{2})$	1630.2613 (17)	6	7.9(-5)	155.5
$(3,2,\frac{5}{2}) \rightarrow (2,3,\frac{5}{2})$	1630.3238 (17)	6	3.6(-6)	155.5
$(3,2,\frac{5}{2}) \rightarrow (2,3,\frac{7}{2})$	1630.3977 (17)	6	7.5(-5)	155.5
$(3,4,\frac{7}{2}) \rightarrow (2,3,\frac{5}{2})$	1632.5160 (17)	6	3.5(-2)	155.6
$(3,4,\frac{9}{2}) \rightarrow (2,3,\frac{7}{2})$	1632.5175 (17) **(X)**	6	3.6(-2)	155.6
$(3,4,\frac{7}{2}) \rightarrow (2,3,\frac{7}{2})$	1632.5899 (17)	6	1.3(-3)	155.6
$(3,3,\frac{5}{2}) \rightarrow (2,2,\frac{3}{2})$	1641.2813 (17)	6	3.0(-2)	164.1
$(3,3,\frac{7}{2}) \rightarrow (2,2,\frac{5}{2})$	1641.2856 (17)	6	3.3(-2)	164.1
$(3,3,\frac{5}{2}) \rightarrow (2,2,\frac{5}{2})$	1641.2957 (17)	6	2.2(-3)	164.1
$(3,2,\frac{3}{2}) \rightarrow (2,1,\frac{3}{2})$	1662.7353 (17)	6	5.2(-3)	155.5
$(3,2,\frac{3}{2}) \rightarrow (2,1,\frac{1}{2})$	1662.7955 (17)	6	2.6(-2)	155.5
$(3,2,\frac{5}{2}) \rightarrow (2,1,\frac{3}{2})$	1662.7979 (17)	6	3.1(-2)	155.5
$(3,3,\frac{7}{2}) \rightarrow (2,3,\frac{5}{2})$	1810.4434 (17)	6	1.8(-4)	164.1
$(3,3,\frac{5}{2}) \rightarrow (2,3,\frac{5}{2})$	1810.4535 (17)	6	4.8(-3)	164.1
$(3,3,\frac{7}{2}) \rightarrow (2,3,\frac{7}{2})$	1810.5173 (17)	6	4.9(-3)	164.1
$(3,3,\frac{5}{2}) \rightarrow (2,3,\frac{7}{2})$	1810.5274 (17)	6	2.4(-4)	164.1

Table 26: Molecular data of SH^+

A.7 H_2O^+

Transition (N, K_a, K_c, J, I_H, F)	Frequency ν ($\Delta\nu$) [GHz] ([MHz])	Band	Einstein-A $[s^{-1}]$	E_{up} $[K]$
$(3,1,2,\frac{5}{2},0,\frac{5}{2}) \rightarrow (2,2,1,\frac{3}{2},0,\frac{3}{2})$	543.2977 (6)	1	3.6(-4)	223.9
$(3,1,2,\frac{7}{2},0,\frac{7}{2}) \rightarrow (2,2,1,\frac{5}{2},0,\frac{5}{2})$	580.0620 (5)	1	4.5(-4)	223.0
$(3,1,2,\frac{5}{2},0,\frac{5}{2}) \rightarrow (2,2,1,\frac{5}{2},0,\frac{5}{2})$	598.2126 (6)	1	4.7(-5)	223.9
$(1,1,0,\frac{3}{2},0,\frac{3}{2}) \rightarrow (1,0,1,\frac{1}{2},0,\frac{1}{2})$	604.7201 (1)	1	1.3(-3)	59.2
$(1,1,0,\frac{3}{2},0,\frac{3}{2}) \rightarrow (1,0,1,\frac{3}{2},0,\frac{3}{2})$	607.2582 (1) **(X)**	1	6.2(-3)	59.2
$(1,1,0,\frac{1}{2},0,\frac{1}{2}) \rightarrow (1,0,1,\frac{1}{2},0,\frac{1}{2})$	631.8195 (1)	1	5.6(-3)	60.5
$(1,1,0,\frac{1}{2},0,\frac{1}{2}) \rightarrow (1,0,1,\frac{3}{2},0,\frac{3}{2})$	634.3576 (1)	1	2.8(-3)	60.5
$(6,2,5,\frac{11}{2},0,\frac{11}{2}) \rightarrow (5,3,2,\frac{9}{2},0,\frac{9}{2})$	715.8514 (29)	2	8.0(-4)	729.5
$(2,0,2,\frac{5}{2},1,\frac{5}{2}) \rightarrow (1,1,1,\frac{1}{2},1,\frac{3}{2})$	717.5776 (2)	2	5.9(-8)	89.1
$(2,0,2,\frac{3}{2},1,\frac{1}{2}) \rightarrow (1,1,1,\frac{1}{2},1,\frac{3}{2})$	721.7384 (2)	2	3.1(-4)	89.3
$(2,0,2,\frac{3}{2},1,\frac{1}{2}) \rightarrow (1,1,1,\frac{1}{2},1,\frac{1}{2})$	721.7487 (2)	2	2.5(-3)	89.3
$(2,0,2,\frac{3}{2},1,\frac{3}{2}) \rightarrow (1,1,1,\frac{1}{2},1,\frac{3}{2})$	721.7557 (2)	2	1.2(-3)	89.3
$(2,0,2,\frac{3}{2},1,\frac{3}{2}) \rightarrow (1,1,1,\frac{1}{2},1,\frac{1}{2})$	721.7660 (2)	2	1.6(-3)	89.3
$(2,0,2,\frac{3}{2},1,\frac{5}{2}) \rightarrow (1,1,1,\frac{1}{2},1,\frac{3}{2})$	721.7845 (2)	2	2.8(-3)	89.3
$(2,0,2,\frac{5}{2},1,\frac{7}{2}) \rightarrow (1,1,1,\frac{3}{2},1,\frac{5}{2})$	742.0332 (1) **(X)**	2	3.6(-3)	89.1
$(2,0,2,\frac{5}{2},1,\frac{5}{2}) \rightarrow (1,1,1,\frac{3}{2},1,\frac{3}{2})$	742.0336 (1)	2	3.0(-3)	89.1
$(2,0,2,\frac{5}{2},1,\frac{3}{2}) \rightarrow (1,1,1,\frac{3}{2},1,\frac{1}{2})$	742.0374 (1)	2	2.7(-3)	89.1
$(2,0,2,\frac{5}{2},1,\frac{3}{2}) \rightarrow (1,1,1,\frac{3}{2},1,\frac{3}{2})$	742.0553 (1)	2	8.7(-4)	89.1
$(2,0,2,\frac{5}{2},1,\frac{5}{2}) \rightarrow (1,1,1,\frac{3}{2},1,\frac{5}{2})$	742.0635 (1)	2	5.9(-4)	89.1
$(2,0,2,\frac{5}{2},1,\frac{3}{2}) \rightarrow (1,1,1,\frac{3}{2},1,\frac{5}{2})$	742.0852 (1)	2	3.7(-5)	89.1
$(2,1,1,\frac{5}{2},1,\frac{7}{2}) \rightarrow (2,0,2,\frac{3}{2},1,\frac{5}{2})$	743.2482 (2)	2	8.6(-4)	125.0
$(2,1,1,\frac{5}{2},1,\frac{5}{2}) \rightarrow (2,0,2,\frac{3}{2},1,\frac{5}{2})$	743.2763 (2)	2	1.5(-4)	125.0
$(2,1,1,\frac{5}{2},1,\frac{3}{2}) \rightarrow (2,0,2,\frac{3}{2},1,\frac{5}{2})$	743.2964 (2)	2	9.8(-6)	125.0
$(2,1,1,\frac{5}{2},1,\frac{5}{2}) \rightarrow (2,0,2,\frac{3}{2},1,\frac{3}{2})$	743.3050 (2)	2	7.2(-4)	125.0
$(2,1,1,\frac{5}{2},1,\frac{3}{2}) \rightarrow (2,0,2,\frac{3}{2},1,\frac{3}{2})$	743.3251 (2)	2	2.2(-4)	125.0
$(2,1,1,\frac{5}{2},1,\frac{3}{2}) \rightarrow (2,0,2,\frac{3}{2},1,\frac{1}{2})$	743.3424 (2)	2	6.5(-4)	125.0
$(6,2,5,\frac{13}{2},0,\frac{13}{2}) \rightarrow (5,3,2,\frac{11}{2},0,\frac{11}{2})$	744.2053 (29)	2	9.0(-4)	728.0
$(2,0,2,\frac{3}{2},1,\frac{1}{2}) \rightarrow (1,1,1,\frac{3}{2},1,\frac{1}{2})$	746.1765 (2)	2	3.7(-4)	89.3
$(2,0,2,\frac{3}{2},1,\frac{3}{2}) \rightarrow (1,1,1,\frac{3}{2},1,\frac{1}{2})$	746.1938 (1)	2	1.5(-4)	89.3
$(2,0,2,\frac{3}{2},1,\frac{1}{2}) \rightarrow (1,1,1,\frac{3}{2},1,\frac{3}{2})$	746.1945 (2)	2	3.0(-4)	89.3
$(2,0,2,\frac{3}{2},1,\frac{3}{2}) \rightarrow (1,1,1,\frac{3}{2},1,\frac{3}{2})$	746.2118 (1)	2	3.6(-4)	89.3
$(2,0,2,\frac{3}{2},1,\frac{5}{2}) \rightarrow (1,1,1,\frac{3}{2},1,\frac{3}{2})$	746.2405 (2)	2	1.1(-4)	89.3
$(2,0,2,\frac{3}{2},1,\frac{3}{2}) \rightarrow (1,1,1,\frac{3}{2},1,\frac{5}{2})$	746.2417 (1)	2	1.6(-4)	89.3
$(2,0,2,\frac{3}{2},1,\frac{5}{2}) \rightarrow (1,1,1,\frac{3}{2},1,\frac{5}{2})$	746.2704 (1)	2	5.5(-4)	89.3
$(2,1,1,\frac{5}{2},1,\frac{7}{2}) \rightarrow (2,0,2,\frac{5}{2},1,\frac{5}{2})$	747.4551 (1)	2	9.5(-4)	125.0
$(2,1,1,\frac{5}{2},1,\frac{5}{2}) \rightarrow (2,0,2,\frac{5}{2},1,\frac{3}{2})$	747.4614 (1)	2	1.2(-3)	125.0
$(2,1,1,\frac{5}{2},1,\frac{3}{2}) \rightarrow (2,0,2,\frac{5}{2},1,\frac{3}{2})$	747.4815 (1)	2	9.7(-3)	125.0
$(2,1,1,\frac{5}{2},1,\frac{5}{2}) \rightarrow (2,0,2,\frac{5}{2},1,\frac{5}{2})$	747.4832 (1)	2	9.1(-3)	125.0
$(2,1,1,\frac{5}{2},1,\frac{7}{2}) \rightarrow (2,0,2,\frac{5}{2},1,\frac{7}{2})$	747.4854 (1)	2	1.1(-2)	125.0
$(2,1,1,\frac{5}{2},1,\frac{3}{2}) \rightarrow (2,0,2,\frac{5}{2},1,\frac{5}{2})$	747.5033 (1)	2	1.9(-3)	125.0
$(2,1,1,\frac{5}{2},1,\frac{5}{2}) \rightarrow (2,0,2,\frac{5}{2},1,\frac{7}{2})$	747.5135 (1)	2	1.3(-3)	125.0
$(2,1,1,\frac{3}{2},1,\frac{3}{2}) \rightarrow (2,0,2,\frac{3}{2},1,\frac{5}{2})$	762.7560 (1)	2	2.8(-3)	125.9

Transition (N, K_a, K_c, J, I_H, F)	Frequency ν ($\Delta\nu$) [GHz] ([MHz])	Band	Einstein-A $[s^{-1}]$	E_{up} $[K]$
$(2,1,1,\frac{3}{2},1,\frac{1}{2}) \rightarrow (2,0,2,\frac{3}{2},1,\frac{3}{2})$	762.7709 (1)	2	5.2(-3)	125.9
$(2,1,1,\frac{3}{2},1,\frac{5}{2}) \rightarrow (2,0,2,\frac{3}{2},1,\frac{5}{2})$	762.7791 (1)	2	1.0(-2)	125.9
$(2,1,1,\frac{3}{2},1,\frac{3}{2}) \rightarrow (2,0,2,\frac{3}{2},1,\frac{3}{2})$	762.7848 (1)	2	6.4(-3)	125.9
$(2,1,1,\frac{3}{2},1,\frac{1}{2}) \rightarrow (2,0,2,\frac{3}{2},1,\frac{1}{2})$	762.7882 (1)	2	6.6(-3)	125.9
$(2,1,1,\frac{3}{2},1,\frac{3}{2}) \rightarrow (2,0,2,\frac{3}{2},1,\frac{1}{2})$	762.8021 (1)	2	2.6(-3)	125.9
$(2,1,1,\frac{3}{2},1,\frac{5}{2}) \rightarrow (2,0,2,\frac{3}{2},1,\frac{3}{2})$	762.8079 (1)	2	1.9(-3)	125.9
$(2,1,1,\frac{3}{2},1,\frac{1}{2}) \rightarrow (2,0,2,\frac{5}{2},1,\frac{3}{2})$	766.9273 (2)	2	1.4(-3)	125.9
$(2,1,1,\frac{3}{2},1,\frac{3}{2}) \rightarrow (2,0,2,\frac{5}{2},1,\frac{3}{2})$	766.9412 (2)	2	2.1(-4)	125.9
$(2,1,1,\frac{3}{2},1,\frac{3}{2}) \rightarrow (2,0,2,\frac{5}{2},1,\frac{5}{2})$	766.9630 (2)	2	1.2(-3)	125.9
$(2,1,1,\frac{3}{2},1,\frac{5}{2}) \rightarrow (2,0,2,\frac{5}{2},1,\frac{3}{2})$	766.9643 (2)	2	5.4(-6)	125.9
$(2,1,1,\frac{3}{2},1,\frac{5}{2}) \rightarrow (2,0,2,\frac{5}{2},1,\frac{5}{2})$	766.9861 (2)	2	1.4(-4)	125.9
$(2,1,1,\frac{3}{2},1,\frac{5}{2}) \rightarrow (2,0,2,\frac{5}{2},1,\frac{7}{2})$	767.0163 (2)	2	1.2(-3)	125.9
$(6,2,5,\frac{11}{2},0,\frac{11}{2}) \rightarrow (5,3,2,\frac{11}{2},0,\frac{11}{2})$	774.2646 (29)	2	1.6(-5)	729.5
$(5,2,3,\frac{9}{2},0,\frac{9}{2}) \rightarrow (4,3,2,\frac{7}{2},0,\frac{7}{2})$	841.9973 (27) **(X)**	3	1.3(-3)	580.7
$(5,2,3,\frac{11}{2},0,\frac{11}{2}) \rightarrow (4,3,2,\frac{9}{2},0,\frac{9}{2})$	876.8793 (27)	3	1.5(-3)	579.2
$(5,2,3,\frac{9}{2},0,\frac{9}{2}) \rightarrow (4,3,2,\frac{9}{2},0,\frac{9}{2})$	909.8219 (28)	3	6.1(-5)	580.7
$(3,1,2,\frac{7}{2},0,\frac{7}{2}) \rightarrow (3,0,3,\frac{5}{2},0,\frac{5}{2})$	981.6707 (3)	4	9.3(-4)	223.0
$(3,1,2,\frac{7}{2},0,\frac{7}{2}) \rightarrow (3,0,3,\frac{7}{2},0,\frac{7}{2})$	987.4153 (3)	4	2.3(-2)	223.0
$(3,1,2,\frac{5}{2},0,\frac{5}{2}) \rightarrow (3,0,3,\frac{5}{2},0,\frac{5}{2})$	999.8213 (3)	4	2.3(-2)	223.9
$(3,1,2,\frac{5}{2},0,\frac{5}{2}) \rightarrow (3,0,3,\frac{7}{2},0,\frac{7}{2})$	1005.5659 (3)	4	1.2(-3)	223.9
$(1,1,1,\frac{3}{2},1,\frac{3}{2}) \rightarrow (0,0,0,\frac{1}{2},1,\frac{1}{2})$	1115.0591 (1)	4	1.7(-2)	53.5
$(1,1,1,\frac{3}{2},1,\frac{1}{2}) \rightarrow (0,0,0,\frac{1}{2},1,\frac{1}{2})$	1115.0771 (1)	4	2.8(-2)	53.5
$(1,1,1,\frac{3}{2},1,\frac{5}{2}) \rightarrow (0,0,0,\frac{1}{2},1,\frac{3}{2})$	1115.0860 (1) **(X)**	4	3.1(-2)	53.5
$(1,1,1,\frac{3}{2},1,\frac{3}{2}) \rightarrow (0,0,0,\frac{1}{2},1,\frac{3}{2})$	1115.1159 (1)	4	1.4(-2)	53.5
$(1,1,1,\frac{3}{2},1,\frac{1}{2}) \rightarrow (0,0,0,\frac{1}{2},1,\frac{3}{2})$	1115.1339 (1)	4	3.5(-3)	53.5
$(1,1,1,\frac{1}{2},1,\frac{1}{2}) \rightarrow (0,0,0,\frac{1}{2},1,\frac{1}{2})$	1139.5049 (1)	5	3.7(-3)	54.7
$(1,1,1,\frac{1}{2},1,\frac{3}{2}) \rightarrow (0,0,0,\frac{1}{2},1,\frac{1}{2})$	1139.5152 (1) **(X)**	5	1.5(-2)	54.7
$(1,1,1,\frac{1}{2},1,\frac{1}{2}) \rightarrow (0,0,0,\frac{1}{2},1,\frac{3}{2})$	1139.5616 (1)	5	2.9(-2)	54.7
$(1,1,1,\frac{1}{2},1,\frac{3}{2}) \rightarrow (0,0,0,\frac{1}{2},1,\frac{3}{2})$	1139.5719 (1)	5	1.8(-2)	54.7
$(3,0,3,\frac{5}{2},0,\frac{5}{2}) \rightarrow (2,1,2,\frac{5}{2},0,\frac{5}{2})$	1414.1752 (2)	6	2.8(-3)	175.9
$(5,2,3,\frac{11}{2},0,\frac{11}{2}) \rightarrow (5,1,4,\frac{11}{2},0,\frac{11}{2})$	1416.0503 (10)	6	7.5(-2)	579.2
$(3,2,1,\frac{5}{2},0,\frac{5}{2}) \rightarrow (3,1,2,\frac{5}{2},0,\frac{5}{2})$	1418.9554 (6)	6	5.8(-2)	292.0
$(5,2,3,\frac{9}{2},0,\frac{9}{2}) \rightarrow (5,1,4,\frac{9}{2},0,\frac{9}{2})$	1429.1456 (10)	6	7.7(-2)	580.7
$(3,2,1,\frac{5}{2},0,\frac{5}{2}) \rightarrow (3,1,2,\frac{7}{2},0,\frac{7}{2})$	1437.1060 (7)	6	3.1(-3)	292.0
$(5,2,3,\frac{9}{2},0,\frac{9}{2}) \rightarrow (5,1,4,\frac{11}{2},0,\frac{11}{2})$	1448.9929 (11)	6	1.5(-3)	580.7
$(2,2,0,\frac{5}{2},1,\frac{7}{2}) \rightarrow (2,1,1,\frac{3}{2},1,\frac{5}{2})$	1461.4267 (5)	6	3.1(-3)	196.1
$(2,2,0,\frac{5}{2},1,\frac{5}{2}) \rightarrow (2,1,1,\frac{3}{2},1,\frac{5}{2})$	1461.4491 (5)	6	5.1(-4)	196.1
$(2,2,0,\frac{5}{2},1,\frac{3}{2}) \rightarrow (2,1,1,\frac{3}{2},1,\frac{5}{2})$	1461.4651 (5)	6	3.2(-5)	196.1
$(2,2,0,\frac{5}{2},1,\frac{5}{2}) \rightarrow (2,1,1,\frac{3}{2},1,\frac{3}{2})$	1461.4722 (5)	6	2.6(-3)	196.1
$(2,2,0,\frac{5}{2},1,\frac{3}{2}) \rightarrow (2,1,1,\frac{3}{2},1,\frac{3}{2})$	1461.4882 (5)	6	7.6(-4)	196.1
$(2,2,0,\frac{5}{2},1,\frac{3}{2}) \rightarrow (2,1,1,\frac{3}{2},1,\frac{1}{2})$	1461.5020 (5)	6	2.4(-3)	196.1
$(2,2,0,\frac{5}{2},1,\frac{7}{2}) \rightarrow (2,1,1,\frac{5}{2},1,\frac{5}{2})$	1480.9295 (5)	6	3.7(-3)	196.1
$(2,2,0,\frac{5}{2},1,\frac{5}{2}) \rightarrow (2,1,1,\frac{5}{2},1,\frac{3}{2})$	1480.9318 (5)	6	4.8(-3)	196.1
$(2,2,0,\frac{5}{2},1,\frac{3}{2}) \rightarrow (2,1,1,\frac{5}{2},1,\frac{3}{2})$	1480.9478 (5)	6	3.8(-2)	196.1

Transition (N, K_a, K_c, J, I_H, F)	Frequency ν ($\Delta\nu$) [GHz] ([MHz])	Band	Einstein-A $[s^{-1}]$	E_{up} $[K]$
$(2,2,0,\frac{5}{2},1,\frac{5}{2}) \rightarrow (2,1,1,\frac{5}{2},1,\frac{5}{2})$	1480.9519 (5)	6	3.5(-2)	196.1
$(2,2,0,\frac{5}{2},1,\frac{7}{2}) \rightarrow (2,1,1,\frac{5}{2},1,\frac{7}{2})$	1480.9576 (5)	6	4.1(-2)	196.1
$(2,2,0,\frac{5}{2},1,\frac{3}{2}) \rightarrow (2,1,1,\frac{5}{2},1,\frac{5}{2})$	1480.9679 (5)	6	7.2(-3)	196.1
$(2,2,0,\frac{5}{2},1,\frac{5}{2}) \rightarrow (2,1,1,\frac{5}{2},1,\frac{7}{2})$	1480.9800 (5)	6	4.9(-3)	196.1
$(2,2,0,\frac{3}{2},1,\frac{3}{2}) \rightarrow (2,1,1,\frac{3}{2},1,\frac{5}{2})$	1516.4307 (5)	6	1.1(-2)	198.7
$(2,2,0,\frac{3}{2},1,\frac{5}{2}) \rightarrow (2,1,1,\frac{3}{2},1,\frac{5}{2})$	1516.4399 (5)	6	4.0(-2)	198.7
$(2,2,0,\frac{3}{2},1,\frac{1}{2}) \rightarrow (2,1,1,\frac{3}{2},1,\frac{3}{2})$	1516.4483 (5)	6	2.1(-2)	198.7
$(2,2,0,\frac{3}{2},1,\frac{3}{2}) \rightarrow (2,1,1,\frac{3}{2},1,\frac{3}{2})$	1516.4538 (5)	6	2.5(-2)	198.7
$(2,2,0,\frac{3}{2},1,\frac{1}{2}) \rightarrow (2,1,1,\frac{3}{2},1,\frac{1}{2})$	1516.4622 (5)	6	2.6(-2)	198.7
$(2,2,0,\frac{3}{2},1,\frac{5}{2}) \rightarrow (2,1,1,\frac{3}{2},1,\frac{3}{2})$	1516.4630 (5)	6	7.5(-3)	198.7
$(2,2,0,\frac{3}{2},1,\frac{3}{2}) \rightarrow (2,1,1,\frac{3}{2},1,\frac{1}{2})$	1516.4677 (5)	6	1.0(-2)	198.7
$(2,2,0,\frac{3}{2},1,\frac{1}{2}) \rightarrow (2,1,1,\frac{5}{2},1,\frac{3}{2})$	1535.9080 (6)	6	5.3(-3)	198.7
$(2,2,0,\frac{3}{2},1,\frac{3}{2}) \rightarrow (2,1,1,\frac{5}{2},1,\frac{3}{2})$	1535.9135 (6)	6	8.4(-4)	198.7
$(2,2,0,\frac{3}{2},1,\frac{5}{2}) \rightarrow (2,1,1,\frac{5}{2},1,\frac{3}{2})$	1535.9227 (6)	6	2.3(-5)	198.7
$(2,2,0,\frac{3}{2},1,\frac{3}{2}) \rightarrow (2,1,1,\frac{5}{2},1,\frac{5}{2})$	1535.9336 (6)	6	4.4(-3)	198.7
$(2,2,0,\frac{3}{2},1,\frac{5}{2}) \rightarrow (2,1,1,\frac{5}{2},1,\frac{5}{2})$	1535.9428 (6)	6	5.5(-4)	198.7
$(2,2,0,\frac{3}{2},1,\frac{5}{2}) \rightarrow (2,1,1,\frac{5}{2},1,\frac{7}{2})$	1535.9708 (6)	6	4.7(-3)	198.7
$(6,2,4,\frac{13}{2},1,\frac{15}{2}) \rightarrow (6,1,5,\frac{11}{2},1,\frac{13}{2})$	1578.2015 (16)	6	9.0(-4)	774.6
$(6,2,4,\frac{13}{2},1,\frac{13}{2}) \rightarrow (6,1,5,\frac{11}{2},1,\frac{13}{2})$	1578.2264 (16)	6	2.2(-5)	774.6
$(6,2,4,\frac{13}{2},1,\frac{13}{2}) \rightarrow (6,1,5,\frac{11}{2},1,\frac{11}{2})$	1578.2504 (16)	6	8.9(-4)	774.6
$(6,2,4,\frac{13}{2},1,\frac{11}{2}) \rightarrow (6,1,5,\frac{11}{2},1,\frac{11}{2})$	1578.2721 (16)	6	2.6(-5)	774.6
$(6,2,4,\frac{13}{2},1,\frac{11}{2}) \rightarrow (6,1,5,\frac{11}{2},1,\frac{9}{2})$	1578.2924 (16)	6	8.8(-4)	774.6
$(6,2,4,\frac{13}{2},1,\frac{15}{2}) \rightarrow (6,1,5,\frac{13}{2},1,\frac{13}{2})$	1600.1104 (16)	6	1.9(-3)	774.6
$(6,2,4,\frac{13}{2},1,\frac{13}{2}) \rightarrow (6,1,5,\frac{13}{2},1,\frac{11}{2})$	1600.1132 (16)	6	2.1(-3)	774.6
$(6,2,4,\frac{13}{2},1,\frac{11}{2}) \rightarrow (6,1,5,\frac{13}{2},1,\frac{11}{2})$	1600.1348 (16)	6	1.0(-1)	774.6
$(6,2,4,\frac{13}{2},1,\frac{13}{2}) \rightarrow (6,1,5,\frac{13}{2},1,\frac{13}{2})$	1600.1354 (16)	6	1.0(-1)	774.6
$(6,2,4,\frac{13}{2},1,\frac{15}{2}) \rightarrow (6,1,5,\frac{13}{2},1,\frac{15}{2})$	1600.1360 (16)	6	1.0(-1)	774.6
$(6,2,4,\frac{13}{2},1,\frac{11}{2}) \rightarrow (6,1,5,\frac{13}{2},1,\frac{13}{2})$	1600.1571 (16)	6	2.5(-3)	774.6
$(6,2,4,\frac{13}{2},1,\frac{13}{2}) \rightarrow (6,1,5,\frac{13}{2},1,\frac{15}{2})$	1600.1610 (16)	6	2.1(-3)	774.6
$(6,2,4,\frac{11}{2},1,\frac{11}{2}) \rightarrow (6,1,5,\frac{11}{2},1,\frac{13}{2})$	1610.3062 (16)	6	2.9(-3)	776.1
$(6,2,4,\frac{11}{2},1,\frac{9}{2}) \rightarrow (6,1,5,\frac{11}{2},1,\frac{11}{2})$	1610.3105 (16)	6	3.5(-3)	776.1
$(6,2,4,\frac{11}{2},1,\frac{13}{2}) \rightarrow (6,1,5,\frac{11}{2},1,\frac{13}{2})$	1610.3295 (16)	6	1.0(-1)	776.1
$(6,2,4,\frac{11}{2},1,\frac{11}{2}) \rightarrow (6,1,5,\frac{11}{2},1,\frac{11}{2})$	1610.3302 (16)	6	1.0(-1)	776.1
$(6,2,4,\frac{11}{2},1,\frac{9}{2}) \rightarrow (6,1,5,\frac{11}{2},1,\frac{9}{2})$	1610.3309 (16)	6	1.0(-1)	776.1
$(6,2,4,\frac{11}{2},1,\frac{11}{2}) \rightarrow (6,1,5,\frac{11}{2},1,\frac{9}{2})$	1610.3506 (16)	6	2.9(-3)	776.1
$(6,2,4,\frac{11}{2},1,\frac{13}{2}) \rightarrow (6,1,5,\frac{11}{2},1,\frac{11}{2})$	1610.3535 (16)	6	2.5(-3)	776.1
$(2,1,2,\frac{5}{2},0,\frac{5}{2}) \rightarrow (1,0,1,\frac{3}{2},0,\frac{3}{2})$	1625.6044 (1)	6	8.6(-2)	108.0
$(6,2,4,\frac{11}{2},1,\frac{9}{2}) \rightarrow (6,1,5,\frac{13}{2},1,\frac{11}{2})$	1632.1733 (16)	6	1.5(-3)	776.1
$(6,2,4,\frac{11}{2},1,\frac{11}{2}) \rightarrow (6,1,5,\frac{13}{2},1,\frac{11}{2})$	1632.1930 (16)	6	3.4(-5)	776.1
$(6,2,4,\frac{11}{2},1,\frac{11}{2}) \rightarrow (6,1,5,\frac{13}{2},1,\frac{13}{2})$	1632.2152 (16)	6	1.4(-3)	776.1
$(6,2,4,\frac{11}{2},1,\frac{13}{2}) \rightarrow (6,1,5,\frac{13}{2},1,\frac{13}{2})$	1632.2385 (16)	6	2.9(-5)	776.1
$(6,2,4,\frac{11}{2},1,\frac{13}{2}) \rightarrow (6,1,5,\frac{13}{2},1,\frac{15}{2})$	1632.2641 (16)	6	1.4(-3)	776.1
$(2,1,2,\frac{3}{2},0,\frac{3}{2}) \rightarrow (1,0,1,\frac{1}{2},0,\frac{1}{2})$	1638.2007 (1) **(X)**	6	7.3(-2)	108.7
$(2,1,2,\frac{3}{2},0,\frac{3}{2}) \rightarrow (1,0,1,\frac{3}{2},0,\frac{3}{2})$	1640.7388 (2)	6	1.6(-2)	108.7

Transition (N, K_a, K_c, J, I_H, F)	Frequency ν ($\Delta\nu$) [GHz] ([MHz])	Band	Einstein-A $[s^{-1}]$	E_{up} $[K]$
$(2,2,1,\frac{5}{2},0,\frac{5}{2}) \rightarrow (2,1,2,\frac{3}{2},0,\frac{3}{2})$	1800.6495 (5)	6	3.9(-3)	195.2
$(2,2,1,\frac{5}{2},0,\frac{5}{2}) \rightarrow (2,1,2,\frac{5}{2},0,\frac{5}{2})$	1815.7839 (5)	6	6.3(-2)	195.2
$(5,1,4,\frac{11}{2},0,\frac{11}{2}) \rightarrow (5,0,5,\frac{9}{2},0,\frac{9}{2})$	1826.9730 (15)	6	1.3(-3)	511.2
$(5,1,4,\frac{11}{2},0,\frac{11}{2}) \rightarrow (5,0,5,\frac{11}{2},0,\frac{11}{2})$	1835.3426 (15)	6	9.1(-2)	511.2
$(5,1,4,\frac{9}{2},0,\frac{9}{2}) \rightarrow (5,0,5,\frac{9}{2},0,\frac{9}{2})$	1846.8203 (15)	6	9.3(-2)	512.2
$(5,1,4,\frac{9}{2},0,\frac{9}{2}) \rightarrow (5,0,5,\frac{11}{2},0,\frac{11}{2})$	1855.1899 (16)	6	1.8(-3)	512.2
$(2,2,1,\frac{3}{2},0,\frac{3}{2}) \rightarrow (2,1,2,\frac{3}{2},0,\frac{3}{2})$	1855.5645 (5)	6	6.5(-2)	197.8
$(2,2,1,\frac{3}{2},0,\frac{3}{2}) \rightarrow (2,1,2,\frac{5}{2},0,\frac{5}{2})$	1870.6989 (6)	6	7.2(-3)	197.8
$(7,2,5,8,0,8) \rightarrow (7,1,6,7,0,7)$	1909.1982 (30)	6	1.3(-3)	1002.3

Table 27: Molecular data of H_2O^+

B Maps of the recorded spectra

B.1 S140

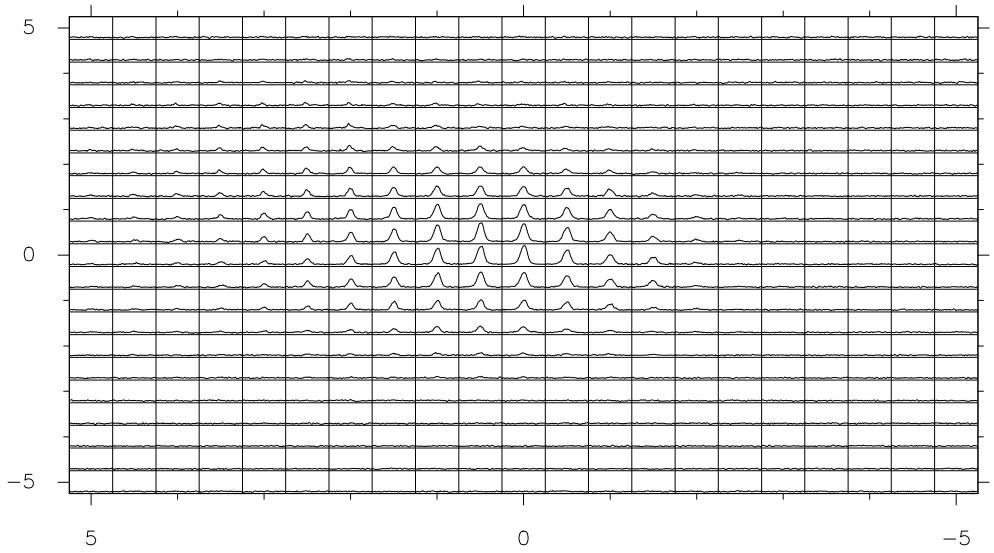

Figure 42: Map of the recorded spectra for HCO^+(3-2) of S140. The x-range is -16 to 2 km s^{-1} and the y-range is -0.5 to 5 K.

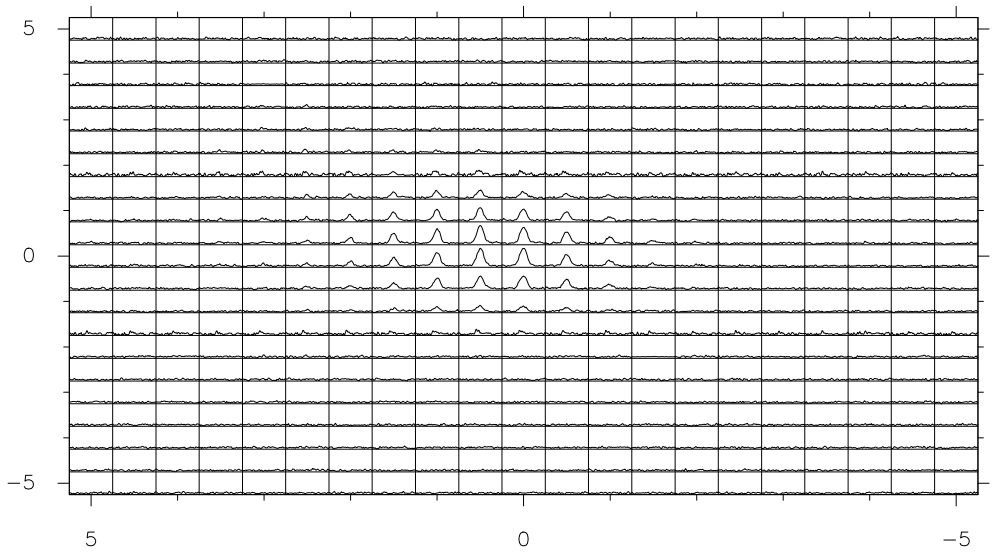

Figure 43: Map of the recorded spectra for HCO^+(4-3) of S140. The x-range is -16 to 2 km s^{-1} and the y-range is -0.5 to 7 K.

B.2 W3

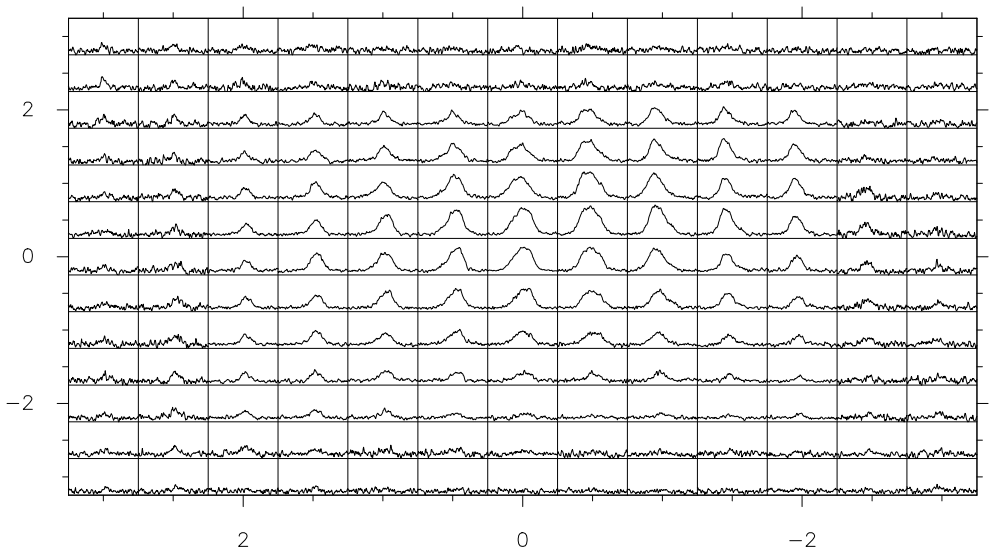

Figure 44: Map of the recorded spectra for HCO^+(3-2) of W3. The x-range is -55 to -25 km s^{-1} and the y-range is -0.3 to 2.5 K.

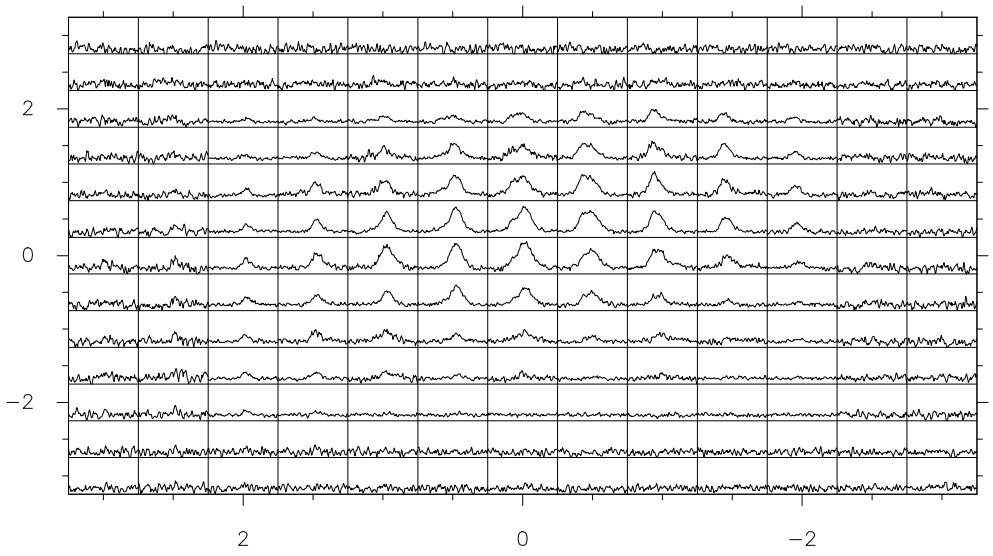

Figure 45: Map of the recorded spectra for HCO^+(4-3) of W3. The x-range is -55 to -25 km s^{-1} and the y-range is -0.7 to 3.8 K.

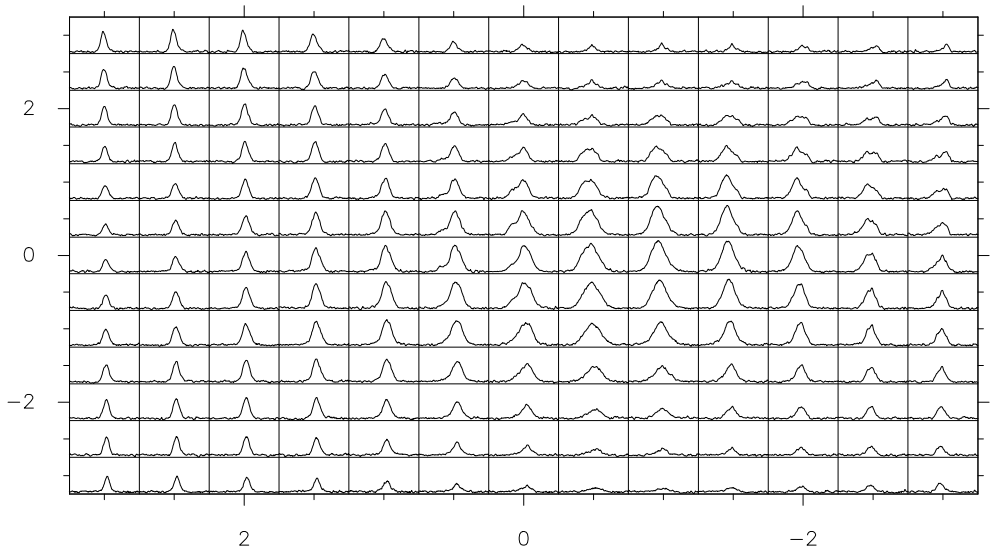

Figure 46: Map of the recorded spectra for ^{13}CO(2-1) of W3. The x-range is -55 to -25 km s^{-1} and the y-range is -0.8 to 11 K.

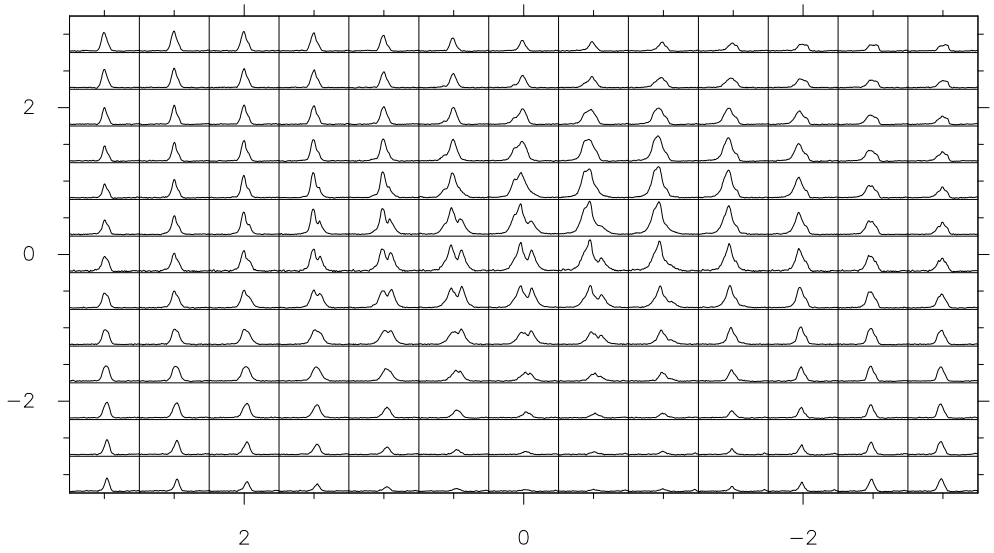

Figure 47: Map of the recorded spectra for CO(3-2) of W3. The x-range is -55 to -25 km s^{-1} and the y-range is -2 to 40 K.

Acknowledgments

I am thankful to the following persons who have supported and helped me with my work:

- Prof. Dr. Arnold Benz for giving me the possibility to do this work in his group, for his guidance and many useful suggestions.
- Pascal Stäuber for explaining me the chemistry and physics of Young Stellar Objects and his chemical models.
- Dr. Martin Schäfer for the introduction and help with the `SPCAT`-Program.
- Dr. Martin Miller and the I. Physikalisches Institut, University of Cologne, for giving me the possibility to make measurements with their KOSMA telescope.
- Marina Battaglia for letting me share her office and Paolo Grigis for helping at any `IDL`-difficulty.
- Michael Rissi for carefully reading the text and giving useful comments.
- My family for supporting me in every way during my time as student.

References

Afram, N. 2004, *Zeeman Effect in the FeH Molecule*, diploma thesis, Eidgenössische Technische Hochschule Zürich

Aspin, C., Beck T. 2001, *NIRI SV observation 20*, `http://www.gemini.edu/sciops/instruments/niri/SVobs/NIRISVobs20.html`

Benz, A.O., Güdel, M. 2005, *Physik der Stern und Planetenentstehung*, Lecture notes

Berdyugina, S.V., Livingston, W.C. 2002b, *Detection of the mercapto radical SH in the solar atmosphere*, Astronomy & Astrophysics, 387, L6-L9

Berdyugina, S.V., Solanki, S.K. 2002a, *The molecular Zeeman effect and diagnostics of solar and stellar magnetic fields. I. Theoretical spectral patterns in the Zeeman regime*, Astronomy & Astrophysics, 385, 701-715

Bergin, E.A., Plume, R., William, J.P., Myers, P.C. 1999, *The Ionization Fraction in Dense Molecular Gas. II. Massive Cores*, The Astrophysical Journal, 512, 724-739

Bernath, P.F. 2002, *Electronic Spectroscopy of Diatomic Molecules*, Handbook of Molecular Physics and Quantum Chemistry (Chap. 16), John Wiley & Sons Ltd.

Bernes, C. 1979, *A Monte Carlo approach to non-LTE radiative transfer problems*, Astronomy & Astrophysics, 79, 67-73

Beuther, H. 1999, *On the Fly Kartierung und Multilinienanalyse der interstellaren Molekülwolke Cepheus B*, Diplomarbeit, I. Physikalisches Institut der Universität zu Köln.

Blake, G.A., Sutton, E.C., Masson, C.R., Phillips, T.G. 1987, *Molecular abundances in OMC-1 - The chemical composition of interstellar molecular clouds and the influence of massive star formation*, The Astrophysical Journal, 315, 621-645

Brémaud, D. 2002, *Kartierung und physikalische Untersuchung der Sternentstehungsregion S140*, diploma thesis, Eidgenössische Technische Hochschule Zürich

Bruderer, S. 2004, *Cosmic background radiation at 200 MHz : determination of the Allan-variance for several frequencies*, semester thesis, Eidgenössische Technische Hochschule Zürich

Caselli, P. 2005, *Chemical processes in star forming regions*, astro-ph/0504298

CDMS: The Cologne Database for Molecular Spectroscopy, `http://www.cdms.de`

Colin, R. 1989, *Perturbations between the $X^2\Pi$ and $a^4\Sigma^-$ states of the NH^+ ion*, Journal of Molecular Spectroscopy, 136, 387-401

Crane, P., Lambert, D.L., Sheffer, Y. 1995, *A very high resolution survey of interstellar CH and CH^+*, The Astrophysical Journal Supplement Series, 99, 107-120

de Almeida, A.A, Singh, P.D. 1981, *NH^+ - A candidate for Comets and Interstellar Space*, Astronomy & Astrophysics, 113, 199-204

de Graauw, T., Helmich, F.P. 2001, *Herschel-HIFI: The Heterodyne Instrument for the Far - Infrared*, Proc. of 'The Promise of the Herschel Space Observatory' symposium held 12-15 December 2000 in Toledo, Spain, Eds.: G.L.Pilbratt, J.Cernicharo, A.M.Heras, T.Prusti, R.Harris, ESA SP-460, 45-51

Demtröder, W. 2005 (3 ed), *Atome, Moleküle und Festkörper*, Springer

Doty, S.D., Schier, F.L., van Dishoeck, E.F 2004, *Physical-chemical modeling of the low-mass protostar IRAS 16293-2422*, Astronomy & Astrophysics, 418, 1021-1034

Doty, S.D., van Dishoeck, E.F., van der Tak, F.F.S., Boonman, A. M. S. 2002, *Chemistry as a probe of the structures and evolution of massive star-forming regions*, Astronomy & Astrophysics, 389, 446-463

Douglas, A.E., Herzberg, G. 1941, *Note on CH^+ in Interstellar Space and in the Laboratory*, The Astrophysical Journal, 94, 381

Ewald, R. 1986, *HCO^+ und HCN in S140 und W51 / Beobachtungen mit dem Kölner 3m-Radioteleskop*, Ph.D. thesis, University of Cologne

Falgarone, E., Phillips, T.G., Pearson, J.C. 2005, *First Detection of $^{13}CH^+$ ($J = 1 - 0$)*, The Astrophysical Journal, 634, L149-L152

Frosch, R.A., Foley, H.M. 1952, *Magnetic Hyperfine Structure in Diatomic Molecules*, Physical Review, 88, 1337-1348

Genzel, R., Burton, W.B., Elmegreen, B.G. 1991, *The galactic interstellar medium*, Saas-Fee Advanced Course 21, Springer

Gerin, M., Falgarone, E., Giesen, T., Goldsmith, P., Herbst, E., Joblin, C., Krelowski, J., Langer, W., Martin-Pintado, J., Mookerjea, B., Neufeld, D., Pearson, J., Phillips, T., Spaans, M., Stutzki, J., Teyssier, D., Vastel, C. 2005, *Molecular carriers in the ISM*, unpublished

Gredel, R. 1997, *Interstellar CH^+ in southern OB associations*, Astronomy & Astrophysics, 320, 929-944

Hamel, J. 1998, *Geschichte der Astronomie*, Birkhäuser

Helmich, F.P., van Dishoeck, E.F. 1997, *Physical and chemical variations within the W3 star-forming region*, Astronomy & Astrophysics Supplement Series, 124, 205-253

Herbst, E. 2001, *The chemistry of interstellar space*, Chemical Society reviews, 30, 168-176

Herzberg G. 1965 (2 ed), *Molecular Spectra and Molecular Structure, I. Spectra of Diatomic Molecules*, D. Van Nostrand Company Inc.

Hofner, P., Delgado, H., Whitney, B., Chrchwell, E., Linz, H. 2002, *X-Ray Detection of the Ionizing Stars in Ultracompact HII Regions*, The Astrophysical Journal, 579, L95-L98

Hogerheijde, M.R., van der Tak, F.F.S. 2004, *RATRAN - Radiative transfer and molecular excitation in one and two dimensions*, `http://www.mpifr-bonn.mpg.de/staff/fvandertak/ratran/frames.html`

Hogerheijde, M.R., van der Tak, F.F.S. 2000, *An accelerated Monte Carlo method to solve two-dimensional radiative transfer and molecular excitation*, Astronomy & Astrophysics, 362, 697-710

Hougen, J.T. 1970, *The Calculation of Rotational Energy Levels and Rotational Line Intensities in Diatomic Molecules*, `http://physics.nist.gov/Pubs/Mono115/cover.html`

Hovde, D.C., Saykally, R.J. 1987, *Laser magnetic resonance in supersonic plasmas: The rotational spectrum of SH^+*, Journal of Chemical Physics, 87, 4332-4338

Jørgensen, J.K., Lahuis, F., Schöier, F.L., van Dishoeck, E.F., Blake, G.A., Boogert, A.C.A., Dullemond, C.P., Evans, N.J., Kessler-Silacci, J. E., Pontoppidan, K.M. 2005, *Protostellar Holes: Spitzer Space Telescope Observations of the Protostellar Binary IRAS 16293-2422*, The Astrophysical Journal, 631, L77L80

Jørgensen, J.K., Schöier, F.L., van Dishoeck, E.F. 2004, *Molecular inventories and chemical evolution of low-mass protostellar envelopes*, Astronomy & Astrophysics, 416, 603-622

JPL Molecular Spectroskopy, `http://spec.jpl.nasa.gov`

Klaus, T., Takano S., Winnewisser G. 1997, *Laboratory measurement of the $N = 1 \leftarrow 0$ rotational transition of NH at 1 THz*, Astronomy & Astrophysics, 322, L1-L4

Klisch, E., Klaus, T., Below, S.P., Dolgner, A., Schieder, R., Winnewisser, G. 1996, *The Rotational Spectrum of SH and SD*, The Astrophysical Journal, 473, 1118-1124

Kramer, C., Jakob, H., Mookerjea, B., Schneider, N., Brüll, M, Stutzki, J. 2004, *Emission of CO, CI and CII in W3 Main*, Astronomy & Astrophysics, 424, 887-903

Kramer, C., Beuther, H., Simon, R., Stutzki, J., Winnewisser, G. 2000, *Surveys with the New KOSMA Telescope*, Imaging at Radio through Submillimeter Wavelengths, ASP Conference Series Vol. 217, Edt: Jeffrey G. Mangum and Simon J. E. Radford

Kraus, J.D. 1966, *Radio Astronomy*, McGraw-Hill Book Company

Lada, C.J. 1987, *Star formation - From OB associations to protostars*, IAU Symposium 115: Star Forming Regions, 115, 1

Lequeux J., Falgarone E., Ryter Ch. 2005, *The Interstellar Medium*, A & A Library, Springer

Millar, T.J., Farquhar, P.R.A., Willacy, K. 1997, *The UMIST Database for Astrochemistry 1995*, Astronomy & Astrophysics Supplement Series, 121, 139 - 185

Müller, H.S.P., Thorwirth, S., Roth, D.A., Winnewisser, G. 2001, *The Cologne Database for Molecular Spectroscopy CDMS*, Astronomy & Astrophysics, 370, L49-L52

Nussbaumer, H. 2005, *Das Weltbild der Astronomie*, vdf Hochschulverlag AG

Pickett, H.M., Poynter, R.L., Cohen, E.A., Delitsky, M.L., Pearson, J.C., Muller, H.S.P. 1998 (rev. 4/2003), *Submillimeter, Millimeter, and Microwave Spectral Line Catalog*, Journal of quantitative spectroscopy and radiative transfer, 60, 883-890

Pickett, H.M. 1991, *The Fitting and Prediction of Vibration-Rotation Spectra with Spin Interactions*, Journal of Molecular Spectroscopy, 148, 371-377

Pilbratt, G.L. 2001, *The Herschel Mission, scientific objectives, and this meeting*, Proc. of 'The Promise of the Herschel Space Observatory' symposium held 12-15 December 2000 in Toledo, Spain, Eds.: G.L.Pilbratt, J.Cernicharo, A.M.Heras, T.Prusti, R.Harris, ESA SP-460, 13-20

Preibisch, T., Smith, M.D. 2002, *The outflow activity of the protostars in S140 IRS*, Astronomy & Astrophysics, 383, 540-547

Rydbeck, O. E. H., Kollberg, E., Hjalmarson, A., Sume, A., Ellder, J., Irvine, W. M. 1976, *Radio observations of interstellar CHI*, The Astrophysical Journal Supplement Series, 31, 333-415

Savage, C., Ziurys, L.M. 2004b, *Ion Chemistry in Photo-Dominated Regions: Examining the $[HCO^+]/[HOC^+]/[CO^+]$ Chemical Network*, The Astrophysical Journal, 616, 966-975

Savage, C., Apponi, A.J., Ziurys, L.M. 2004a, *Direct Measurement of the $N = 0 \rightarrow 1$ Transition of SH^+ ($X^3\Sigma^-$) by Submillimeter Velocity Modulation Spectroscopy*, The Astrophysical Journal, 608, L73-L76

Schöier, F.L., van der Tak, F.F.S., van Dishoeck, E.F., Black, J.H. 2005, *An atomic and molecular database for analysis of submillimetre line observations*, Astronomy & Astrophysics, 432, 369-379

Schwabl, F. 2002, *Quantenmechanik*, Springer

Shu, F.H., Fred, C.A., Lizano, S. 1987, *Star Formation in Molecular Clouds: Oberservation and Theory*, Annual Review of Astronomy and Astrophysics, 25, 23-81

Sigrist, M. 2003, *Quantenmechanik I/II*, Lecture Notes

Stäuber, P., Jørgensen, J.K., van Dishoeck, E.F., Doty, S.D., Benz, A.O. 2005b, *Water destruction by X-rays in young stellar objects*, Submitted to Astronomy & Astrophysics.

Stäuber, P., Doty, S.D., van Dishoeck, E.F., Benz, A.O. 2005a, *X-ray Chemistry in the envelopes around young stellar objects*, Astronomy & Astrophysics, 440, 949-966

Stäuber, P., Doty, S.D., van Dishoeck, E.F., Benz, A.O. 2004b, *X-ray chemistry in the envelopes around young stellar objects in The Dusty and Molecular Universe: A Prelude to Herschel and ALMA*, meeting held in Paris, France, October 27-29, 2004, Eds.: A. Wilson. ESA Conference Series, 222

Stäuber, P., Doty, S.D., van Dishoeck, E.F., Jørgensen, J.K., Benz, A.O. 2004a, *Influence of UV radiation from a massive YSO on the chemistry of its envelope*, Astronomy & Astrophysics, 425, 577-589

Stäuber, P. 2003, *Examination and interpretation of the star formation region S140 on large scales*, diploma thesis, Eidgenössische Technische Hochschule Zürich

Strahan, S.E., Müller, R.P., Saykally R.J. 1986, *Measurement of the rotational spectrum of the water cation (H_2O^+) by laser magnetic resonance*, Journal of Chemical Physics, 85, 1252-1261

Tafalla, M., Bachiller, R., Martin-Pintado, J. 1993, *Dense cores in L1204/S140 - Star formation and velocity shifts*, The Astrophysical Journal, 403, 175-182

van der Tak, F.F.S. 2005, *The chemistry of high-mass star formation*, astro-ph/0506146, `http://www.arxiv.org`

van der Tak, F.F.S., van Dishoeck, E.F. 2000, *Limits on the cosmic-ray ionization rate toward massiv young stars*, Astronomy & Astrophysics, 358, L79-L82

van Dishoeck, E.F., Blake, G.A. 1998, *Chemical Evolution of Star-Forming Regions*, Annual Review of Astronomy and Astrophysics, 36, 317-368

van Langevelde, H. J., van der Tak, F. F. S. 2004, *Radiation Bookkeeping: a guide to astronomical molecular spectroscopy and radiative transfer problems with an emphasis on RADEX*, `http://www.strw.leidenuniv.nl/~moldata/radex_manual.pdf`

van Zadelhoff, G.J., Dullemond, C.P., van der Tak, F.F.S., Yates, J.A., Doty, S.D., Ossenkopf, V., Hogerheijde, M.R., Juvela, M., Wiesemeyer, H., Schier, F. L. 2002, *Numerical methods for non-LTE line radiative transfer: Performance and convergence characteristics*, Astronomy & Astrophysics, 395, 373-384

Verhoeve, P., Ter Meulen, J.J., Leo Meerts, W., Dyamanus, A. 1986, *Observation of the lowest rotational transition of NH^+ with resolved hyperfine structure*, Chemical Physics Letters, 132, 213-217

Wehinger, P.A., Wyckoff, S., Herbig, G.H., Herzberg, G., Lew, H. 1974, *Identification of H_2O^+ in the Tail of Comet Kohoutek (1973f)*, The Astrophysical Journal, 190, L43

Whiting, E.E., Nicholls, R.W. 1974, *Reinvestigation of Rotational-Line Intensity Factors in Diatomic Spectra*, The Astrophysical Journal Supplement Series, 27, 1

Wilner, D.J. and Welch, W.J. 1993, *The S140 core: Aperture synthesis HCO^+ and SO observations*, The Astrophysical Journal, 427, 898 - 913

Zhou, S., Evans, N.J. II, Mundy, L.G., Kutner, M.L. 1993, *New VLA Observations of NH_3 in S140*, The Astrophysical Journal, 417, 613 - 623